
Theses and Dissertations

Fall 2013

Measurement and prediction of distortions during casting of a steel bar

Daniel Joseph Galles
University of Iowa

Follow this and additional works at: <https://ir.uiowa.edu/etd>



Part of the [Mechanical Engineering Commons](#)

Copyright 2013 Daniel Joseph Galles

This thesis is available at Iowa Research Online: <https://ir.uiowa.edu/etd/4986>

Recommended Citation

Galles, Daniel Joseph. "Measurement and prediction of distortions during casting of a steel bar." MS (Master of Science) thesis, University of Iowa, 2013.
<https://doi.org/10.17077/etd.1zam4k3k>

Follow this and additional works at: <https://ir.uiowa.edu/etd>



Part of the [Mechanical Engineering Commons](#)

MEASUREMENT AND PREDICTION OF DISTORTIONS DURING CASTING OF A
STEEL BAR

by
Daniel Joseph Galles

A thesis submitted in partial fulfillment
of the requirements for the Master of
Science degree in Mechanical Engineering
in the Graduate College of
The University of Iowa

December 2013

Thesis Supervisor: Professor Christoph Beckermann

Graduate College
The University of Iowa
Iowa City, Iowa

CERTIFICATE OF APPROVAL

MASTER'S THESIS

This is to certify that the Master's thesis of

Daniel Joseph Galles

has been approved by the Examining Committee
for the thesis requirement for the Master of Science
degree in Mechanical Engineering at the December 2013 graduation.

Thesis Committee: _____
Christoph Beckermann, Thesis Supervisor

Olesya I. Zhupanska

H.S. Udaykumar

ACKNOWLEDGEMENTS

This work would not have been possible without the support of many people. I would like to express gratitude to my advisor, Professor Christoph Beckermann, for his tremendous support, guidance, and insistence that I hold myself to the highest possible standards. I would like to thank the members of my thesis committee, Professors Olesya Zhupanska and H.S. Udaykumar, for their advice and input. I want to acknowledge the members of the Solidification Laboratory, especially Kent Carlson and Richard Hardin, for their support and encouragement. I also thank Jerry Thiel and the students at the University of Northern Iowa Metal Casting Center for their assistance in the casting trials. Special thanks are extended to my parents Roger and Donna, who taught me the most daunting tasks are accomplished through hard work, persistence, and a positive mindset. Finally, thanks to my wife, Cassandra, who has stood by me with unwavering support through this challenging process.

ABSTRACT

An elasto-visco-plastic deformation model predicts stresses and distortions in a low-carbon steel casting. Features of the model include rate and hardening effects, temperature-dependent properties, and pressure-dependent deformation in the mushy zone. A volume-averaging technique considers the multiple phases during solidification and is used to formulate the conservation equations, which (due to a weak link between temperatures and deformations) are decoupled and solved sequentially using commercial software. Temperature fields are calculated first using MAGMAsoft (*MAGMAsoft*, MAGMA GmbH, Kackerstrasse 11, 52072 Aachen, Germany) and then exported to a finite element software package, ABAQUS (*Abaqus/Standard*, Abaqus, Inc., Providence, RI, 2006), which predicts stresses and distortions. In order to simulate the conditions encountered in an industrial casting process, predicted temperatures and distortions are matched with experimental data from *in situ* casting trials. Preliminary simulations do not agree with the experimental distortions, which suggest that stress-strain data from mechanical tests (from which the mechanical properties were estimated) does not accurately characterize the material behavior of a casting during solidification and cooling. The adjustments needed to match measured and predicted distortions provide valuable insight to the effect a solidified microstructure has on its mechanical properties.

TABLE OF CONTENTS

LIST OF TABLES	vi
LIST OF FIGURES	vii
LIST OF NOMENCLATURE	xiv
LIST OF SYMBOLS	xv
CHAPTER 1: INTRODUCTION	1
1.1 Motivation.....	1
1.2 Objective of Present Study.....	2
CHAPTER 2: LITERATURE REVIEW	4
2.1 Introduction.....	4
2.2 Previous Experiments	4
2.2.1 Mechanical Testing.....	4
2.2.2 <i>In situ</i> Testing	5
2.3 Previous Models.....	7
CHAPTER 3: DESCRIPTION OF EXPERIMENTS	17
3.1 Introduction.....	17
3.2 Experimental Setup.....	17
3.3 Casting Procedure	20
3.4 Experimental Results	20
CHAPTER 4: THERMAL SIMULATIONS	40
4.1 Introduction.....	40
4.2 Thermophysical Properties and Parameters.....	40
4.3 Thermal Simulations.....	41
CHAPTER 5: MECHANICAL MODEL AND PROPERTIES	70
5.1 Introduction.....	70
5.2 Mechanical Model	70
5.3 Mechanical Properties.....	75
CHAPTER 6: STRESS SIMULATIONS	99
6.1 Introduction.....	99
6.2 Unrestrained Simulations.....	99
6.3 Strained Simulations	101
CHAPTER 7: CONCLUSIONS	126
REFERENCES	128

LIST OF TABLES

Table

3.1	Summary of sprue diameter and casting chemistry for all casting trials.	29
3.2	Summary of solidus temperatures. Solidus temperatures were experimentally determined as the temperature at the maximum cooling rates.	34
5.1	Estimated viscoplastic parameters.	82

LIST OF FIGURES

Figure

- 2.1 Experimental setup of Monroe and Beckermann. A T-shaped casting was restrained from free contraction with a restraint built from two pipes and endplates. Restraining bolts (F1 and F2) were embedded in each end of the casting and connected in series with load bolts, which dynamically measured the restraining force. The casting contraction was transmitted from tabs (which protruded from the casting) via quartz rods and dynamically measured with LVDT's (D2 and D4).....11
- 2.2 Submerged split-chill tensile (SSCT) test developed by Ackermann *et al.* The two-piece cylinder consists of a stationary upper part (2) and lower part (1). After a shell forms around the cylinders, a downward force is applied to a piston (which is connected to the lower cylinder) to separate the cylinders and deform the solidifying shell. The applied force and piston displacement are dynamically measured.12
- 2.3 Experimental setup of Motoyama and coworkers. To characterize the material behavior of a solidifying aluminum alloy in a sand mold, an experiment was devised to generate axial forces through the casting resulting from mold-metal interactions at the flange. The length change in the casting and axial forces were measured with an LVDT and a load cell, respectively.13
- 2.4 Experimental setup of Bellet *et al.* Displacement transducers (E, F, G, H) were placed at the mid-height of the casting near the mold metal interface to dynamically measure gap formation between the casting and mold.14
- 2.5 Top view of the experimental setup of Stangeland *et al.* Two aluminum bars were cast and fed from a cylindrical feeder. Anchor bolts were used to prevent thermal contractions. The axial force and length change of the lower bar were measured dynamically.15
- 2.6 Schematic of submerged split-chill compression (SSCC) test. This is a simplified version of the SSCT test (developed by Ackermann *et al.*). During solidification, the required force (F_z) to maintain the vertical position at the top of the assembly is measured dynamically.....16
- 3.1 Schematic of Strained and Unrestrained experimental setups at the casting mid-plane. Displacements and forces were measured with LVDT's (Linear Variable Differential Transformer) and load bolts, respectively. Temperatures were measured in the steel with type B thermocouples.....26
- 3.2 Pro-E drawings of the isometric view of the Strained and Unrestrained experimental setups. The molds were designed to contain symmetry about the mid-depth and mid-length vertical planes to minimize mold-metal interactions.....27

3.3	Mold dimensions and thermocouple placement for the Strained and Unrestrained setups. All dimensions are in inches. The yellow circles represent the thermocouple locations. The sprue diameter for Strained 4, 5, and 6 casting trials was 1.5 inches. All other casting trials used a 1-inch sprue diameter.....	28
3.4	Examples of the Unrestrained and Strained castings.....	30
3.5	Radiographs of the large-sprue and small-sprue Strained castings.	30
3.6	Measured temperature results at the Sprue location (shown on the schematic in Figure 3.3) of the Unrestrained (unr.) and Strained (str.) casting trials on large (12,000 s), medium (1600 s), and small (250 s) time scales.....	31
3.7	Measured temperature results at the Right location (shown on the schematic in Figure 3.3) of the Unrestrained (unr.) and Strained (str.) casting trials on large (12,000 s), medium (1600 s), and small (250 s) time scales.....	32
3.8	Cooling rates of the Unrestrained (unr.) and Strained (str.) bar experiments at the Sprue and Right locations. The approximate solidus temperature is experimentally determined as the temperature at which the maximum cooling rate occurs.	33
3.9	Measured axial length changes of the Strained (str.) and Unrestrained (unres.) bars on large (12,000 s), medium (1600 s), and small (250 s) time scales. As force is applied during the Strained experiments, the axial length change increases with time, as seen on the small time scale. The increasing axial length change seen after 600 s (on the medium time scale) is the result of the solid-state transformation.	35
3.10	Measured Left turnbuckle forces (shown on the schematic in Figure 3.1) of the Strained experiments at the Right location on large (12,000 s), medium (1600 s), and small (250 s) time scales. The decreasing force seen after 600 s (on the medium time scale) is the result of the solid-state transformation. The induced straining period (shown on the small time scale) shows the different times and durations for which the turnbuckle was turned.....	36
3.11	Comparison of Left and Right (shown on schematic in Figure 3.1) load bolt forces from the Strained 4 experiment. This difference in forces, which was typical of all Strained experiments, was the result an interaction between the mold and the sprue.	38
4.1	Thermophysical properties of steel. IDS used the experimental casting chemistry to calculate the thermophysical properties in the steel in IDS. Discontinuities in the curves at approximately 700°C are due to the solid-state transformation from austenite to ferrite and pearlite.	46
4.2	Solid fraction volume as a function of temperature. IDS used the experimental casting chemistry to calculate the volume of solid fraction as a function of temperature. The inflection point at $g_s=0.63$ is the result of the solid-state transformation from delta-ferrite to austenite.....	47

4.3	Interfacial heat transfer coefficient (<i>IHTC</i>). The interfacial heat transfer coefficient characterizes the heat transfer at the mold-metal interface. As the casting cools, an air gap forms at the interface and acts to decrease the heat transfer rate. The <i>IHTC</i> is taken from the “Steel-Sand” dataset in the MAGMASoft database.	48
4.4	Thermophysical properties of the mold. The thermophysical properties are taken from the “Furan” dataset located in the MAGMASoft database. The “spikes” in the effective specific heat curve at 100°C and 400°C account for endothermic reactions needed to evaporate the water and phenolic urethane binder, respectively.	49
4.5	Initial thermal simulation at the Sprue location.	50
4.6	Initial thermal simulation at the Right location. While reasonable agreement between simulated and measured temperatures is seen on the large scale, the small-scale comparison reveals a large difference in the time to solidus of approximately 75 s.	51
4.7	Thermal simulation after enhancing the thermal conductivity and adjusting the pouring temperature. The adjustments have a small impact on the simulation below the liquidus temperature.	52
4.8	Thermal simulation at the Sprue location after adjusting the latent heat of solidification from 249 to 180 kJ/kg. The difference in times to the solidus temperature is reduced from 100 s to 50 s after the adjustment.	53
4.9	Thermal simulation at the Right location after adjusting the latent heat of solidification from 249 to 180 kJ/kg. The difference in times to the solidus temperature is reduced from 75 s to 40 s after the adjustment.	54
4.10	Thermal simulation at the Sprue location after adjusting the thermal conductivity of the mold. The adjustment to the thermal conductivity in the mold results in good agreement in times to solidus.	55
4.11	Thermal simulation at the Right location after adjusting the thermal conductivity of the mold. The adjustment to the thermal conductivity in the mold results in good agreement in times to solidus.	56
4.12	Thermal simulation at the Sprue location after adjusting the solid fraction. Although the agreement is worse after the adjustment for this instance, it will generally improve the agreement in the other thermal simulations.	57
4.13	Thermal simulation at the Right location after adjusting the solid fraction. The measured and simulated temperatures agree throughout the solidification range after the adjustment.	58
4.14	Thermal simulation at the Sprue location after adjusting the <i>IHTC</i> . This adjustment results in good agreement after the solid-state transformation.	59
4.15	Thermal simulation at the Right location after adjusting the <i>IHTC</i> . This adjustment results in good agreement after the solid-state transformation.	60

4.16 Unrestrained 1 final thermal simulation at the Sprue location. The experimental thermocouple failed at the Right location.	61
4.17 Unrestrained 2 final thermal simulation at the Sprue and Right locations.	62
4.18 Unrestrained 3 final thermal simulation at the Sprue location. The thermocouple failed at the Right location.	63
4.19 Strained 1 final thermal simulation at the Sprue and Right locations.	64
4.20 Strained 2 final thermal simulation at the Sprue and Right locations.	65
4.21 Strained 3 final thermal simulation at the Sprue and Right locations.	66
4.22 Strained 4 final thermal simulation. The experimental thermocouple failed at the Right location.	67
4.23 Strained 5 final thermal simulation at the Sprue and Right locations.	68
4.24 Strained 6 final thermal simulation at the Sprue and Right locations.	69
5.1 The linear thermal expansion and total thermal expansion coefficient were calculated from the steel density. The total thermal expansion coefficient (defined in Equation 5.9) is the parameter required by ABAQUS to calculate thermal strains.	80
5.2 Elastic properties included a constant Poisson's ratio of 0.3 and temperature-dependent modulus of elasticity shown above taken from Li and Thomas.	81
5.3 Comparison between simulated and measured data at 20°C and 300°C from Maciejewski. Because the steel was rate-independent at these temperatures, i.e., $1/m = 0$, only two viscoplastic parameters (σ_0 and n) from the viscoplastic constitutive equation (Equation 18) remained to be estimated.	83
5.4 Strain rate and hardening exponents. The rate and hardening exponents were estimated using the experimental data of Suzuki <i>et al.</i> , Wray, and Maciejewski <i>et al.</i>	84
5.5 The reference strain rate was estimated with the high temperature data of Suzuki <i>et al.</i> and Wray and extended to the lower temperatures ($T < 700^\circ\text{C}$).	85
5.6 The initial yield stress was estimated using the experimental data of Suzuki <i>et al.</i> , Wray, and Maciejewski <i>et al.</i>	86
5.7 The reference strain was calculated from Young's modulus (E , shown in Figure 5.2), the hardening parameter ($1/n$, shown in Figure 5.4), and the initial yield stress (σ_0 , shown in Figure 5.6) using the relation $\varepsilon_0 = \sigma_0 n / E$	87
5.8 Comparison of predicted and measured (from Suzuki <i>et al.</i>) stresses at 0.19% carbon content. Each curve represents a different strain rate. The viscoplastic model can be evaluated based on its ability to reproduce the experimental stress-strain curves from which its parameters were estimated. The root-mean-square (RMS) values show the relative error for each curve.	88

- 5.9 Comparison of predicted and measured (from Wray) stresses at 0.005% carbon content. Each curve represents a different strain rate. The viscoplastic model can be evaluated based on its ability to reproduce the experimental stress-strain curves from which its parameters were estimated. The root-mean-square (RMS) values show the relative error for each curve.....90
- 5.10 Comparison of predicted and measured (from Wray) stresses at 0.051% carbon content. Each curve represents a different strain rate. The viscoplastic model can be evaluated based on its ability to reproduce the experimental stress-strain curves from which its parameters were estimated. The root-mean-square (RMS) values show the relative error for each curve.....91
- 5.11 Comparison of predicted and measured (from Wray) stresses at 0.29% carbon content. Each curve represents a different strain rate. The viscoplastic model can be evaluated based on its ability to reproduce the experimental stress-strain curves from which its parameters were estimated. The root-mean-square (RMS) values show the relative error for each curve.....92
- 5.12 Comparison of predicted and measured (from Wray) stresses at 0.46% carbon content. Each curve represents a different strain rate. The viscoplastic model can be evaluated based on its ability to reproduce the experimental stress-strain curves from which its parameters were estimated. The root-mean-square (RMS) values show the relative error for each curve.....93
- 5.13 Comparison of predicted and measured (from Wray) stresses at 0.71% carbon content. Each curve represents a different strain rate. The viscoplastic model can be evaluated based on its ability to reproduce the experimental stress-strain curves from which its parameters were estimated. The root-mean-square (RMS) values show the relative error for each curve.....94
- 5.14 Comparison of predicted and measured (from Wray) stresses at 0.93% carbon content. Each curve represents a different strain rate. The viscoplastic model can be evaluated based on its ability to reproduce the experimental stress-strain curves from which its parameters were estimated. The root-mean-square (RMS) values show the relative error for each curve.....95
- 5.15 Comparison of predicted and measured (from Wray) stresses at 1.24% carbon content. Each curve represents a different strain rate. The viscoplastic model can be evaluated based on its ability to reproduce the experimental stress-strain curves from which its parameters were estimated. The root-mean-square (RMS) values show the relative error for each curve.....96
- 5.16 Comparison of predicted and measured (from Wray) stresses at 1.54% carbon content. Each curve represents a different strain rate. The viscoplastic model can be evaluated based on its ability to reproduce the experimental stress-strain curves from which its parameters were estimated. The root-mean-square (RMS) values show the relative error for each curve.....97
- 5.17 Comparison of predicted and measured (from Maciejewski *et al.*) stresses at 0.23% carbon content. Each curve represents a different strain rate. The viscoplastic model can be evaluated based on its ability to reproduce the experimental stress-strain curves from which its parameters were estimated. The root-mean-square (RMS) values show the relative error for each curve.....98

6.1	ABAQUS model of the Unrestrained bar. To save computational costs, the steel in the pouring cup was not included in the simulations. Because the mold was not included in the stress simulations, an additional boundary condition was required on the right side of the model to restrict the bar to thermal contraction in the axial direction.	107
6.2	Stress simulation of Unrestrained 1. The “initial” curves use the IDS density to calculate the total thermal expansion coefficient. The “adjusted” total thermal expansion coefficient results in excellent agreement between measured and simulated axial length changes.	108
6.3	Stress simulation of Unrestrained 2. The “adjusted” total thermal expansion coefficient from Figure 6.2(c) was used for the simulation.....	109
6.4	Stress simulation of Unrestrained 3. The “adjusted” total thermal expansion coefficient from Figure 6.2(c) was used for the simulation.....	110
6.5	Density of the steel. The adjusted total thermal expansion coefficient, shown in Figure 6.2(c), is calculated using the “adjusted” density curve. The maximum relative difference between the curves is 0.8% (at the solidus temperature).	111
6.6	ABAQUS model of Strained bar. The displacement boundary conditions are the same as the Unrestrained bar (shown in Figure 6.1). The measured force from the Right load bolt is used as the force boundary condition on the right side of the bar. An additional force boundary condition is required at the base of the sprue to account for the force imbalance between the Left and Right force measurements.....	112
6.7	Simulated thermal fields of the small-sprue Strained bar at the beginning (a) and end (b) of the straining period. At the beginning of the straining period, the highest temperatures in the cross-section of the bar only have a range of 24°C ($1450 < T < 1474^{\circ}\text{C}$), resulting in relatively isothermal conditions along the axis (compared to the large-sprue bar).....	113
6.8	Simulated thermal fields of the large-sprue Strained bar at the beginning (a) and end (b) of the straining period. At the beginning of the straining period, the highest temperatures in the cross-section of the bar have a range of 151°C ($1347 < T < 1498^{\circ}\text{C}$), resulting in relatively large temperature gradients (compared to the small-sprue bars).....	114
6.9	Predicted equivalent plastic strain of the small-sprue (a) and large-sprue (b) bars. Significant plastic strain is predicted along the length of both small-sprue and large-sprue bars. The force boundary condition at the sprue creates a higher percentage of predicted plastic strain on the left side of the bar.	115
6.10	Comparison of the simulated and measured axial length changes of the Strained 1 experiment before and after adjustments to the strain rate exponent.....	116
6.11	Comparison of the simulated and measured axial length changes of the Strained 2 experiment before and after adjustments to the strain rate exponent.....	117

6.12 Comparison of the simulated and measured axial length changes of the Strained 3 experiment before and after adjustments to the strain rate exponent.....	118
6.13 Comparison of the simulated and measured axial length changes of the Strained 4 experiment before and after adjustments to the strain rate exponent.....	119
6.14 Comparison of the simulated and measured axial length changes of the Strained 5 experiment before and after adjustments to the strain rate exponent.....	120
6.15 Comparison of the simulated and measured axial length changes of the Strained 6 experiment before and after adjustments to the strain rate exponent.....	121
6.16 Adjusted strain rate exponents from all Strained stress simulations. The “initial” curve was estimated from the experimental data of Suzuki <i>et al.</i> , Wray, and Maciejewski <i>et al.</i> , shown in Figure 5.4.	122
6.17 Total thermal expansion coefficient of the steel. Because of differences in casting chemistries, slight variations were needed at the solid-state transformation to achieve reasonable agreement between measured and simulated length changes.	123
6.18 Parametric study of the strain rate exponent. To illustrate the necessity of the strain-rate exponent adjustments (shown in Figure 6.16), stress simulations were performed with iterations of the adjusted strain rate exponents. For this simulation, the “iteration 1” strain rate exponent curve matched the “final” curve at higher temperatures and “initial” curve at lower temperatures. As a result, the simulation predicts too little viscoplastic strain.....	124
6.19 Parametric study of the strain rate exponent. To illustrate the necessity of the strain-rate exponent adjustments (shown in Figure 6.16), stress simulations were performed using iterations of the adjusted strain rate exponents. For this simulation, the “iteration 2” strain rate exponent curve matched the “final” curve at lower temperatures and “initial” curve at higher temperatures. As a result, the simulation predicts too much viscoplastic strain and occurring too early.....	125
7.1 Strain rate exponent Mastercurve. The “initial” curve was estimated from the experimental data of Suzuki <i>et al.</i> , Wray, and Maciejewski <i>et al.</i> , shown in Figure 5.4.	127

LIST OF NOMENCLATURE

Acronyms

ALU	Arbitrary lagrangian eulerian
CAD	Computer-aided design
DAQ	Data acquisition system
DC	Direct-chill
IHTC	Interfacial heat transfer coefficient
LVDT	Linear variable differential transformer
RMS	Root mean square
SSCC	Submerged split-chill compression test
SSCT	Submerged split-chill tension test
UMAT	User material subroutine

LIST OF SYMBOLS

I	2^{nd} order identity tensor
α_{tot}	total thermal expansion coefficient
A	Arrhenius prefactor (1/s)
A_0'	polynomial coefficient used in parameter estimation of A
A_1	Cock's model constant
A_1'	polynomial coefficient used in parameter estimation of A
A_2	Cock's model constant
A_2'	1) polynomial coefficient used in parameter estimation of A and 2) constant in the yield function equation
A_3'	constant in the yield function equation
c_p	specific heat (kJ/kg-K)
C_e	4^{th} order elasticity tensor (MPa)
ϵ	strain tensor (mm/mm)
$\dot{\epsilon}$	strain rate (1/s)
ϵ_0	reference strain (mm/mm)
$\dot{\epsilon}_0$	reference strain rate (1/s)
ϵ_e	elastic strain tensor (mm/mm)
ϵ_{eq}	equivalent strain (mm/mm)
$\dot{\epsilon}_{eq}$	equivalent strain rate (1/s)
ϵ_{mech}	mechanical strain (mm/mm)
ϵ_{th}	thermal strain (mm/mm)
ϵ_{th}	thermal strain tensor (mm/mm)
ϵ_{total}	total strain (mm/mm)
ϵ_{vp}	viscoplastic strain tensor (mm/mm)
$\dot{\epsilon}_{vp}$	viscoplastic strain rate tensor (1/s)
E	Young's modulus (GPa)
g	gravitational vector (m/s^2)

g_l	volume fraction of liquid
g_s	volume fraction of solid
g_s^*	scaled solid fraction
g_s^{coal}	coalescence solid fraction
g_s^{coh}	coherency solid fraction
$g_{p,d}$	volume fraction of porosity due to damage
\mathbf{I}	4 th order identity tensor
\mathbf{I}_{dev}	4 th order deviatoric identity tensor
k	thermal conductivity (W/m-K)
K	permeability (m ²)
m	reciprocal of strain rate exponent
m_0'	polynomial coefficient used in parameter estimation of m
m_1'	polynomial coefficient used in parameter estimation of m
n	reciprocal of hardening exponent
n_0'	polynomial coefficient used in parameter estimation of n
n_1'	polynomial coefficient used in parameter estimation of n
p_l	liquid pressure (MPa)
p_s	solid pressure (MPa)
ρ	density (kg/m ³)
ρ_s	solid density (kg/m ³)
q_s	von Mises stress (MPa)
Q	activation energy (kJ/mol)
R	universal gas constant (kJ/mol-K)
σ	stress (MPa)
σ	stress tensor (MPa)
σ_0	initial yield stress (MPa)
σ_0'	polynomial coefficient used in parameter estimation of σ_0

σ_1'	polynomial coefficient used in parameter estimation of σ_0
σ_{dy}	dynamic yield stress (MPa)
σ_{eq}	equivalent stress (MPa)
σ_s	solid stress tensor (MPa)
$\tilde{\sigma}_s$	effective solid stress tensor (MPa)
t	time (s)
T	temperature (°C)
T_{coh}	coherency temperature (°C)
T_{liq}	liquidus temperature (°C)
T_{right}	temperature measured at the Right location of the casting (shown in Figure 3.1) (°C)
T_{sol}	solidus temperature (°C)
T_{sprue}	temperature measured at the Sprue location of the casting (shown in Figure 3.1) (°C)
τ_s	deviatoric stress tensor (MPa)
u_x	displacement in the x-direction
u_y	displacement in the y-direction
u_z	displacement in the z-direction
μ_l	liquid dynamic viscosity (kg/s-m)
ν	Poisson's ratio
y_i	measured value
\hat{y}_i	predicted value
$\dot{\gamma}$	scalar flow parameter (1/s)

CHAPTER 1: INTRODUCTION

1.1 Motivation

During solidification and cooling of a steel casting, thermal contractions not only reduce the casting volume but also lead to unwanted stress-induced distortions, i.e., plastic deformation. For particular casting geometries, however, a stress-free casting void of mechanical strains may be produced; consequently, the dimensional changes are the sole result of thermal strains, and the final dimensions are accurately predicted with a shrink rule. Nevertheless, this is generally not the case, as most geometries are conducive to the generation of stresses and associated mechanical strains resulting from 1) contact interactions at the mold-metal interface, 2) uneven cooling throughout the casting, and 3) the occurrence of solid-state phase transformations at different times throughout the casting. Not only can these stresses cause gross distortions in the final part, but also defects such as hot tears may form, which are irreversible cracks that develop in the semi-solid mushy zone [1]. For these reasons, the quality of the casting may be compromised and require costly, time-consuming rework.

A thorough understanding of the material behavior throughout the casting process is essential to minimize the aforementioned issues. In recent years, thermal simulation software has been combined with advanced stress models to predict stresses and deformations during solidification and cooling; to date, the models have been calibrated with stress-strain data from previous mechanical tests (using reheated samples in a controlled environment). Unfortunately, because the microstructure created during solidification differs from that of a reheated specimen, the ability of these models to accurately predict deformations in an industrial casting process has not been verified. In order to emulate the conditions encountered in a casting environment, measurements should be acquired during *in situ* experiments, from which the measurement of displacements at high temperatures provides a challenge.

1.2 Objective of Present Study

The objective of this work is to validate the finite element stress simulation of a steel casting throughout solidification and cooling using force and displacement measurements from *in situ* casting trials. By calibrating model parameters to match the *in situ* data, a better understanding will be gained as to the effect a cast microstructure has on its high-temperature mechanical properties.

For the present study, an elasto-visco-plastic constitutive model that considers damage is implemented in an ABAQUS user-defined UMAT subroutine to predict stresses and distortions during solidification and cooling in a steel casting. To validate the model, experimental data is acquired from *in situ* casting trials in which a long, slender low-carbon steel bar is produced. With the aid of a restraint and turnbuckle, an axial force is applied to the bar at high temperatures (before solidification is complete), generating stresses and mechanical strains in the casting. The applied force, dimensional changes, and temperatures of the bar are measured dynamically throughout the casting process. An additional casting trial serves as the experimental control to determine the thermal strain in the steel bar, which is subsequently subtracted from the total strain to calculate the mechanical strain.

Through a decoupling of the volume-averaged conservation equations, stresses and deformations are predicted in a two-step process using commercial software. In the first step, MAGMAsoft calculates the temperature fields during solidification and cooling, which are then used to determine the preliminary temperature-dependent mechanical properties (estimated with experimental stress-strain data from the literature) at all times and locations throughout the bar. In the second step, stresses and deformations are calculated with ABAQUS; the experimental control is simulated first to determine the thermal expansion coefficient of the steel. Then, using the measured force as a boundary condition, the axial length change of the steel bar is predicted. Finally,

through an adjustment to the elasto-visco-plastic parameters, the measured and simulated distortions are matched at all times throughout the casting process.

CHAPTER 2: LITERATURE REVIEW

2.1 Introduction

Plasticity of metals has been studied for hundreds of years across several disciplines, including physics, mathematics, and engineering. Data from previous experiments has been integral in the development and validation of deformation models. Until recently, the mechanical behavior near the melting point of metals had not been studied. With recent technological advances, however, the development of high-temperature testing machines has facilitated the characterization of material properties at temperatures encountered during casting processes. These tests have led to a better understanding of deformation mechanisms and material properties associated with high temperatures, which in turn have spurred the development of increasingly complex computational models. This chapter reviews previous 1) high-temperature experiments, and 2) computational models developed to predict stresses and deformations in casting processes. Primarily, this survey focuses on steel castings; however, relevant experiments and models of other metals (i.e., aluminum and magnesium alloys) are also briefly reviewed.

2.2 Previous Experiments

2.2.1 Mechanical Testing

Early attempts to characterize the high-temperature deformation of carbon steel alloys were conducted with mechanical tests using reheated specimens. Experiments were generally performed in a controlled, inert atmosphere, in which the specimens were annealed for a period to create isothermal conditions. Most studies were conducted with either steady-state tension (constant strain rate) or creep (constant load) tests. The first comprehensive study on the high-temperature behavior of steel was from Feltham [2], who performed creep tests in a vacuum furnace over a range of carbon contents (0.05% to 1.15%) for austenitic carbon steel from 940°C to 1300°C. Oxidation of the test sample

was prevented by smearing the inner walls of the furnace with carbon, which reacted with residual oxygen in the vacuum chamber to create a carbon monoxide atmosphere.

Wray and Holmes [3] used a vacuum furnace flooded with argon gas to perform tensile tests on several austenitic ferrous alloys from 950°C to 1350°C. With the exception of zone-refined iron, all samples produced similar stress-strain curves. Using the same experimental setup as [3], Wray [4] comprehensively characterized the mechanical behavior of austenitic carbon steel throughout a range of temperatures (850°C to 1250°C), carbon contents (0.005% to 1.54%), and strain rates (6×10^{-6} to 2×10^{-2} 1/s).

In order to study the different stress conditions during a continuous casting process of steel, Suzuki *et al.* [5] performed a series of creep experiments, including tension, compression, sinusoidal tension-compression, and stress removal tests. Using a single carbon content (0.19%), the tensile creep tests were performed at different stress levels (4.1 to 9.8 MPa) from 1250°C to 1400°C. The results of the tests were fitted to a time-hardening equation and valid for strains up to the onset of dynamic recrystallization.

Zhang *et al.* [6] performed tensile tests with a Gleeble at high temperatures (above 1200°C) and fit the data to an elasto-visco-plastic model. However, thermal gradients in the test specimens, which resulted in non-uniform deformation of the sample, created uncertainty in the parameter estimation.

2.2.2 *In situ* Testing

The nature of solidification inherently leads to solute rejection into the liquid, resulting in a segregated microstructure. Conversely, the annealing period during mechanical tests likely annihilates any existing microsegregation to create a homogeneous material. As a result, these microscopic differences may have a significant impact on the material properties. Therefore, data from *in situ* tests, rather than mechanical tests, should be used to characterize the mechanical properties. In addition,

due to the nonlinear stress-strain relationship of steel during plastic deformation, both force and displacement data should be measured dynamically throughout the entire casting process.

Parkins and Cowan [7] produced bar castings with flanges on either end to study the effect of the mold restraint on casting deformation. A contact interaction at the mold-metal interface of the flange constrained the bar from free contraction and induced plastic deformation during the cooling period. The contraction of the bar was measured dynamically using dial gauges, which monitored the displacement of steel rods embedded in each end of the casting. However, no restraint forces were measured in this study.

Nyichomba and coworkers [8,9,10] studied the effect of mold restraint on grey iron castings for different sand mold materials, including green sand and furan. While the casting geometry was similar to that of Parkins and Cowan [7], only the final contraction of the bars was measured after shakeout. Again, no restraint forces were measured.

Monroe and Beckermann [11] devised an experiment to dynamically measure both the casting deformation and restraining force in a T-shaped steel casting. The experimental setup included a restraint (shown in Figure 2.1), which was constructed from metal pipes and endplates. Force transducers (load bolts) were inserted through the restraint and connected in series with restraining bolts, which were embedded into each end of the casting. From small tabs (which protruded from the casting surface), the displacement was transmitted along quartz rods and measured with displacement transducers (LVDT's). Unfortunately, a contact interaction at the mold-metal interface of the tabs was the source of additional restraint in the casting, which was not measured by the load bolts.

The submerged split-chill tensile test (SSCT), which was developed by Ackermann *et al.* [12] and used in subsequent studies [13,14,15], characterizes the mechanical behavior during solidification to predict hot tears. The test apparatus consists

of a two-piece cylindrical assembly, shown in Figure 2.2. The upper part is fixed, while the lower part is connected to a piston (which may be translated vertically to create a gap between the upper and lower parts). The assembly is submerged into a pool of molten metal for a short period to form a solid shell around the cylinders. After removing the assembly from the pool, the piston is translated (using a hydraulic jack), which separates the upper and lower cylinders to deform the solidified shell. The applied force (from the jack) and displacement (of the piston) are dynamically measured. While this experiment gives valuable insight into the formation of hot tears, it is not particularly useful for the prediction of casting deformations; the complex geometry of the apparatus introduces uncertainty as to which force and displacements are being measured.

Several relevant *in situ* experimental studies were also performed using aluminum alloys. Motoyama and coworkers designed an experiment (shown in Figure 2.3) to study deformations of an aluminum alloy casting resulting from interactions between the sand mold and casting [16,17]. The casting geometry was comprised of a long, narrow bar with a flange, which created a contact interaction at the mold-metal interface and restrained the casting from free contraction. A load cell and LVDT were used to dynamically measure the restraint force and casting contraction, respectively, throughout solidification and cooling. To study gap formation and its affect on heat transfer, Bellet *et al.* [18] dynamically measured displacements at four locations near the mold metal interface of a cylindrical casting with a core (shown in Figure 2.4). Stangeland *et al.* [19] designed an experiment (shown in Figure 2.5), in which two aluminum bars were restrained from thermal contractions by anchor bolts; the tensile force and length change in one of the bars was measured dynamically.

2.3 Previous Models

The first computational model used to predict stresses and mechanical strains in a steel casting was presented by Weiner and Boley [20], who calculated the 1-D thermal

stresses in a semi-infinite slab, from which the temperature field was solved analytically. The plate was constrained from bending and modeled as an elastic-perfectly plastic material. In addition, the yield stress was taken to be a linearly decreasing function of temperature with a value of zero at the solidus temperature. The calculated stresses (compressive near the mold-metal interface but in tension near the solidifying front) exceeded the yield stress and resulted in plastic flow both at the casting surface and near the solidification front. However, this simplified model did not account for corner effects, which are important considerations in a continuous casting process.

Several early computational models studied the coupling between air gap formation (between the mold and casting) and heat transfer at the mold-metal interface. Grill *et al.* [21] coupled the heat flow and deformation in a transverse slice to predict cracks in the solidified shell. Using a plane stress assumption, an elasto-plastic constitutive model calculated gap formations predominantly near the corners, which in turn reduced the heat transfer to create hot spots. Kristiansson [22] expanded on the work of Grill *et al.* by modeling the time-dependent mechanical behavior of steel at high temperatures with a creep model. Kelly *et al.* [23] analyzed the heat transfer and stresses in both the mold and solidifying billet to calculate the air gap. Bellet *et al.* [18] developed a 3-D elasto-visco-plastic model to study gap formation in an aluminum alloy; the model was validated with displacement data collected from an *in situ* casting trial of an aluminum cylinder with a core (shown in Figure 2.4).

Using a creep model, Rammerstrofer *et al.* [24] studied the effects different cooling methods on the stresses after a continuous cast steel billet exited the mold. A reheated strand was found to generate more stresses than a monotonically cooled strand and thus increase the crack susceptibility.

Boehmer *et al.* [25] employed two modeling strategies to calculate stresses and deformations in a continuous casting strand of different materials. For a low thermal conductivity material (i.e., steel) a 2-D transient analysis was performed on several

transverse slices (near the mold outlet) to determine the load history for the stress calculations. For high thermal conductivity materials (i.e., copper), a 2-D steady-state analysis on a longitudinal cross-section of the entire strand was used to model the high thermal gradients along the axis.

Cardona and coworkers implemented an Arbitrary Lagrangian Eulerian (ALE) technique for the time integration in the mechanical problem of a continuous casting strand of steel [26], which was used in subsequent works to compare constitutive models [27] and compare the computation times and performances with a generalized 2-D plane strain formulation [28]. For the former, it was found that the ALE technique incurred higher computational costs while producing similar results as the generalized plane strain formulation. Similarly, Bellet and coworkers also developed an ALE formulation [29], which was used to model the mechanical behavior and macrosegregation of a two-phase mixture of solidifying steel [30].

Thomas and coworkers presented four constitutive relations to model the time-dependent behavior of solidified austenitic steel [31]; all models were fit to the experimental data of Wray [4] and Suzuki *et al.* [5]. Model III was found to be the best compromise (based on its ability to fit the test data and maintain numeric stability) and used in subsequent studies; Li and Thomas [32] developed an in-house finite element code (CON2D) to solve for temperatures, stresses, and strains as a steel billet translates near the mold exit. Koric and Thomas use implicit [33] and explicit [34] time integration methods to solve for stresses and strains during continuous casting processes.

To date, the only study that has used *in situ* dynamic measurements to validate a computational mechanical model of a steel casting was performed by Rowen *et al.* [35], who modeled the submerged split-chill compression (SSCC) test (shown in Figure 2.6). This experiment, which is a simplified version of the SSCT test, characterizes the mechanical behavior of a solidifying steel shell. To validate the model, the simulated and measured forces were matched during solidification. However, because no displacements

are dynamically measured in the SSCC test, the accuracy of the model parameters could not be verified.

Numerous studies have used computational models to predict casting deformations in other metals. Rappaz and coworkers [36,37,38] and Mo and coworkers [19,39,40,41] studied deformations in the DC aluminum castings to predict hot tears. Pokorny *et al.* [42] used a computational deformation model to predict hot tears in a magnesium alloy.

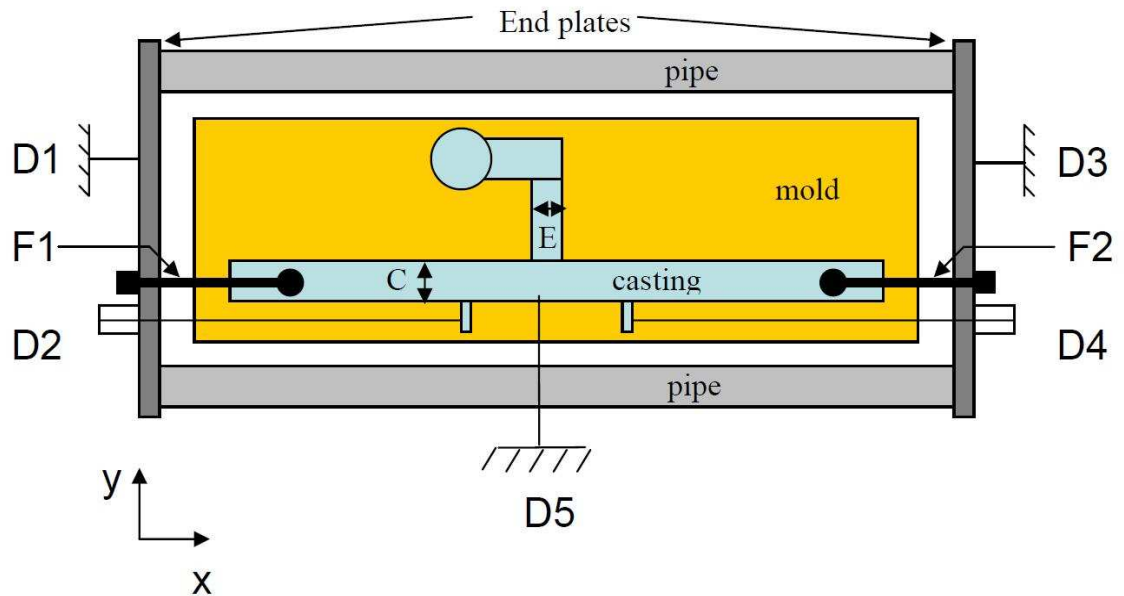


Figure 2.1. Experimental setup of Monroe and Beckermann [11]. A T-shaped casting was restrained from free contraction with a restraint built from two pipes and endplates. Restraining bolts (F1 and F2) were embedded in each end of the casting and connected in series with load bolts, which dynamically measured the restraining force. The casting contraction was transmitted from tabs (which protruded from the casting) via quartz rods and dynamically measured with LVDT's (D2 and D4).

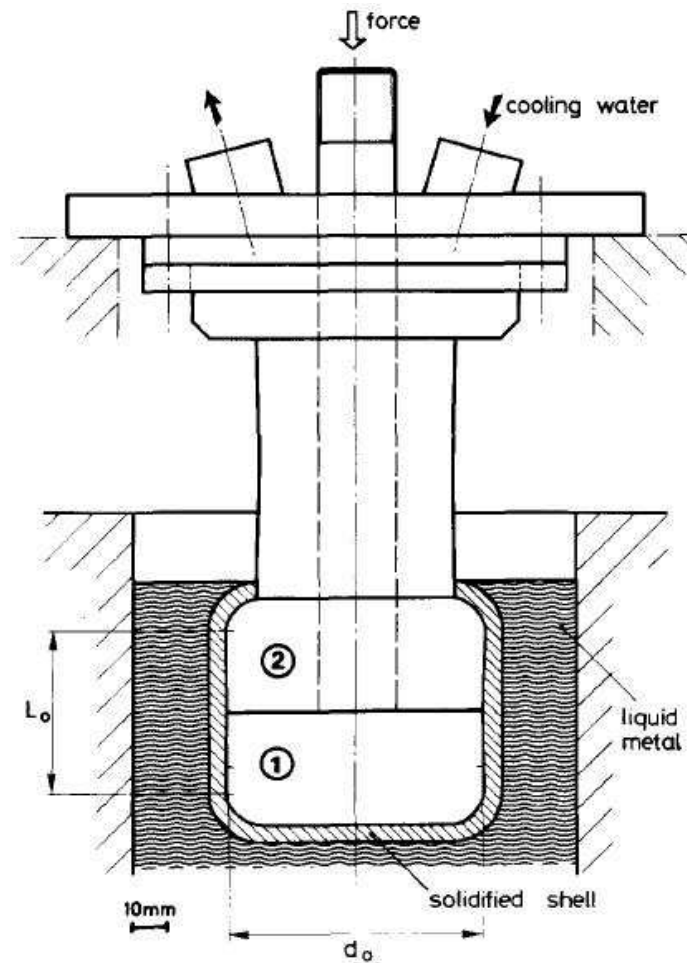


Figure 2.2. Submerged split-chill tensile (SSCT) test developed by Ackermann *et al.* [12]. The two-piece cylinder consists of a stationary upper part (2) and lower part (1). After a shell forms around the cylinders, a downward force is applied to a piston (which is connected to the lower cylinder) to separate the cylinders and deform the solidifying shell. The applied force and piston displacement are dynamically measured.

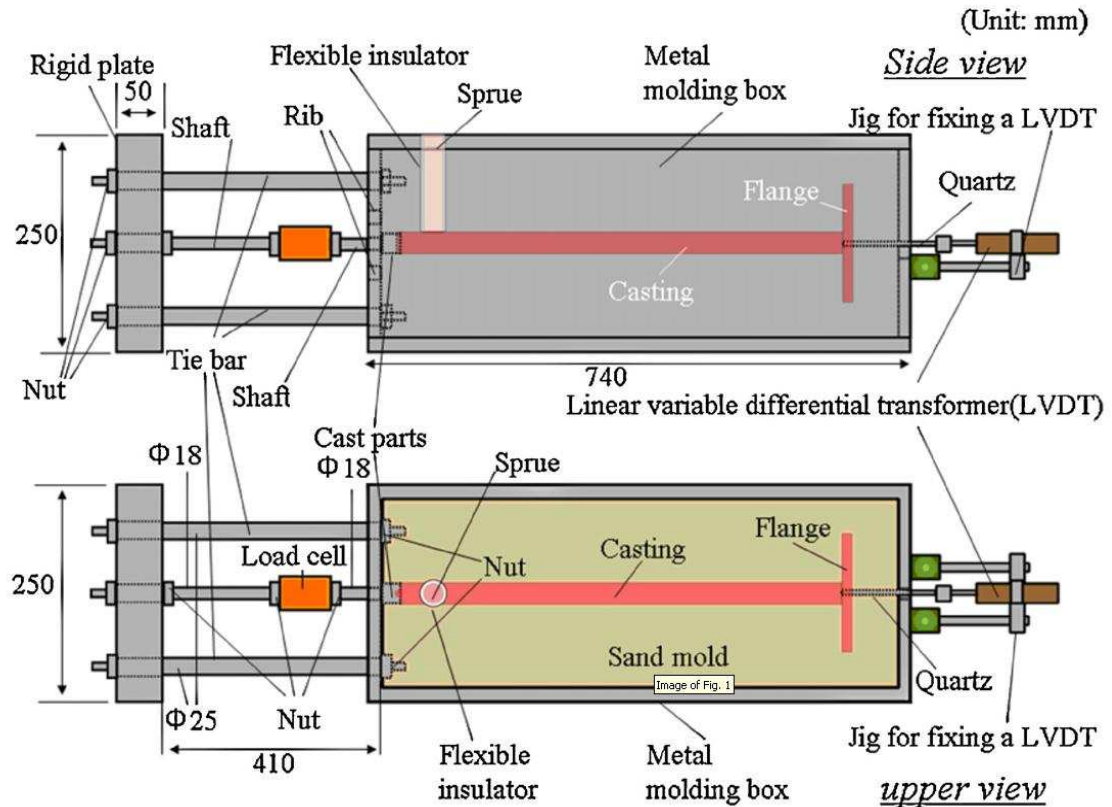
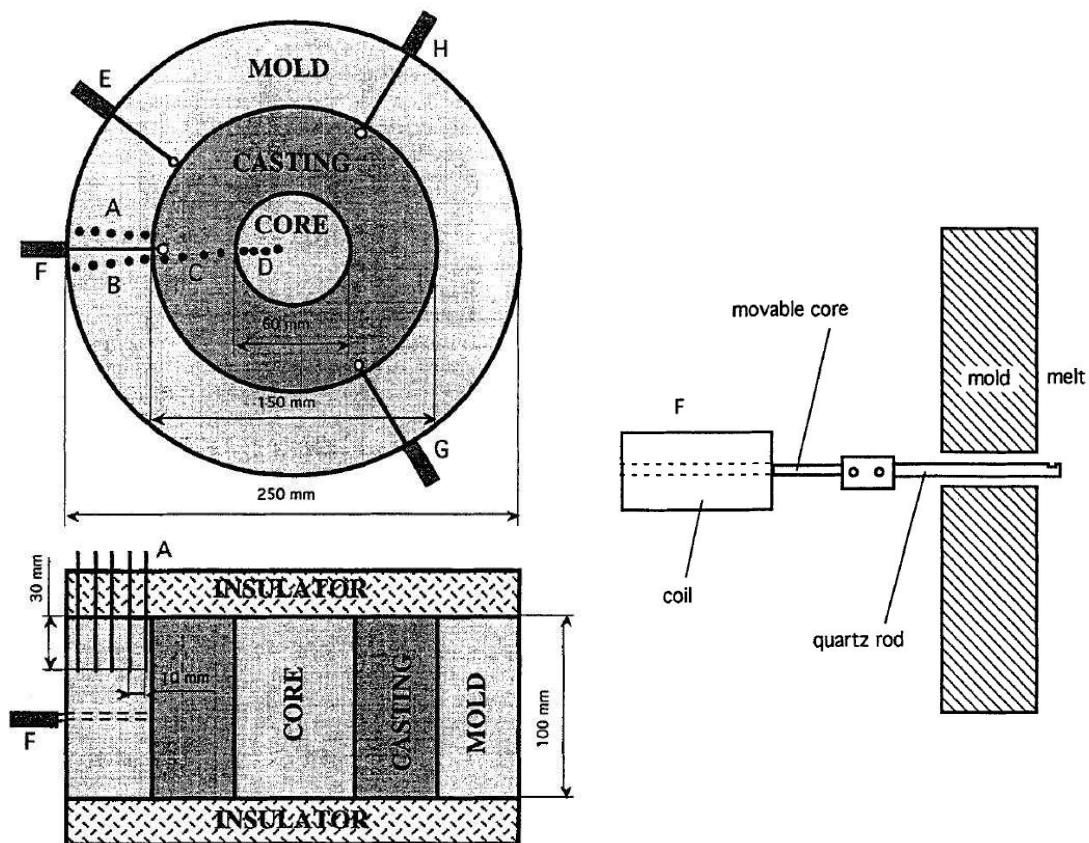


Figure 2.3. Experimental setup of Motoyama and coworkers [16,17]. To characterize the material behavior of a solidifying aluminum alloy in a sand mold, an experiment was devised to generate axial forces through the casting resulting from mold-metal interactions at the flange. The length change in the casting and axial forces were measured with an LVDT and a load cell, respectively.



(a) Aluminum Casting with a Core

(b) Displacement Transducer

Figure 2.4. Experimental setup of Bellet *et al.* [18]. Displacement transducers (E, F, G, H) were placed at the mid-height of the casting near the mold metal interface to dynamically measure gap formation between the casting and mold.

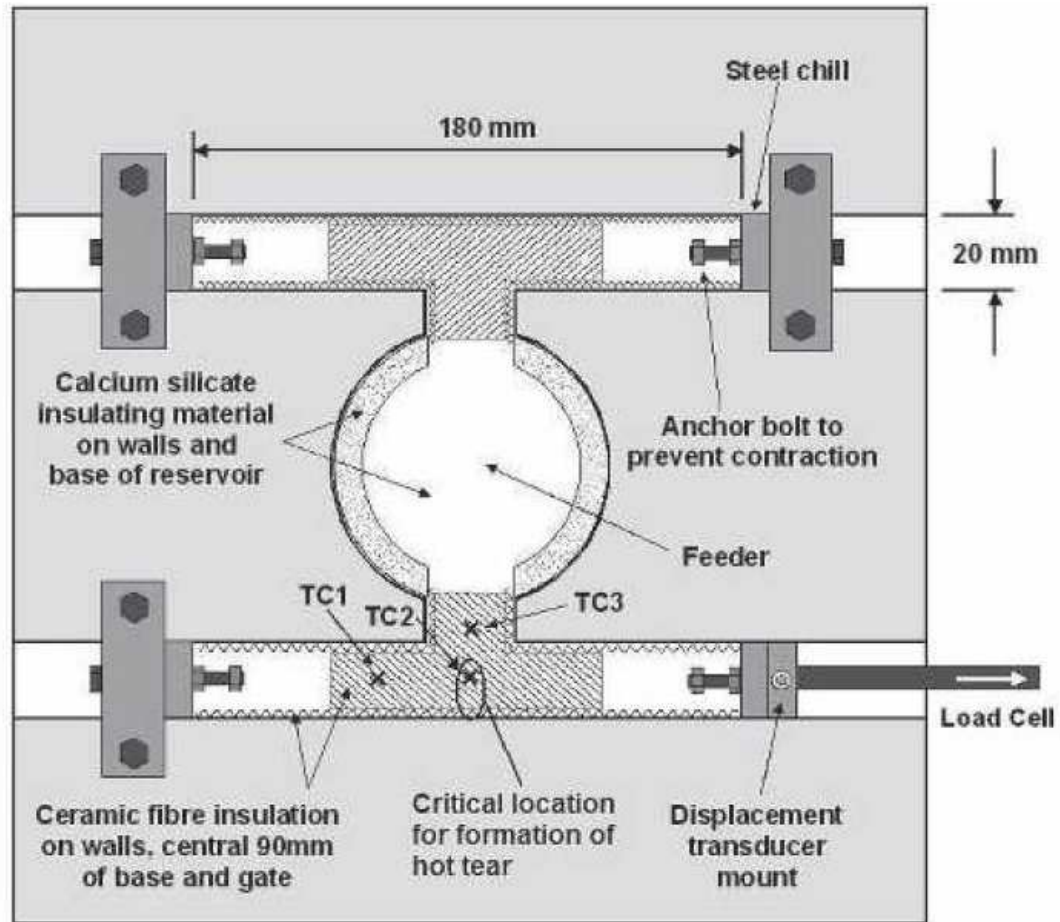


Figure 2.5. Top view of the experimental setup of Stangeland *et al.* [19]. Two aluminum bars were cast and fed from a cylindrical feeder. Anchor bolts were used to prevent thermal contractions. The axial force and length change of the lower bar were measured dynamically.

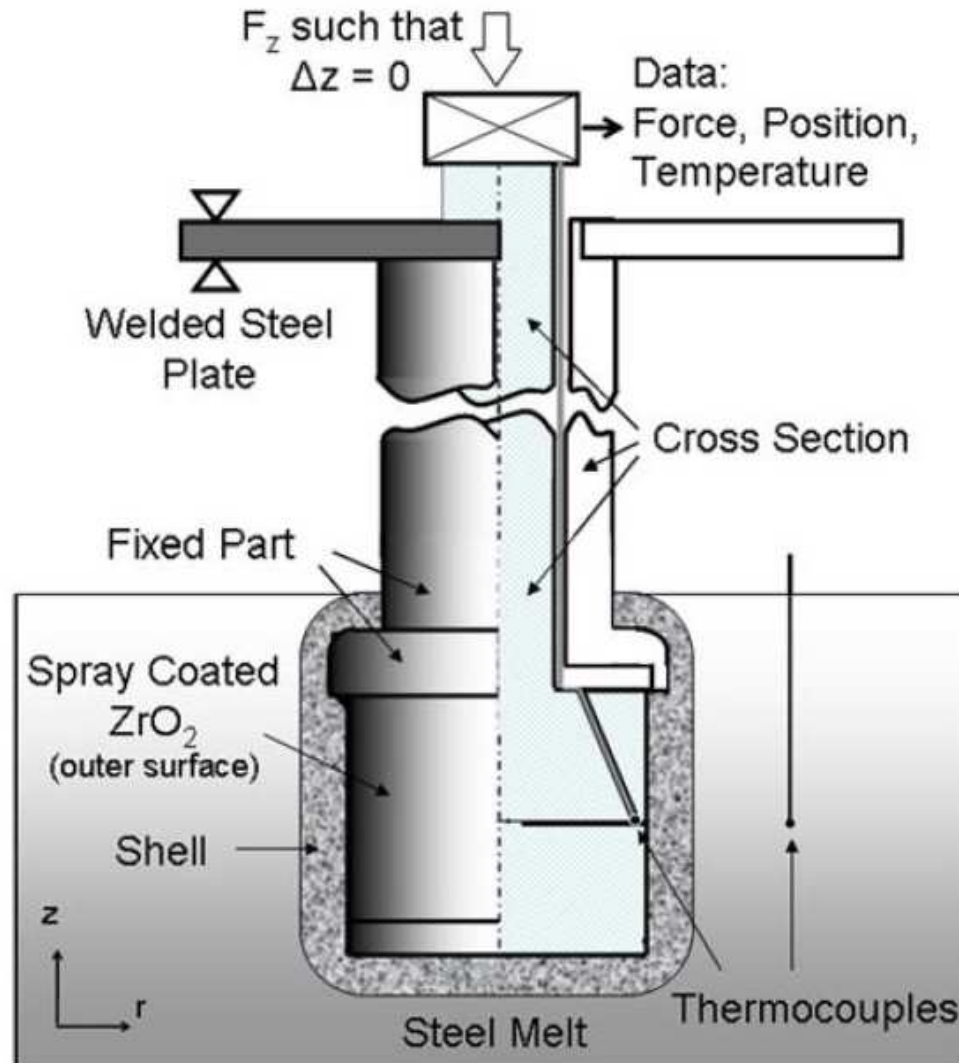


Figure 2.6. Schematic of submerged split-chill compression (SSCC) test. This is a simplified version of the SSCT test (developed by Ackermann *et al.* [12]). During solidification, the required force (F_z) to maintain the vertical position at the top of the assembly is measured dynamically.

CHAPTER 3: DESCRIPTION OF EXPERIMENTS

3.1 Introduction

The ability of a computational model depends on how closely the experiments (which are used for validation) capture physical phenomenon. Clearly, a mechanical test (in which reheated, homogeneous specimens under isothermal conditions are plastically deformed) cannot recreate the harsh conditions of an industrial casting process. Therefore, in order to collect meaningful data, *in situ* casting trials were performed. This chapter thoroughly explains the experimental setup (Section 3.2), casting procedure (Section 3.3), and experimental results (Section 3.4).

3.2 Experimental Setup

The experimental design was motivated from the presumption that total strain, ε_{total} , is decomposed into the sum of its mechanical, ε_{mech} , and thermal, ε_{th} , parts, shown as

$$\varepsilon_{total} = \varepsilon_{mech} + \varepsilon_{th} \quad (3.1)$$

Because mechanical and thermal strains arise from different types of loading (and are thus calculated differently in the simulations), conducting separate *in situ* experiments to measure each component of the total strain is desirable. However, while it is possible to measure thermal strain in the absence of mechanical strain, the opposite would be very difficult. Consequently, two experimental setups, termed “Unrestrained” and “Strained”, were created (shown in Figure 3.1). While castings produced from the Unrestrained setup (experimental control) were designed to experience free contraction, the combination of a restraint and induced force (from a turnbuckle) generated plastic deformations in the Strained castings. Experiments of both setups produced a steel bar of identical dimensions (12 inches long with a 1-inch square cross section). Figure 3.2 shows isometric views of the experimental setups, while mold dimensions and are shown in Figure 3.3. Additionally, two sprue diameters (1-inch and 1.5-inch) were used in the

Strained experiments to create different temperature gradients along the axis of the bar; all Unrestrained experiments used a 1-inch sprue.

Because the computational model (which will be described in Chapter 5) predicts deformation in the mushy zone, it was critical to induce stresses before solidification was complete. At some time during solidification, the steel reaches a level of coherency and can transmit forces; stresses incurred before this time will likely result in casting failure. Because the casting was small (and therefore cooled quickly), a narrow window existed between the coherency and solidification times. Therefore, through a trial-and-error method, the turnbuckle was engaged at different times to collect force and displacement data after the “time to coherency” but before complete solidification.

The setups in Figure 3.1 were outfitted with a number of measurement devices to acquire temperature, force, and displacement data. Temperatures in the casting were measured using type B thermocouples, which were encased in quartz tubing to protect the thermocouple wires from the molten steel. Thermocouple placement is shown in Figure 3.3. In order to differentiate the temperature measurements, the thermocouple locations are termed “Sprue” and “Right”, as shown in Figure 3.3(a).

Force measurements were acquired with an Omega LCS-1/2-2L load bolt embedded on each side of the restraint and connected in series with a restraining bolt (constructed from half-inch threaded steel rod and cut to an appropriate length). Nuts were threaded onto the ends of the restraining bolts inside the mold cavity to act as anchors and minimize slippage resulting from tensile forces induced by the turnbuckle. The restraining bolts were connected to the load bolts with a coupling and turnbuckle on the left and right sides, respectively. Care was taken to axially align the restraining bolts with the casting.

Displacement was measured with an Omega LD620-5 LVDT (linear variable differential transformer) at each end of the mold. A 3 mm diameter quartz rod was connected at one end to the LVDT, while the other end was inserted 3-5 mm into the

mold cavity. To ensure the quartz rod did not slip in the casting, the end of the rod was bulged into a spherical shape using an oxy-acetylene torch. While quartz is a suitable material to use in this application because of its high melting point and low thermal expansion, it is also extremely brittle. The quartz rods frequently broke during the experiments due to the build-up of compressive stresses as the casting cooled. To alleviate this problem, protective metal sleeves were inserted over the bulged ends inside the mold cavity. The axial length change in the bar was calculated by adding the displacements measured from the two LVDT's. Note from Figure 3.1 that the LVDT supports were not in contact with the restraint. This assured that the relative displacement measured by the LVDT's was from the casting itself and not the restraint.

The mold boxes and patterns were built from wood. A cope and drag were produced for each setup, which can be seen in Figure 3.3(b). The horizontal parting plane coincided with the top of the casting. In order to avoid drilling holes through the solidified molds (to insert the thermocouples, restraining bolts, and quartz rods), holes were drilled in the mold box, through which steel rods were inserted into the pattern before filling the mold box with bonded sand. After the molds solidified, the steel rods, mold box, and pattern were removed, and the measurement hardware was inserted at the appropriate locations. Using a drill, a vertical hole was drilled through the cope to serve as the sprue. The cope, drag, and a pouring cup (also built with bonded sand) were assembled and held in place with a foundry paste. Weights were placed on top of the cope to minimize flashing.

To build the molds, Unimin IC55 silica lake sand was bonded with a phenolic urethane no-bake (PUNB) binder system and mixed in a Palmer M-50 no-bake continuous mixer. The binder accounted for 1.25% of the total mold weight and was mixed using a 55:45 ratio of Part 1 (Pep Set 1000) to Part 2 (Pep Set 2000). The chemical reaction was accelerated with a catalyst (Pep Set 3501) based on 6% of binder weight.

The molds were designed to contain symmetry about the vertical planes that cut

through the mid-depth and mid-length of the casting, shown by the CAD drawing in Figure 3.2(a). In addition, due to the casting's small mass (less than 10 kg), frictional forces between the casting and mold were neglected. Therefore, because of the mold design, mechanical strains were 1) neglected in the Unrestrained experiments, and 2) generated only from the induced forces of the turnbuckle in the Strained experiments.

Experimental data was collected using an IOtech model 3005 Personal DAQ system connected to a laptop computer and acquired with DASyLab [43] software. A sampling rate of 2 Hz was used at high temperatures and switched to 0.5 Hz at lower temperatures (< 800 °C).

3.3 Casting Procedure

Experimental casting trials were performed at the University of Northern Iowa's Metal Casting Center. The target chemistry was ASTM A216 grade WCB carbon steel. The castings were poured from a 250 lb heat and prepared in an induction furnace. Because of the heat loss encountered during the transfer from the furnace to pouring ladle, the molten steel was heated to approximately 1700°C. The castings were poured within four hours after building the molds. Immediately before pouring, any slag was removed from the ladle. With the exception of the final casting trial, the liquid steel was transferred from the pouring ladle to a smaller hand-held ladle and then poured into the mold. However, this additional step resulted in further heat loss (which will be explained in detail in the following section). Therefore, in an attempt to retain this heat, the mold in the final casting trial was filled directly from the pouring ladle.

3.4 Experimental Results

In total, nine casting trials were performed (3 Unrestrained, 6 Strained). In order to distinguish between individual casting trials, each experiment will be identified by its type (Unrestrained or Strained) followed by a number. Table 3.1 provides a summary of all casting trials, including the diameter of the sprue and casting chemistry.

Examples of the Strained and Unrestrained castings are shown in Figure 3.4; with the exception of the threaded rods protruding from the ends of the Strained bar, the castings are essentially identical. Radiographs of the Strained 1 (1-inch sprue) and Strained 4 (1.5-inch sprue) casting trials are shown in Figure 3.5. The two small circular shapes on each radiograph show the thermocouple locations. While the Strained 1 radiograph looks to be sound, the Strained 4 radiograph appears to have accumulated significant damage to the right of the sprue. This damage, which will affect the stress simulations, will be discussed in detail in Chapter 6.

All experimental results are shown on large (12000 s), medium (1600 s) and small (250 s) time scales to illustrate the occurrence of different events during solidification and cooling. Temperatures from the thermocouples at the Sprue (termed T_{sprue}) and Right (termed T_{right}) locations of the casting are plotted as functions of time in Figure 3.6 and Figure 3.7, respectively. While a distinct difference is seen in cooling times of the large-sprue and small-sprue castings at the Sprue location, the differences at the Right location are more subtle. Also, differences in experimental conditions (i.e., pouring temperature, casting chemistry, amount of metal in the pouring cup) created additional (slight) variances between each casting trial.

The evolution of the temperature curves can be explained by referring to the “Strained 6” curve in Figure 3.6 and Figure 3.7. A sharp peak is seen after a few seconds at the Sprue location, shown in Figure 3.6(c), as the temperature increased to a maximum of approximately 1550°C before rapidly decreasing to the so-called liquidus temperature (T_{liq}). At this temperature, the liberation of latent heat reduced the cooling rate to nearly zero to indicate the onset of solidification. Hence, the liquidus temperature was experimentally determined at this arrest. A similar plateau can be seen in the “Strained 6” curve at the Right location, as shown in Figure 3.7(c). Although no peak appears at the Right location, the arrest occurred at the same temperature (1482°C) as the Sprue location, thus verifying T_{liq} . Because of its pronounced peak in the temperature

curve, the Strained 6 casting trial was the only experiment in which the liquidus temperature could be experimentally determined. No peak is seen in the other temperature curves due to one or more of the following reasons: (1) the superheat was not large enough, (2) the thermocouples had a delayed response time due to physical limitations, and (3) the casting size was small and cooled quickly. In Strained 1-5 casting trials, the molten steel was transferred from a large ladle to a smaller ladle before pouring the castings in an effort to protect the experimental equipment. However, this resulted in a significant loss of superheat. In the Strained 6 experiment, however, the casting was poured directly from the large ladle. Additionally, 4 mm diameter quartz tubes were used (rather than 6 mm tubes for the previous experiments) to protect the type B thermocouples, which reduced the response time.

The solidus temperature (T_{sol}), which represents the end of the solidification period, was experimentally determined as the temperature at which the maximum cooling rate occurred. The cooling rate curves, shown in Figure 3.8, were calculated as the temperature change per time step and plotted as functions of measured temperature. Because the exact temperature at maximum cooling rates can be difficult to determine from the cooling rate curves, the solidus temperature should be viewed as an approximate value whose accuracy is within a few degrees of the actual solidus temperature. In addition, whereas the liquidus temperature depends on the casting chemistry only, the solidus temperature depends on a number of factors including casting chemistry, cooling rate, and microsegregation. As a result, T_{sol} varied between the Sprue and Right locations, as shown in Table 3.2.

Upon further cooling, the solid-state phase transformation from austenite to pearlite and proeutectoid ferrite caused another temperature arrest (at approximately 675°C), which can be seen on the medium and large time scales in Figure 3.6 and Figure 3.7.

Displacement results, plotted as the axial length change of the bar as a function of

time, are shown in Figure 3.9. Results on the large time scale show excellent reproducibility of all Unrestrained experiments, as the curves essentially lie on top of each other. Slight differences are seen at the solid-state transformation (characterized by the “wiggles” at approximately 1500 s), which were primarily the result of differences in the casting chemistry. Additionally, the percent length change of the Unrestrained experiments was approximately -2.15%, which is close to the free shrink of steel. In the Strained experiments, the effect of the applied turnbuckle force can be seen in Figure 3.9(c). Before the turnbuckle was turned ($t < 50$ s), the axial lengths of all Strained experiments decreased with time (due to thermal contractions of the bar). As the turnbuckle was turned, however, the axial length change increased with time, as the applied force induced mechanical strains, which counteracted the thermal contractions and lengthened the bar. Because the forces were applied at different magnitudes and times, the axial length changes varied between Strained experiments. After the induced straining period, the measured axial length briefly continued to increase (likely due to creep effects) before decreasing as thermal contraction dominated the total strain. Upon reaching the solid-state transformation, the steel significantly increased in strength and the stresses in the bar were no longer sufficient to generate plastic strains. As a result, the Strained and Unrestrained curves are nearly parallel after the transformation, shown in Figure 3.9(c).

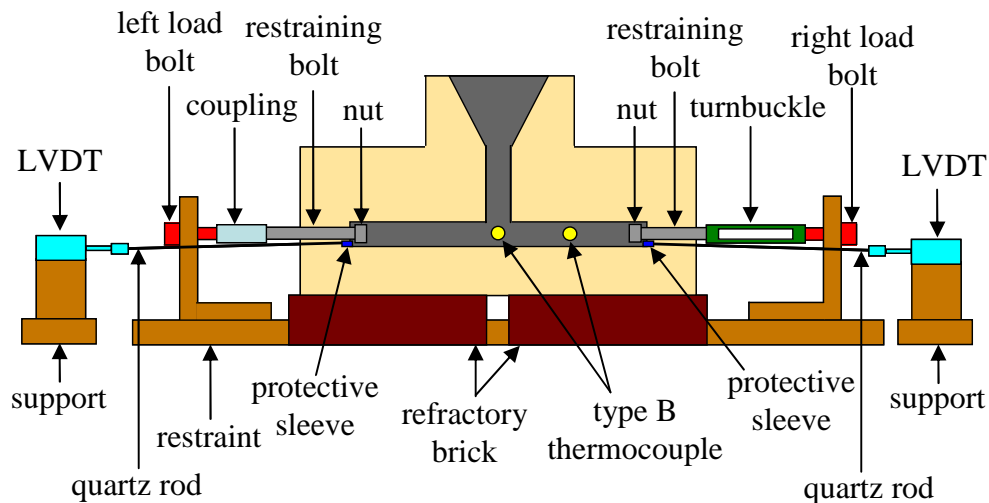
An interesting phenomena of all displacement curves occurred a few seconds after the casting was poured. The LVDT's measured a brief, but steep, decrease in the displacement beginning at 5 seconds and continued for approximately 20-30 s, after which the slopes flattened. Because it is unlikely that the bar had solidified into a coherent network after only a few seconds, this initial displacement cannot be explained by thermal contractions. Rather, this brief contraction could have been the result of mold's thermal expansion upon heating, which acted to “squeeze” the liquid metal out of the mold cavity and into the pouring basin. As a result, the quartz rods, which were

embedded in the ends of the bar, translated inward to result in a negative displacement reading. Because it was neither the result of thermal or mechanical strains, this initial displacement will not be considered in the comparison measured and simulated displacements (to validate the stress model).

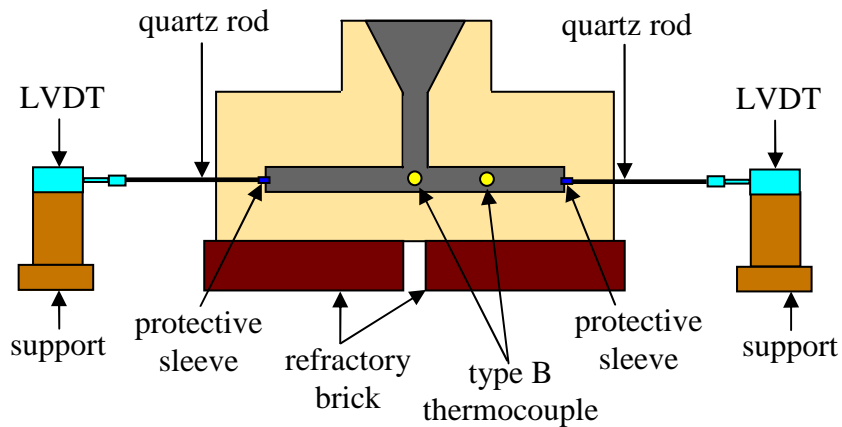
Measured forces from the Left (non-turnbuckle side) load bolt of the Strained schematic (shown in Figure 3.1(a)) are plotted as a function of time and shown in Figure 3.10. Nominal stresses, calculated as the force divided by the initial cross-sectional area, are included on the right vertical axes of the plots. Figure 3.10(c) shows the forces increased dramatically throughout the induced straining period, after which they continued to increase, albeit at a slower rate. This increase in forces occurred as the result of thermal contractions in the bar. The solid-state transformation can readily be seen on the medium time scale, shown in Figure 3.10(b), as the familiar wiggle that was also seen in the displacement curves.

By comparing measurements from the Left (non-turnbuckle side) and Right (turnbuckle side) load bolts shown in the Strained schematic (Figure 3.1(a)), a force imbalance, shown in Figure 3.11, reveals the existence of an interaction between the mold and casting. This interaction, which occurred between the sprue and mold, was initiated during the induced straining period. To understand the curves in Figure 3.11, further explanation is required of how the turnbuckle worked; to engage the turnbuckle, a ratcheting wrench was used to apply a torque and turn the turnbuckle. After the turnbuckle was rotated for a partial turn, the wrench was ratcheted (released) and then turned again to generate additional stresses. During the time which torque was applied, the Left and Right measured forces were balanced, as no interaction occurred. However, when the wrench was released, the mold contacted the sprue, resulting in the force imbalance. Therefore, as the wrench was turned, mechanical strains likely created a gap between the sprue and mold. Because the binder at the mold-metal interface had already evaporated, loose grains of sand may have fallen into the gap. As the wrench was

ratcheted, the release of elastic strains may have caused the sprue to rest against the mold and transmit a force at the mold-metal interface. To model this interaction in the stress simulations, a force boundary condition will be created at the base of the sprue (described in Chapter 6).

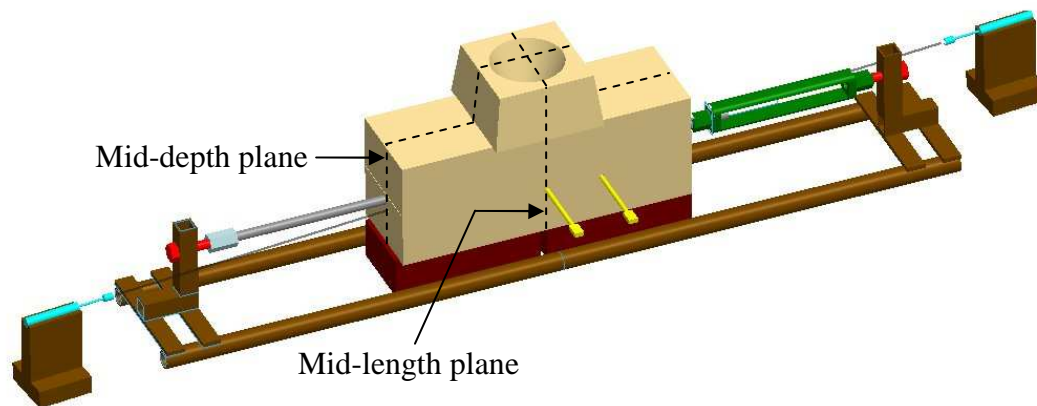


(a) Strained

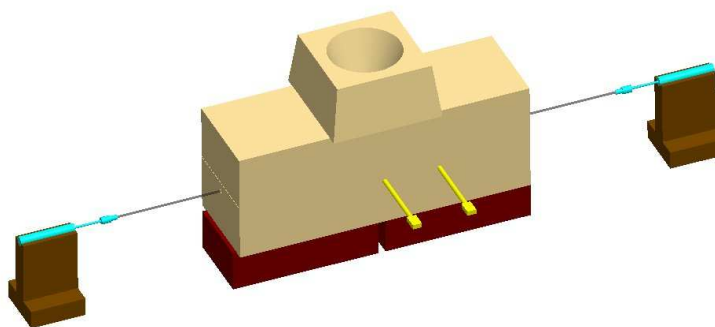


(b) Unrestrained

Figure 3.1. Schematic of Strained and Unrestrained experimental setups at the casting mid-plane. Displacements and forces were measured with LVDT's (Linear Variable Differential Transformer) and load bolts, respectively. Temperatures were measured in the steel with type B thermocouples.

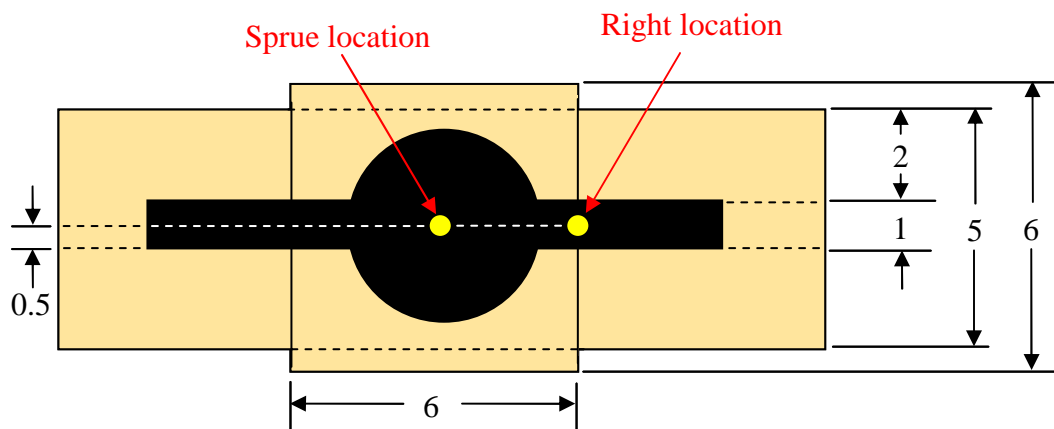


(a) Strained

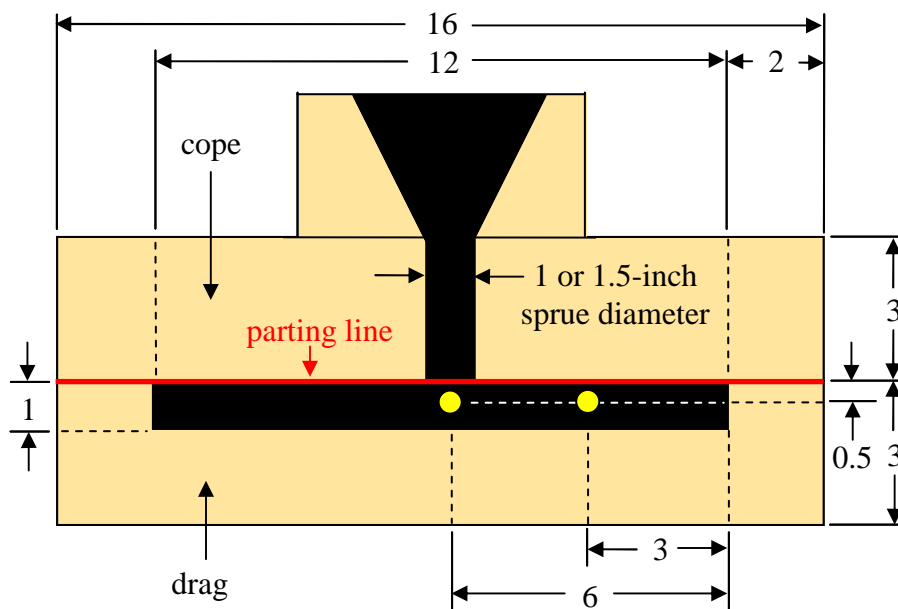


(b) Unrestrained

Figure 3.2. Pro-E drawings of the isometric view of the Strained and Unrestrained experimental setups. The molds were designed to contain symmetry about the mid-depth and mid-length vertical planes to minimize mold-metal interactions.



(a) Top view



(b) Front view

Figure 3.3. Mold dimensions and thermocouple placement for the Strained and Unrestrained setups. All dimensions are in inches. The yellow circles represent the thermocouple locations. The sprue diameter for Strained 4, 5, and 6 casting trials was 1.5 inches. All other casting trials used a 1-inch sprue diameter.

Table 3.1 Summary of sprue diameter and casting chemistry for all casting trials.

	Sprue Diameter (inches)	Casting Chemistry								
		%C	%Si	%Mn	%P	%S	%Cr	%Al	%Cu	%Fe
Unstrained 1	1	0.21	.050	0.52	0.072	0.002	0.08	0.070	0.08	bal.
Unstrained 2	1	0.32	0.69	0.64	0.025	0.014	0.23	0.054	0.10	bal.
Unstrained 3	1	0.25	0.59	0.55	0.012	0.014	0.04	0.069	0.04	bal.
Strained 1	1	0.25	0.58	0.62	0.022	0.016	0.03	0.087	0.05	bal.
Strained 2	1	0.25	0.61	0.56	0.021	0.017	0.10	0.071	0.08	bal.
Strained 3	1	0.25	0.45	0.46	0.019	0.017	0.04	0.045	0.03	bal.
Strained 4	1.5	0.20	0.41	0.42	0.015	0.009	0.01	0.028	0.04	bal.
Strained 5	1.5	0.41	2.76	0.39	0.089	0.031	0.01	0.035	0.75	bal.
Strained 6	1.5	0.30	0.57	0.41	0.031	0.026	0.02	0.056	0.01	bal.

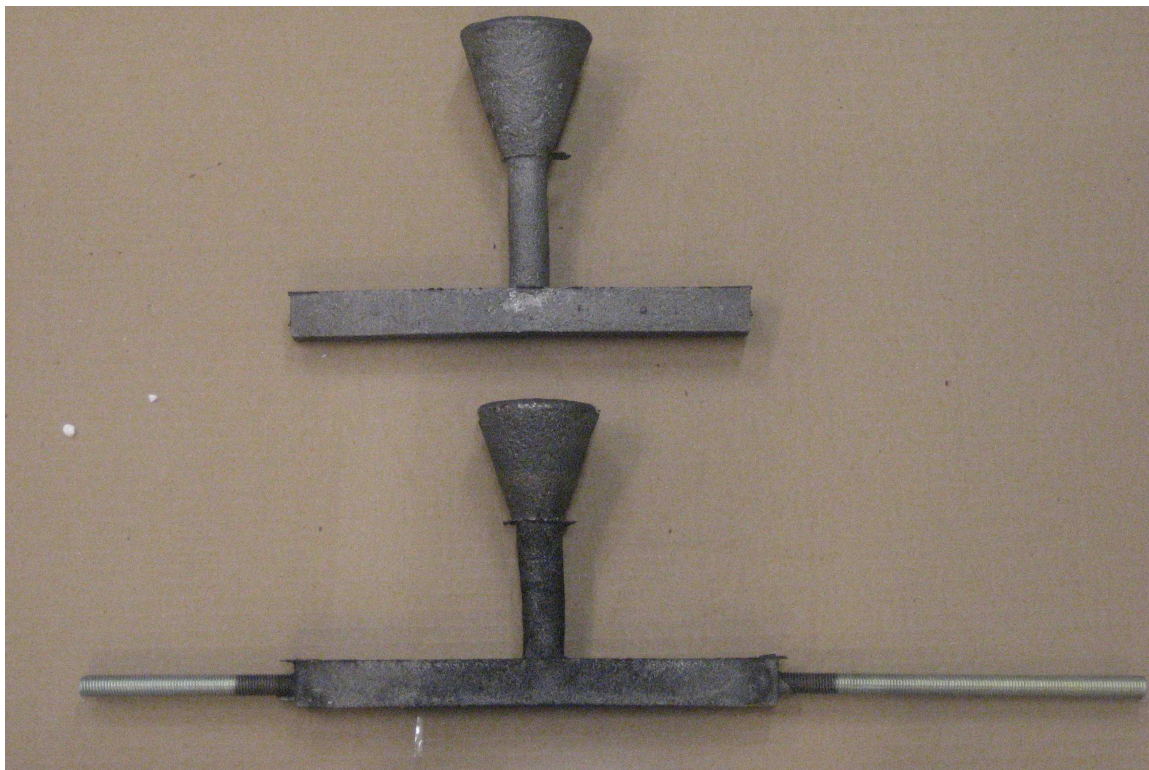
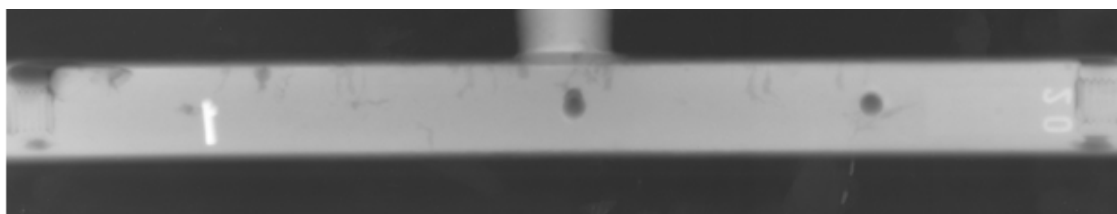
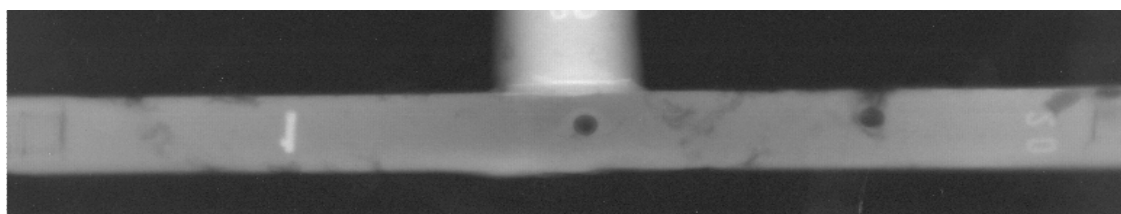


Figure 3.4. Examples of the Unrestrained and Strained castings.

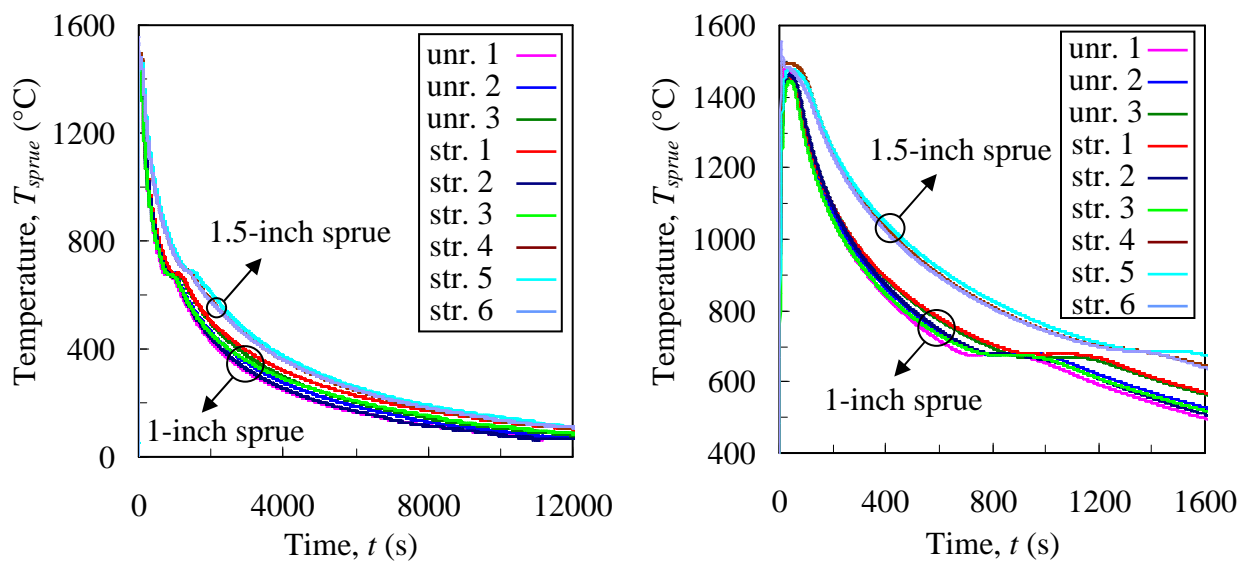


(a) 1-inch sprue



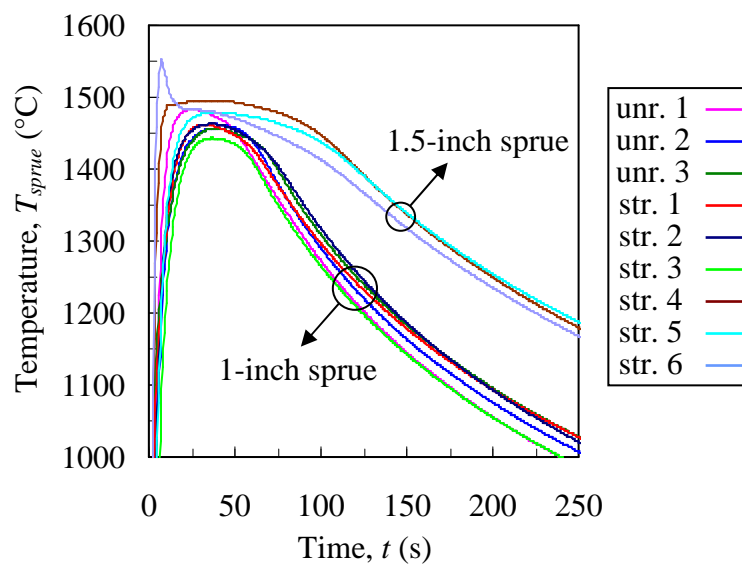
(b) 1.5-inch sprue

Figure 3.5. Radiographs of the large-sprue and small-sprue Strained castings.



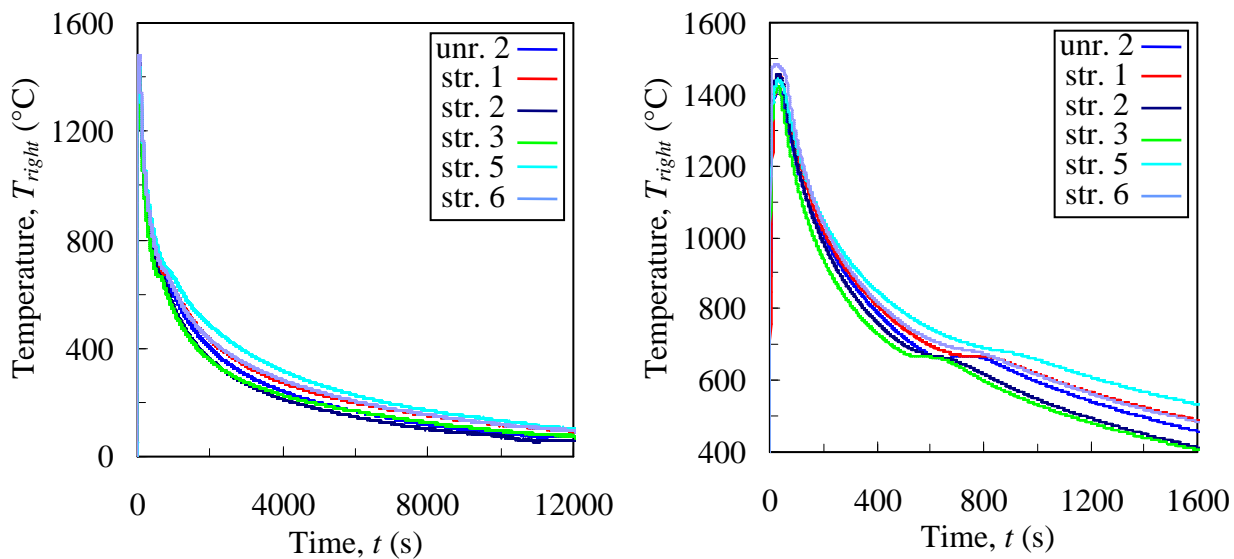
(a) Large time scale

(b) Medium time scale



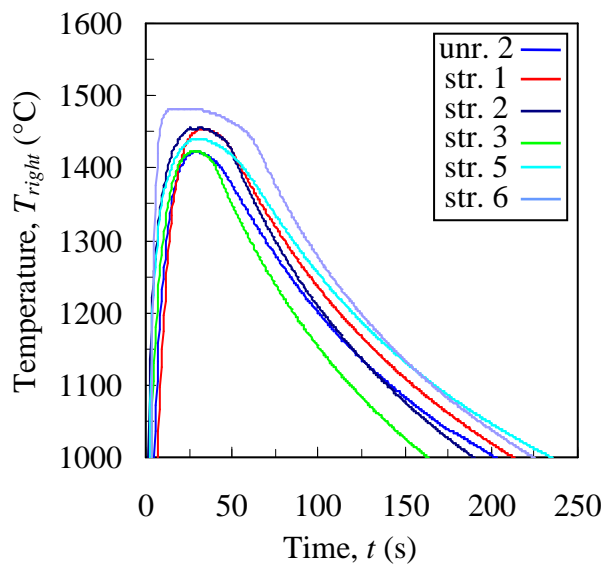
(c) Small time scale

Figure 3.6. Measured temperature results at the Sprue location (shown on the schematic in Figure 3.3) of the Unrestrained (unr.) and Strained (str.) casting trials on large (12,000 s), medium (1600 s), and small (250 s) time scales.



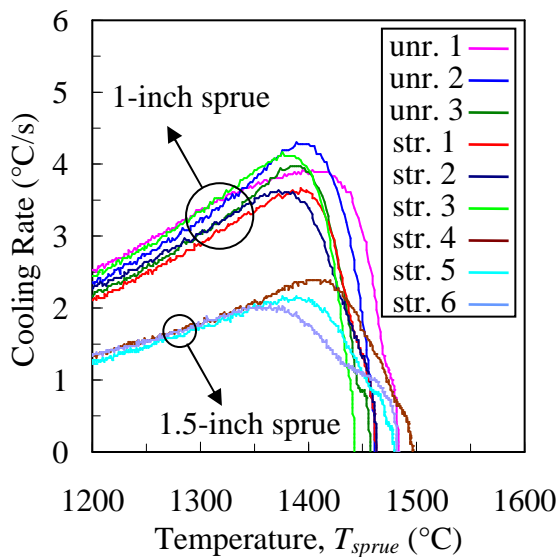
(a) Large time scale

(b) Medium time scale

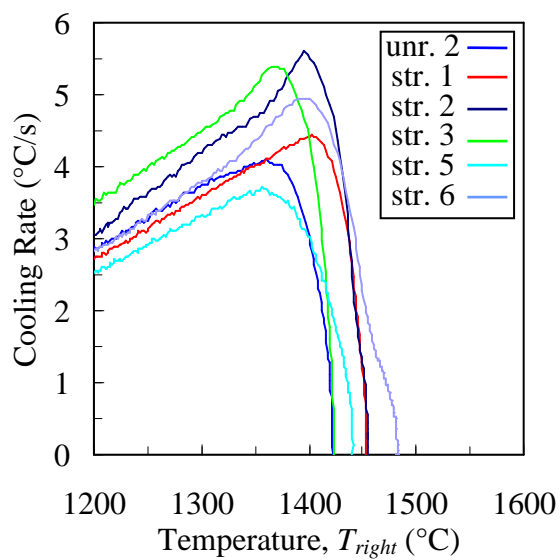


(c) Small time scale

Figure 3.7. Measured temperature results at the Right location (shown on the schematic in Figure 3.3) of the Unrestrained (unr.) and Strained (str.) casting trials on large (12,000 s), medium (1600 s), and small (250 s) time scales.



(a) Sprue location

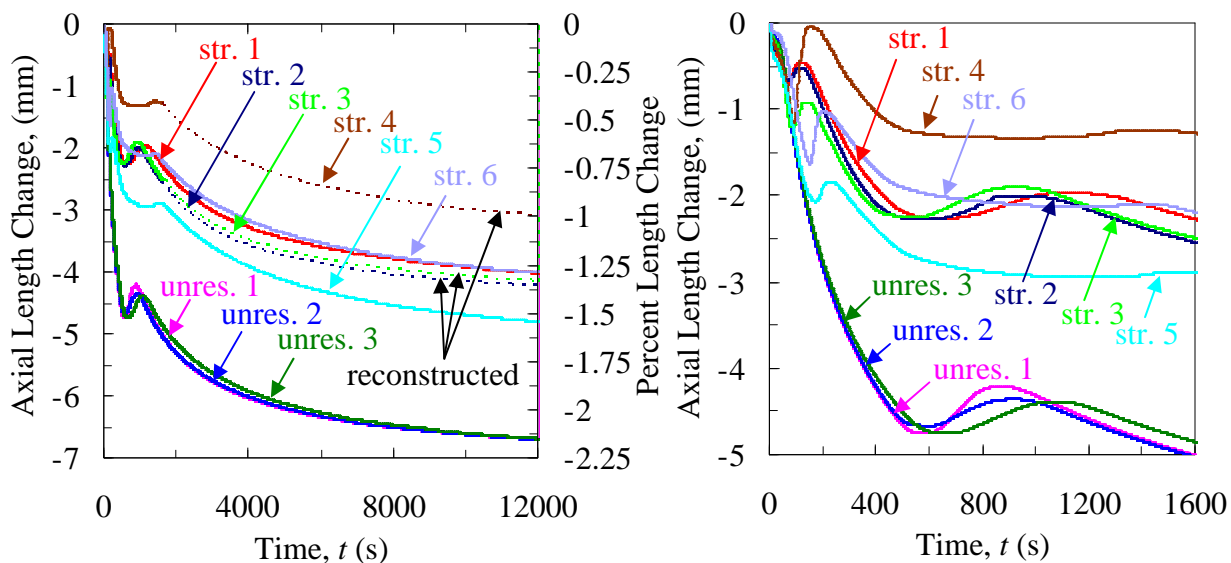


(a) Right location

Figure 3.8. Cooling rates of the Unrestrained (unr.) and Strained (str.) bar experiments at the Sprue and Right locations. The approximate solidus temperature is experimentally determined as the temperature at which the maximum cooling rate occurs.

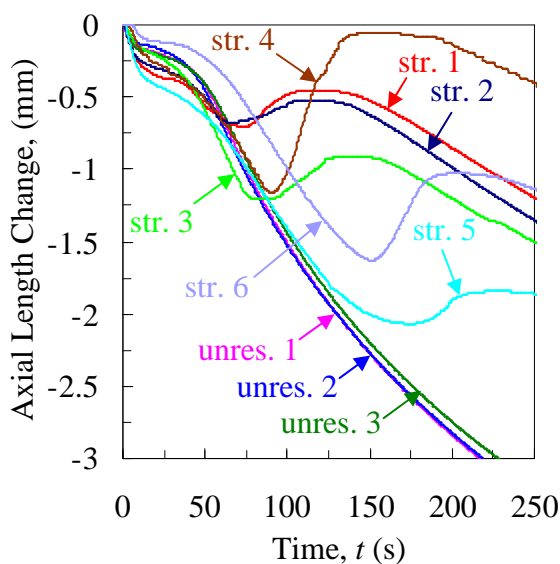
Table 3.2 Summary of solidus temperatures. Solidus temperatures were experimentally determined as the temperature at the maximum cooling rates.

	Solidus Temperature	
	Sprue Location (°C)	Right Location (°C)
Unrestrained 1	1413	N/A
Unrestrained 2	1396	1362
Unrestrained 3	1391	N/A
Strained 1	1396	1405
Strained 2	1378	1395
Strained 3	1385	1369
Strained 4	1409	N/A
Strained 5	1390	1359
Strained 6	1375	1395



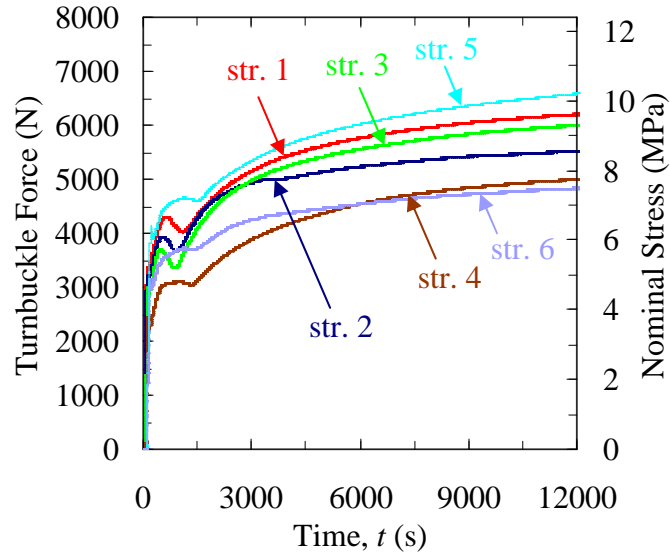
(a) Large time scale

(b) Medium time scale

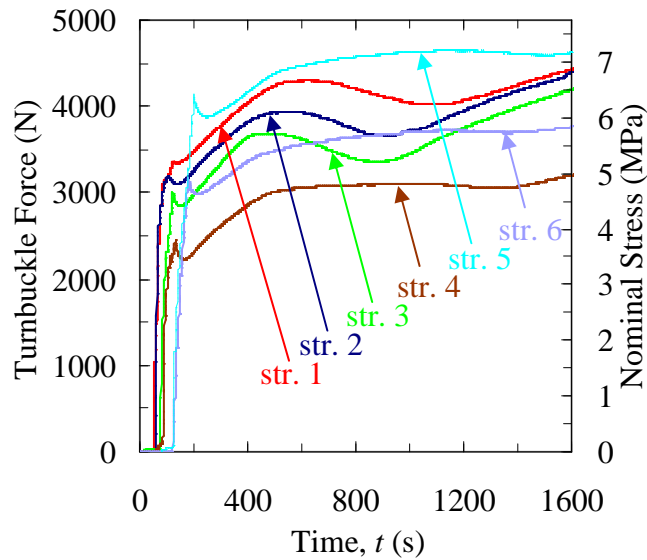


(c) Small time scale

Figure 3.9. Measured axial length changes of the Strained (str.) and Unrestrained (unres.) bars on large (12,000 s), medium (1600 s), and small (250 s) time scales. As force is applied during the Strained experiments, the axial length change increases with time, as seen on the small time scale. The increasing axial length change seen after 600 s (on the medium time scale) is the result of the solid-state transformation.

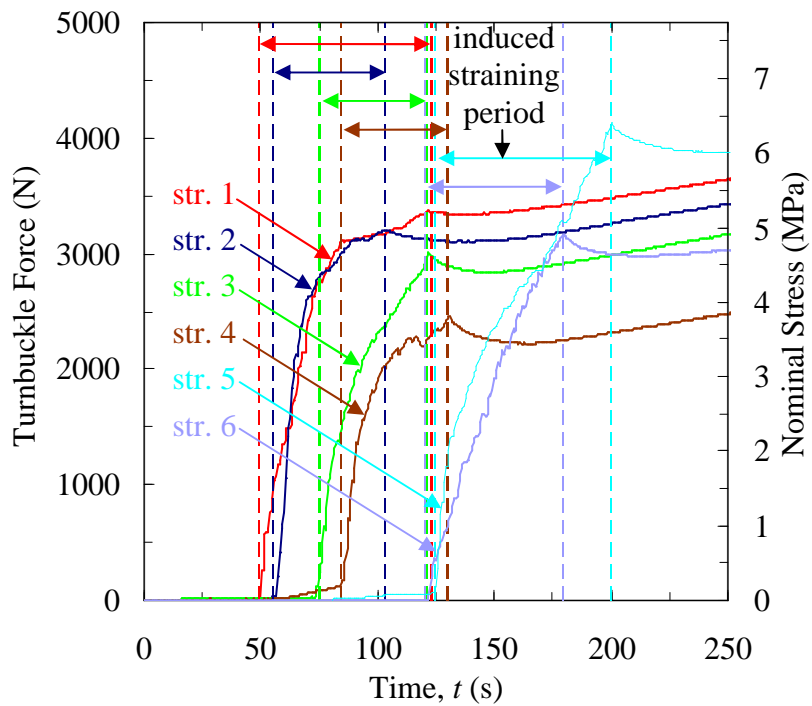


(a) Large time scale



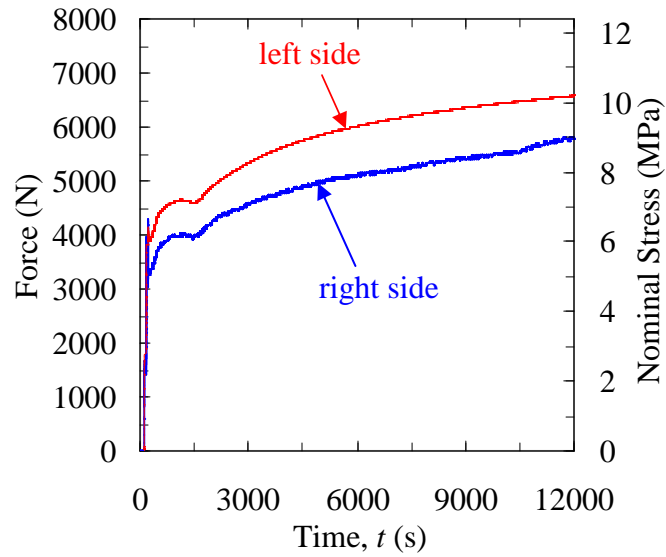
(b) Medium time scale

Figure 3.10. Measured Left turnbuckle forces (shown on the schematic in Figure 3.1) of the Strained experiments at the Right location on large (12,000 s), medium (1600 s), and small (250 s) time scales. The decreasing force seen after 600 s (on the medium time scale) is the result of the solid-state transformation. The induced straining period (shown on the small time scale) shows the different times and durations for which the turnbuckle was turned.

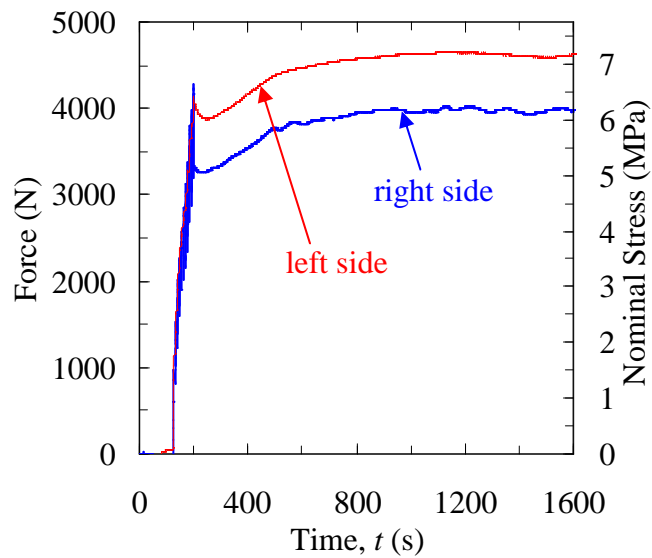


(c) Small time scale

Figure 3.10 (continued).

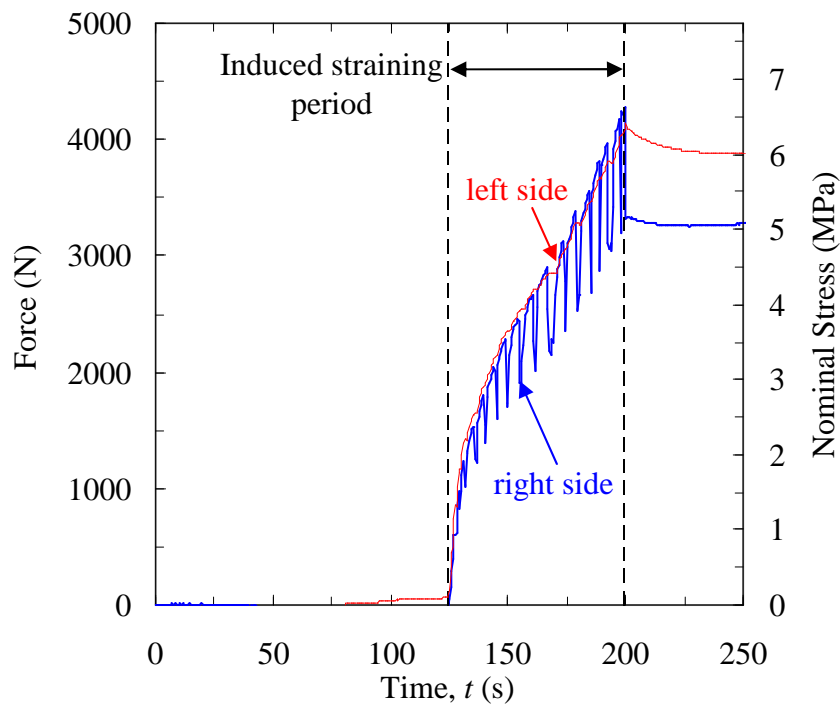


(a) Large time scale



(b) Medium time scale

Figure 3.11. Comparison of Left and Right (shown on schematic in Figure 3.1) load bolt forces from the Strained 4 experiment. This difference in forces, which was typical of all Strained experiments, was the result an interaction between the mold and the sprue.



(c) Small time scale

Figure 3.13 (continued).

CHAPTER 4: THERMAL SIMULATIONS

4.1 Introduction

The mathematical model for the present study is based on the volume-averaged conservation equations of Ni and Beckermann [44]. Through a decoupling, these equations are solved in a sequential process, in which 1) the transient temperature fields are determined first using MAGMAsoft (explained in this chapter) and 2) stresses and deformations are calculated next in ABAQUS (explained in Chapter 6). Because the mechanical properties of the constitutive model are temperature-dependent, accurate calculation of the temperature fields is a critical step in the determination of properties at all times and locations throughout the bar.

4.2 Thermophysical Properties and Parameters

To perform thermal simulations, MAGMAsoft requires several inputs, including thermophysical properties (density, thermal conductivity, specific heat), volume fraction of solid, and latent heat of solidification. Using the experimental casting chemistry, these temperature-dependent properties for the steel were calculated using IDS [45] software, a solidification analysis package for steels. Because the IDS calculations for all casting chemistries (shown in Table 3.1) produced similar properties, a single set of representative properties (from the Strained 6 experiment) are shown in this section.

Thermophysical properties of the steel are shown Figure 4.1. Rather than using a source term in the conservation equations to account for the liberation of heat during the solid-state phase transformation, the effects of the transformation are included in the effective specific heat curve and manifested as a large spike at approximately 700°C (shown in Figure 4.1(b)). This curve was determined from IDS as the differential change in enthalpy with respect to temperature ($\partial H/\partial T$). The volume fraction of solid during solidification (g_s), shown in Figure 4.2, contains an inflection point (at $g_s = 0.6$), which represents the solid-state phase change from delta-ferrite to austenite. Calculated latent

heat of solidification values ranged from 244 to 252 kJ/kg (249 kJ/kg for Strained 6).

The thermal boundary conditions between the mold and casting are specified in MAGMAsoft with the interfacial heat transfer coefficient (*IHTC*), which characterizes the heat transfer at the mold-metal interface. As the casting cools, thermal contractions of the steel create an insulating air gap at the mold-metal interface, reducing the heat transfer from the casting to the mold. The reduction in heat transfer is accomplished by a decrease of the *IHTC* as the air gap increases, i.e., the *IHTC* is inversely proportional to the size of the air gap. For the initial thermal simulation, the temperature-dependent “Steel-Sand” dataset from the MAGMAsoft database was used, shown in Figure 4.3.

Thermophysical properties of the mold, shown in Figure 4.4, were defined using the “Furan” dataset from the MAGMAsoft property database. Again, “spikes” are seen in the (effective) specific heat curve, shown in Figure 4.4(c), to account for the endothermic reactions to vaporize water (100°C) and binder (400°C) in the mold.

4.3 Thermal Simulations

Both the mold and casting were included in the simulations. Virtual thermocouples were placed in the MAGMAsoft model at the experimental thermocouple locations (shown in Figure 3.3). The simulations included filling the mold and solidification and cooling of the casting. In addition to the properties and parameters presented in the Section 4.2, a pouring temperature of 1600°C was specified for the initial thermal simulation. The procedure to match the simulated and measured temperatures in this section is described using the experimental thermocouple data from the Strained 6 casting trial.

Comparisons between the measured and simulated temperatures at the Sprue and Right locations are shown in Figure 4.5 and Figure 4.6, respectively. While the overall agreement between measured and simulated Sprue temperatures (Figure 4.5(a)) appears to be reasonable, the small time scale (Figure 4.5(c)) shows a large discrepancy between

the simulated (125 s) and measured (200 s) times to reach the solidus temperature; when the simulated temperature reaches T_{sol} (1360°C), the measured temperature is more than 100°C cooler. Because the turnbuckle forces in the casting trials induced stresses near the solidus temperature, matching the measured and simulated temperatures in this region is necessary. Thus, a series of adjustments were needed to achieve agreement.

Matching simulated and measured temperatures is a multi-step iterative process. In the first step, a reference time ($t = 0$ s) was set when the molten steel first contacts the Sprue thermocouple during pouring of the mold. At this time, the simulated thermocouple immediately increased to the temperature of the liquid steel. The experimental thermocouple, however, experienced a lag time, especially for high temperature gradients, and required several seconds to read the actual temperature, at which time the liquid melt had already cooled by several degrees. For this reason, the simulation should always predict a slightly higher maximum temperature than the experiment.

Next, the temperature curves were matched in the time interval from the maximum temperature until the onset of solidification at the liquidus temperature (T_{liq}). To account for convective heat transfer in the liquid steel, the thermal conductivity was enhanced by a factor of 2.5 above T_{liq} . The effect of this enhancement increased the heat transfer in the melt and cooled the molten steel more rapidly. However, this enhancement also decreased the maximum temperature in the simulation to a value lower than the experiment. Therefore, the pouring temperature was increased to 1625°C. The results after these adjustments are shown in Figure 4.7. While the slopes still did not perfectly match at this point, subsequent adjustments to other properties, such as the thermal conductivity in the mold, would also affect the simulated slope. Therefore, no further adjustments were made to achieve agreement of the measured and simulated slopes above T_{liq} at this time.

Once the curves reasonably agreed to the time of T_{liq} , measured and simulated

times were matched from T_{liq} to T_{sol} , which was accomplished through a combination of adjustments to the latent heat of solidification and thermal conductivity of the mold. While a reduction in the latent heat results in the generation of less heat during solidification, an increase the mold thermal conductivity removes more heat from the casting. As a result, either adjustment increases the cooling rate of the casting. Figure 4.8 and Figure 4.9 show the effect of reducing the latent heat from 249 to 180 kJ/kg at the Sprue and Right locations, respectively. After this reduction, the small time scale at the Sprue location (shown in Figure 4.8(c)) showed significant improvement, as the simulated time to solidus had decreased from 215 s to 170 s. However, further adjustments were still needed to match the measured time to solidus (130 s). Through an adjustment to the thermal conductivity of the sand (shown in Figure 4.10(d)), the measured and simulated temperatures were now in good agreement (shown in Figure 4.10 and Figure 4.11, respectively) from the reference time ($t = 0$ s) to the solid-state transformation (1200 s and 800 s at the Sprue and Right locations, respectively). In general, the simulated and measured temperatures could not be perfectly matched at both thermocouple locations. Initially, the simulated and measured temperatures were matched at the Sprue location. However, this created significant disagreement at the Right location, as the simulated temperatures were higher than the measurement. As a result, the average temperature throughout the bar was likely higher in the simulation than the experiment. Consequently, this would lead to an inaccurate prediction of the thermal strains during the stress analysis. Therefore, a compromise was made in which the simulated Sprue temperature cooled faster, whereas the Right temperature cooled slower than the measured temperatures. While this procedure would result in a better prediction of thermal strains, it also introduces uncertainties of the predicted temperature fields, especially at the highest temperatures.

In order to demonstrate the motivation behind making adjustments to the mold thermal conductivity, an in-depth explanation is given at this time. The “after

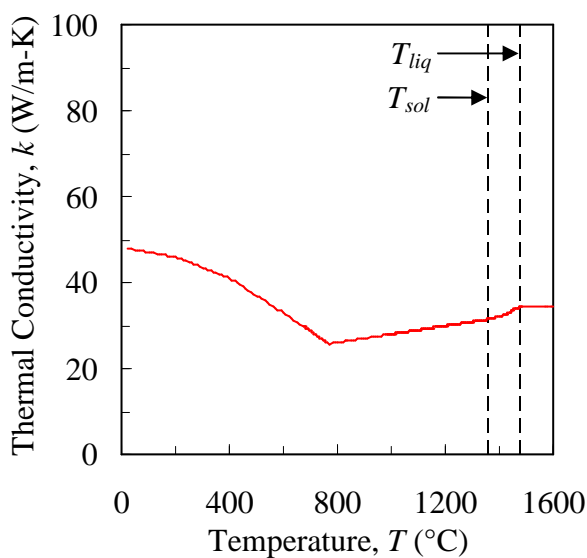
adjustment” curve, shown in Figure 4.10(d), decreases with increasing temperature from a maximum value of 1.4 W/m-K at room temperature to a minimum value of 1.1 W/m-K at 500°C, after which it slowly increases to 1.2 W/m-K at 1600°C. Because thermal conductivity is generally an increasing function of temperature, the decrease from room temperature to 500°C requires additional explanation. As molten metal increases the mold temperature, the mold binder evaporates and creates gases. The binder gases flow outward through the porous mold, and the heat transfer is enhanced by convection. For this reason, the thermal conductivity of the mold from room temperature to 500°C should be viewed as an “effective” thermal conductivity, i.e., the effects of convective heat transfer are included. Once the binder has evaporated, the thermal conductivity decreases to a minimum, as subsequent heat transfer is due primarily to conduction. As a result, the thermal conductivity slowly increases with temperature from 500°C to 1600°C.

Although the times to the liquidus and solidus temperatures were previously matched, the temperatures between these times, i.e., the temperatures throughout the solidification interval, do not necessarily agree. While the “after adjustment” curve of the previous simulation shows excellent agreement throughout the solidification range at the Sprue location (shown in Figure 4.10(c)), this is generally not the case. To match temperature curves during solidification, the released latent heat must be redistributed throughout the solidification interval. This is accomplished through an adjustment to the volume of solid fraction curve. By adjusting the curve as shown in Figure 4.12(d) and Figure 4.13(d), excellent agreement was now achieved throughout the solidification range of the Right thermocouple location, shown in Figure 4.13(c). Although the agreement at the Sprue location was worse after the adjustment, good agreement in the solidification range was generally achieved throughout all other experiments, as will be shown later.

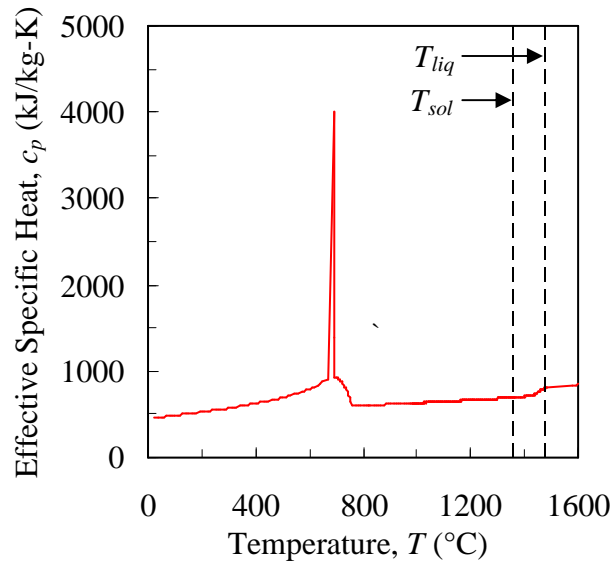
At this point, good agreement was accomplished from the reference time to the solid-state transformation. Final agreement from the solid-state transformation to room temperature was achieved by an adjustment to the *IHTC*. Recall that heat transfer

through the mold was enhanced due to the convective flow of binder gases. Obviously, this enhancement is appropriate only during the heat-up of the mold, as binder gases are no longer present during cool-down, i.e., the mold contains a hysteresis effect. Therefore, while the increased mold thermal conductivity at lower temperatures helped to achieve agreement from the reference time to T_{sol} , it caused the simulated temperatures to cool too quickly at temperatures less than 500°C. Hence, the *IHTC* is also an effective parameter that must be lowered an additional amount below 500°C to account for the hysteresis effects in the mold. By adjusting the *IHTC* as shown in Figure 4.14(c) and Figure 4.15(c), excellent overall agreement was achieved throughout the casting process.

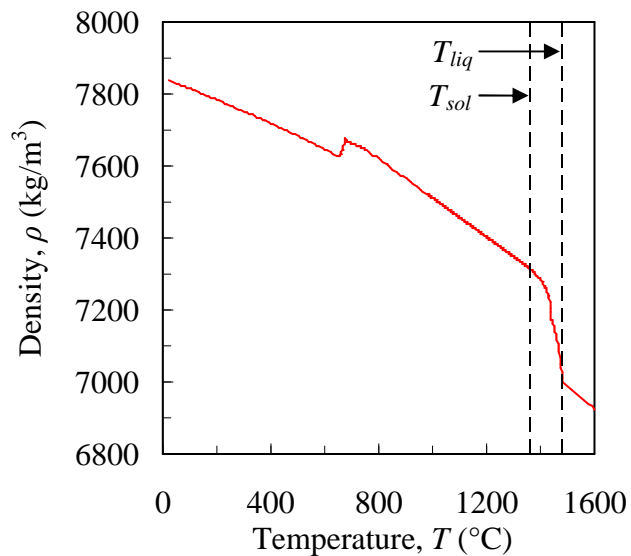
Using a single set of adjusted properties, good agreement between measured and simulated temperature was achieved for all remaining bar experiments. However, because the conditions of each experiment were slightly different (pouring temperatures, casting chemistry, inhomogeneous molds), adjustments to the latent heat, mold thermal conductivity and pouring temperature were required to achieve the best-possible agreement for each experiment. Because accuracy of the temperatures was of primary importance, these changes were deemed necessary. However, these adjustments were minor, and the final set of adjusted properties presented in this section should be considered representative of all experiments. The results for all Unrestrained and Strained experiments at the Sprue and Right (if available) locations are shown in Figure 4.16 through Figure 4.24. To create a smooth transient temperature profile at all bar locations, the temperature fields were printed out and exported to ABAQUS at a sufficient number (approximately 125) of time steps.



(a) Thermal Conductivity



(b) Effective Specific Heat



(c) Density

Figure 4.1. Thermophysical properties of steel. IDS used the experimental casting chemistry to calculate the thermophysical properties in the steel in IDS. Discontinuities in the curves at approximately 700°C are due to the solid-state transformation from austenite to ferrite and pearlite.

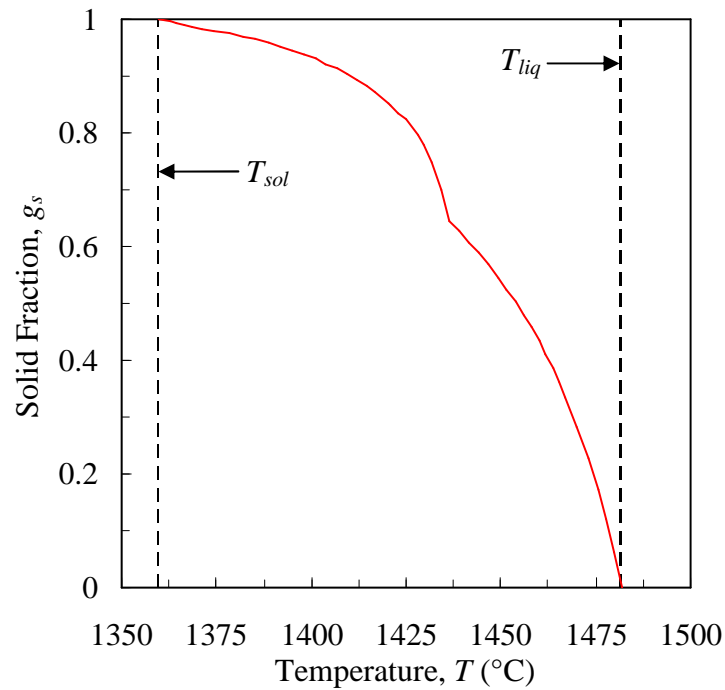


Figure 4.2. Solid fraction volume as a function of temperature. IDS used the experimental casting chemistry to calculate the volume of solid fraction as a function of temperature. The inflection point at $g_s=0.63$ is the result of the solid-state transformation from delta-ferrite to austenite.

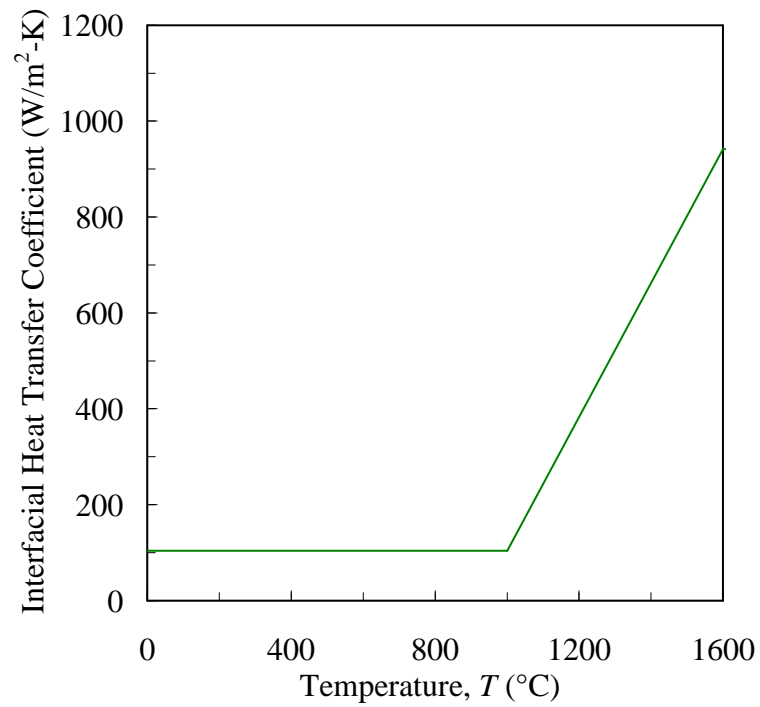
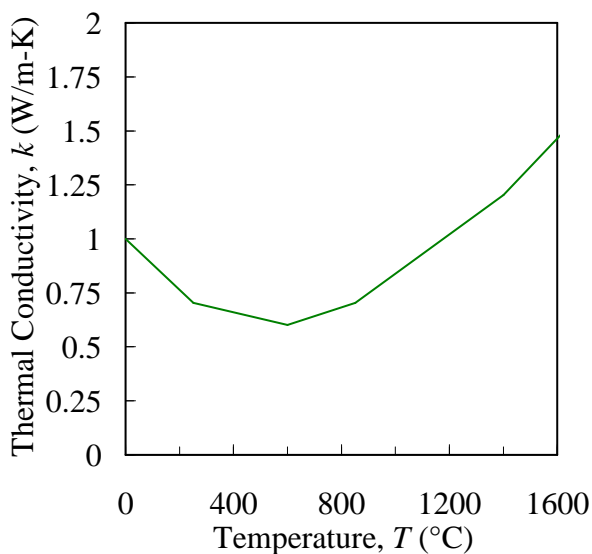
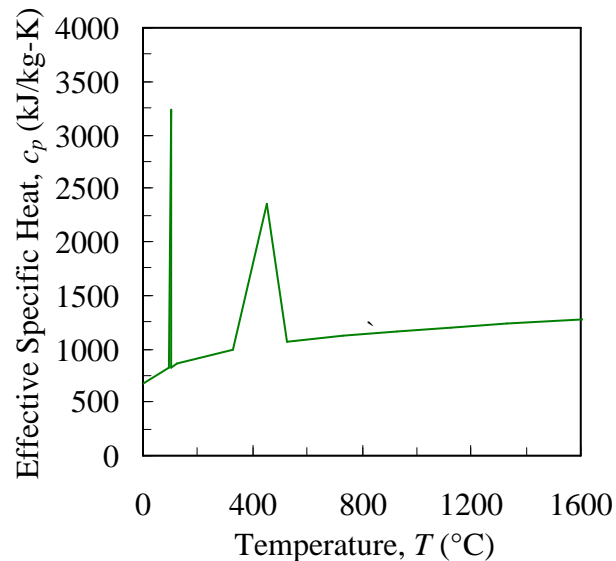


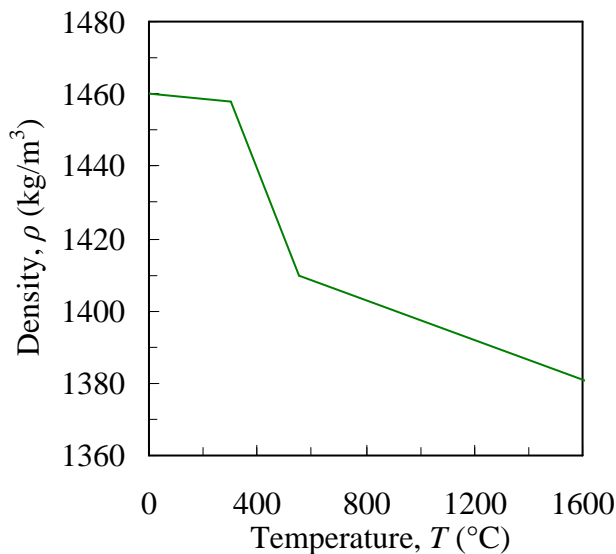
Figure 4.3. Interfacial heat transfer coefficient (*IHTC*). The interfacial heat transfer coefficient characterizes the heat transfer at the mold-metal interface. As the casting cools, an air gap forms at the interface and acts to decrease the heat transfer rate. The *IHTC* is taken from the “Steel-Sand” dataset in the MAGMAsoft database.



(a) Thermal Conductivity

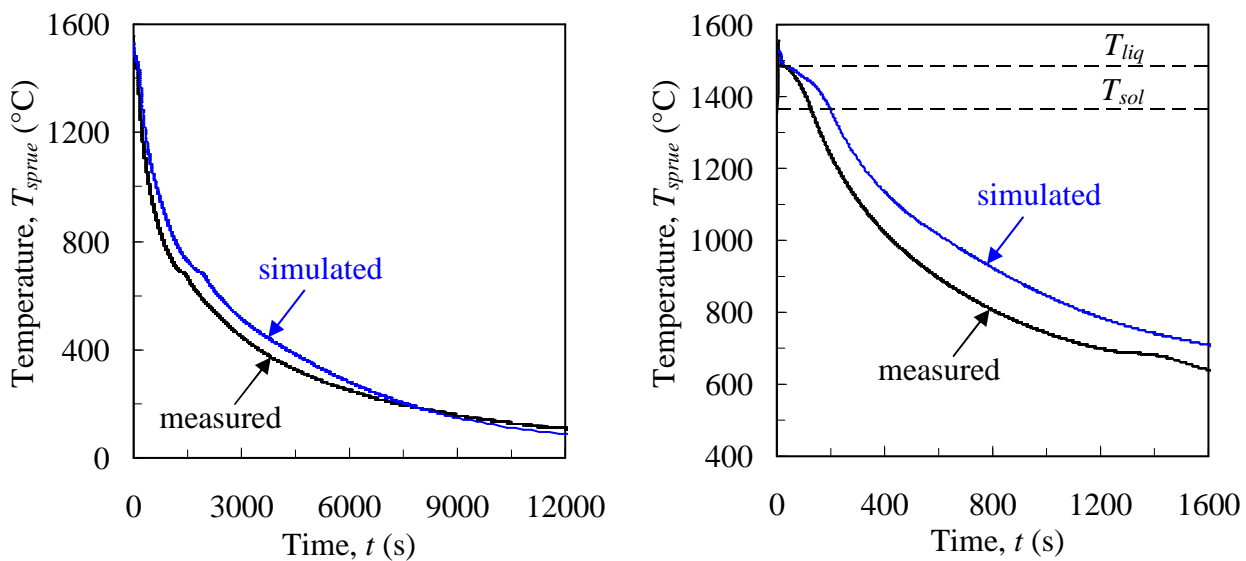


(b) Effective Specific Heat



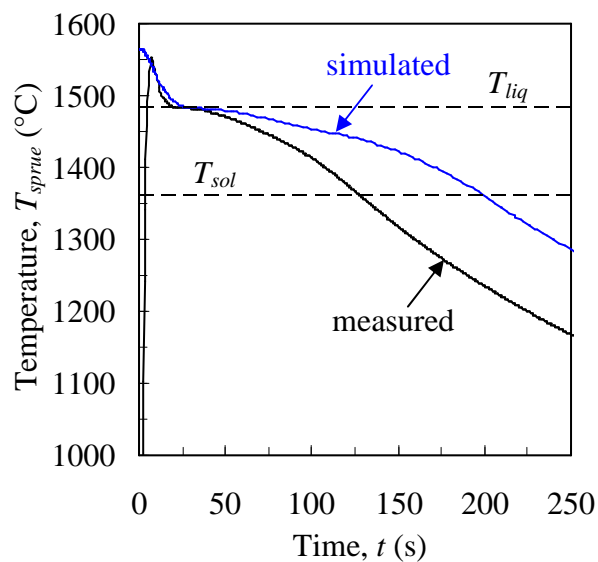
(c) Density

Figure 4.4. Thermophysical properties of the mold. The thermophysical properties are taken from the “Furan” dataset located in the MAGMAsoft database. The “spikes” in the effective specific heat curve at 100°C and 400°C account for endothermic reactions needed to evaporate the water and phenolic urethane binder, respectively.



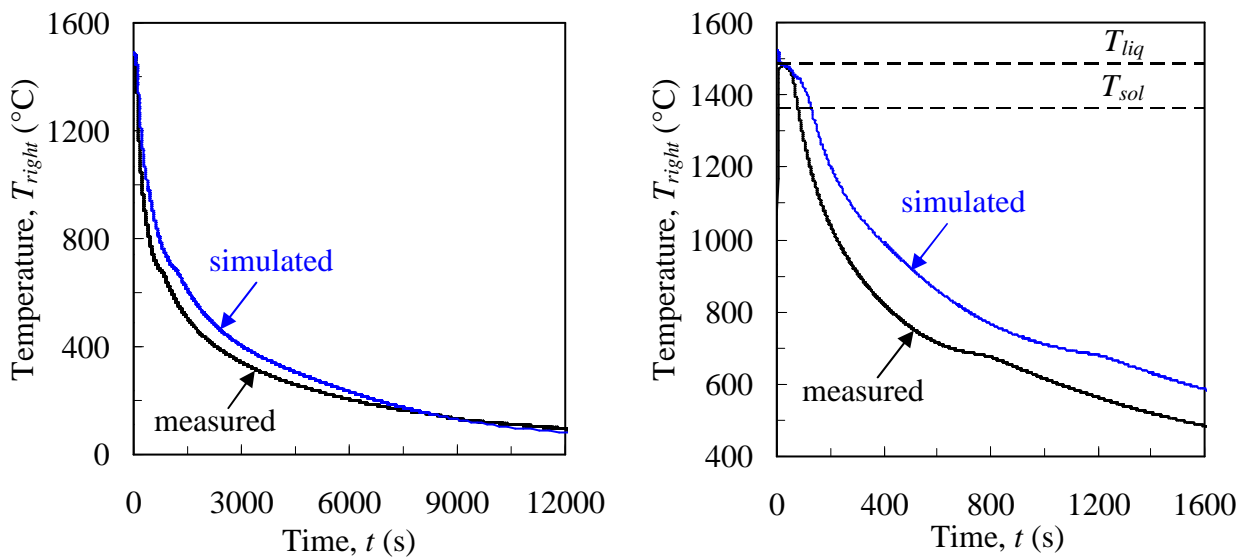
(a) Large time scale

(b) Medium time scale



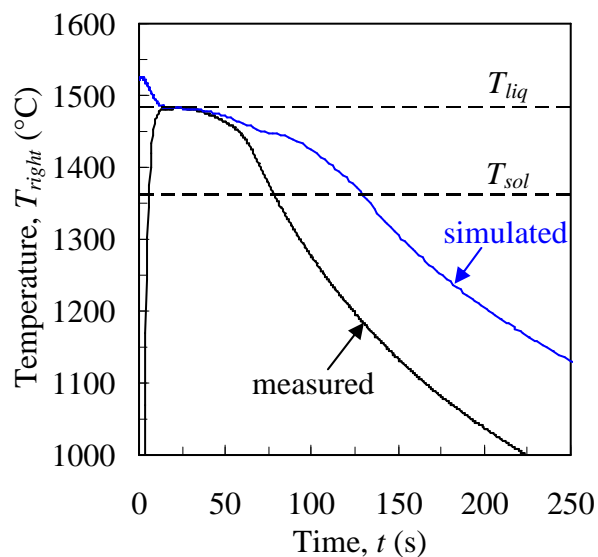
(c) Small time scale

Figure 4.5. Initial thermal simulation at the Sprue location. While reasonable agreement between simulated and measured temperatures is seen on the large scale, the small-scale comparison reveals a large difference in the time to solidus of approximately 100 s.



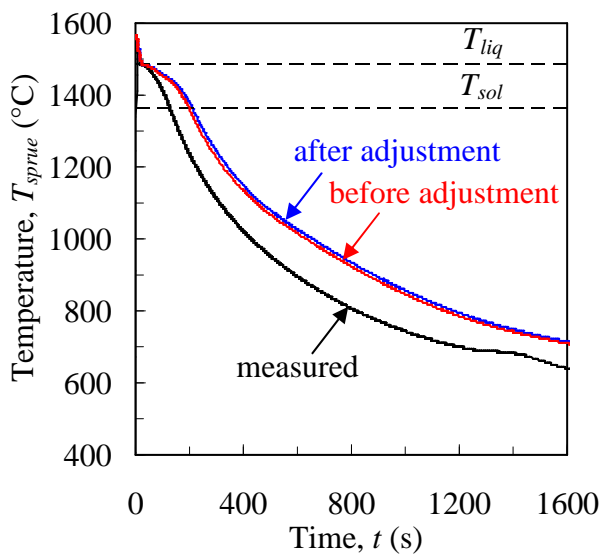
(a) Large time scale

(b) Medium time scale

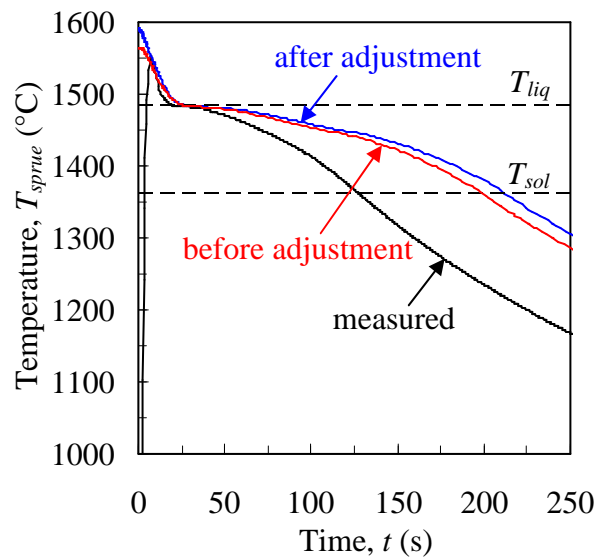


(c) Small time scale

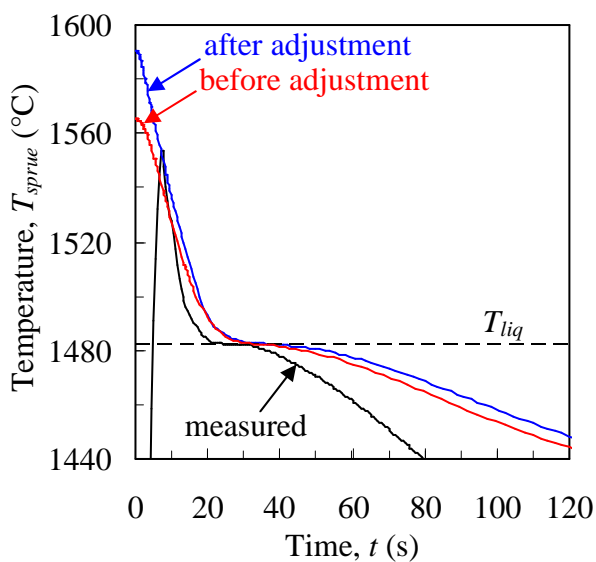
Figure 4.6. Initial thermal simulation at the Right location. While reasonable agreement between simulated and measured temperatures is seen on the large scale, the small-scale comparison reveals a large difference in the time to solidus of approximately 75 s.



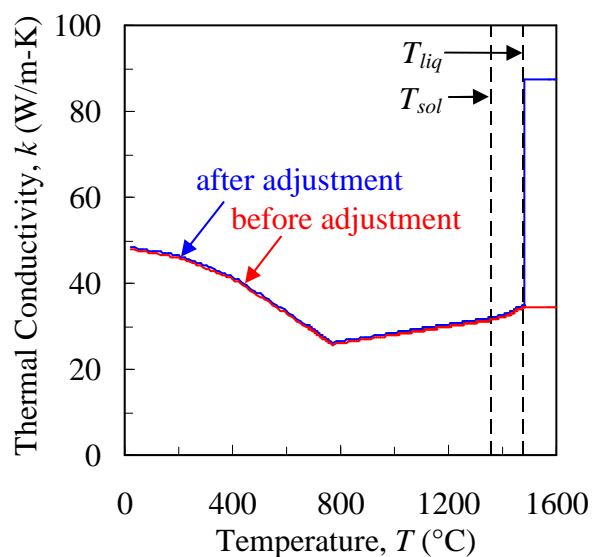
(a) Medium time scale



(b) Small time scale

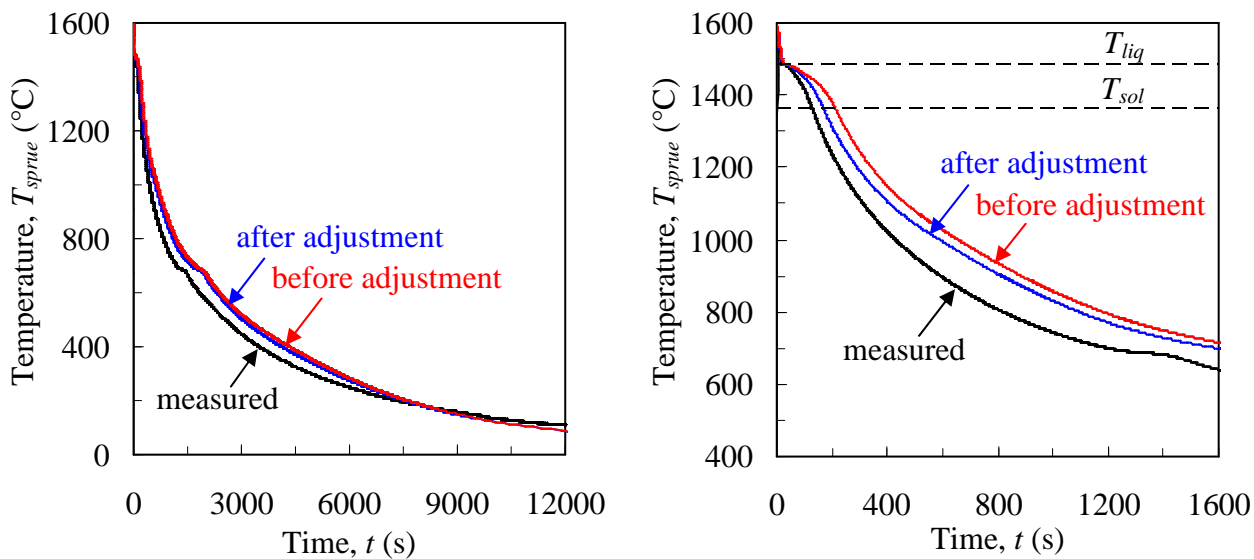


(c) Very small time scale



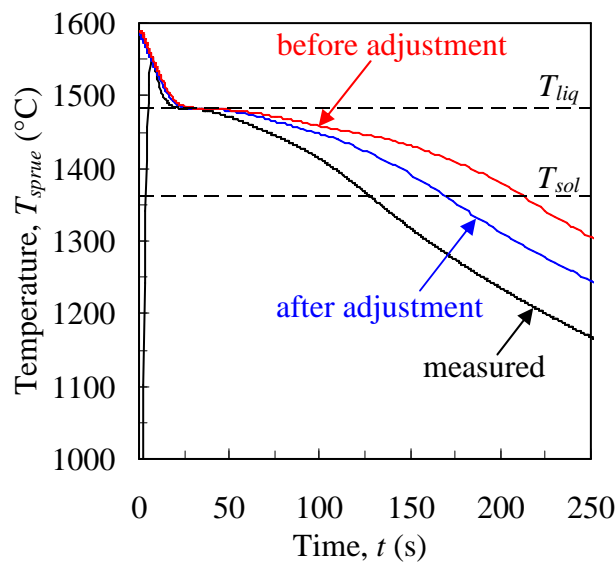
(d) Steel thermal conductivity

Figure 4.7. Thermal simulation after enhancing the thermal conductivity and adjusting the pouring temperature. The adjustments have a small impact on the simulation below the liquidus temperature.



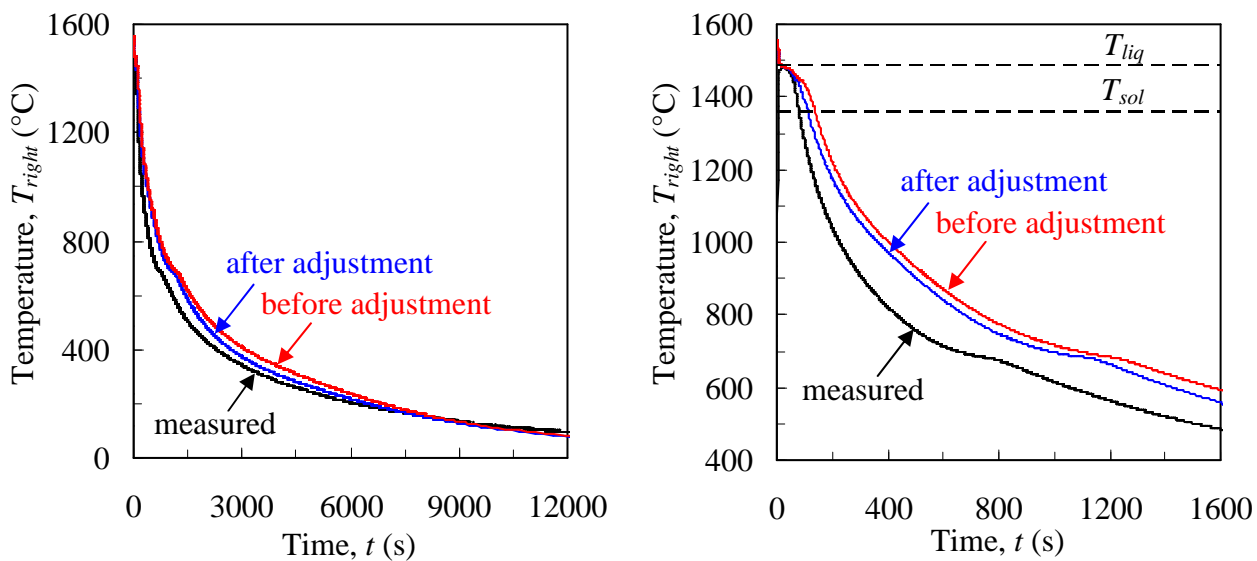
(a) Large time scale

(b) Medium time scale



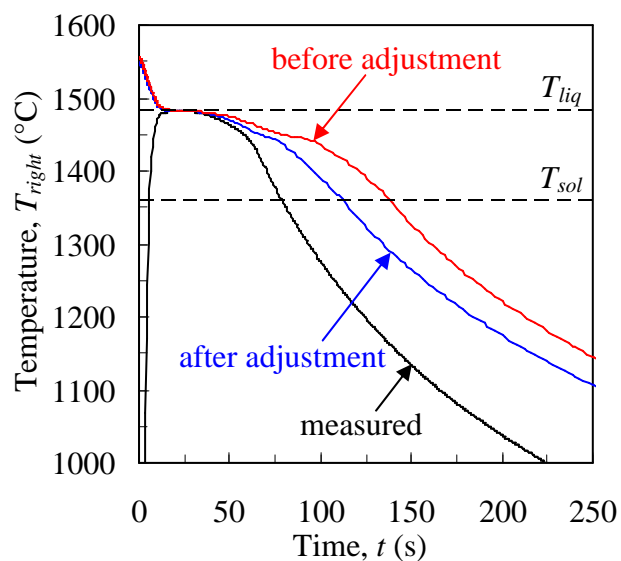
(c) Small time scale

Figure 4.8. Thermal simulation at the Sprue location after adjusting the latent heat of solidification from 249 to 180 kJ/kg. The difference in times to the solidus temperature is reduced from 100 s to 50 s after the adjustment.



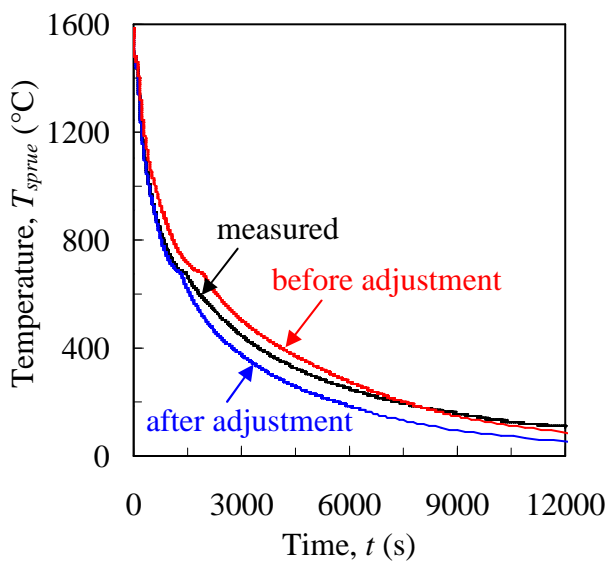
(a) Large time scale

(b) Medium time scale

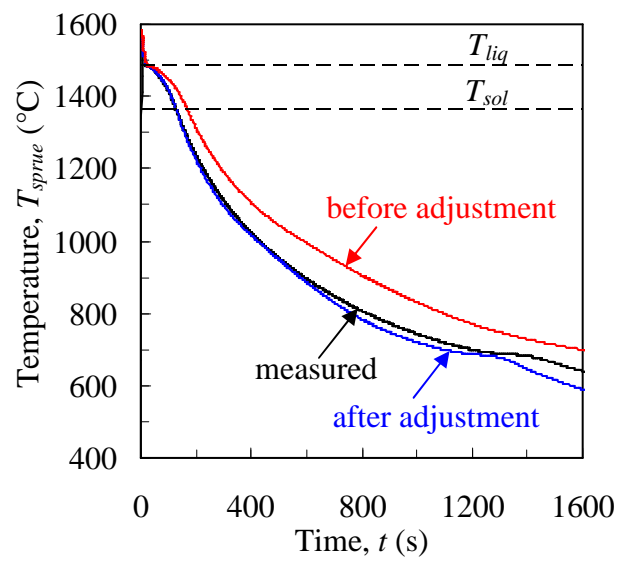


(c) Small time scale

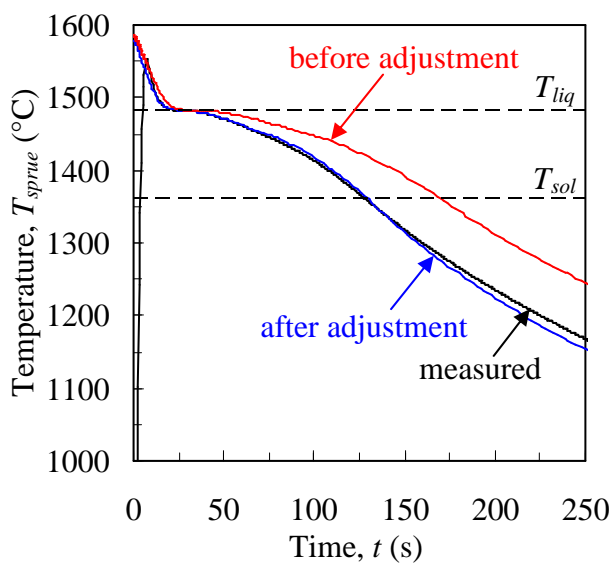
Figure 4.9. Thermal simulation at the Right location after adjusting the latent heat of solidification from 249 to 180 kJ/kg. The difference in times to the solidus temperature is reduced from 75 s to 40 s after the adjustment.



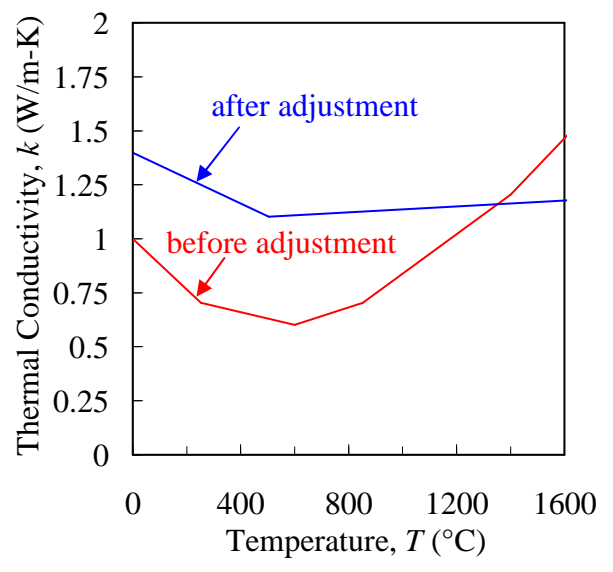
(a) Large time scale



(b) Medium time scale

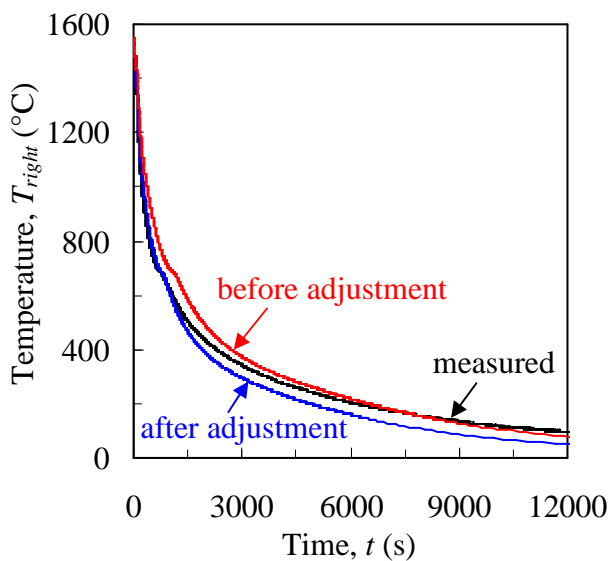


(c) Small time scale

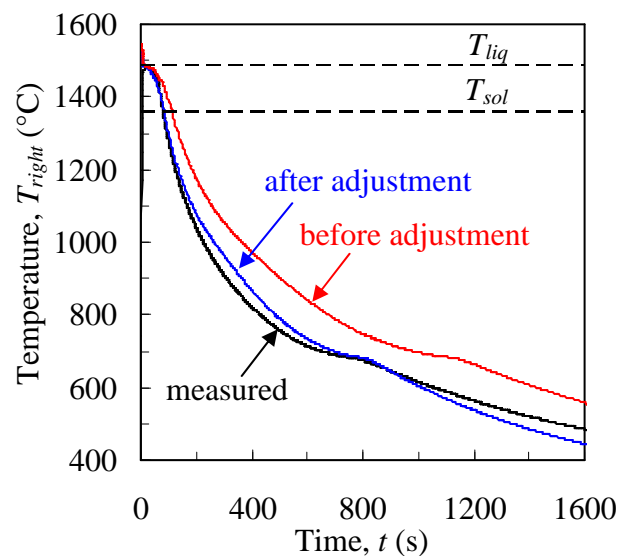


(d) Sand thermal conductivity

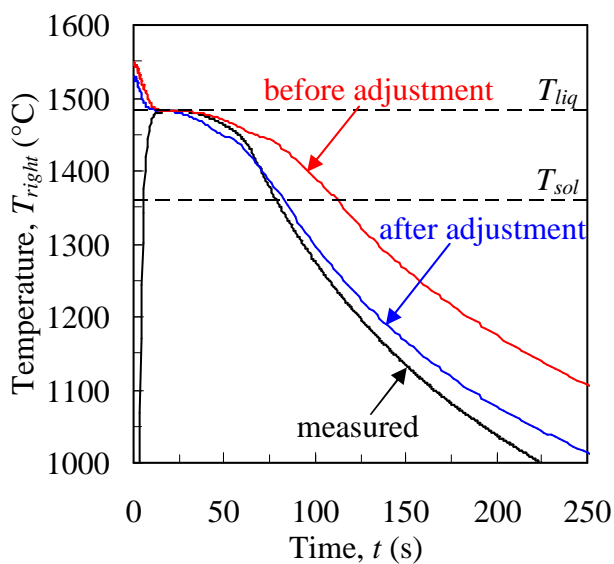
Figure 4.10. Thermal simulation at the Sprue location after adjusting the thermal conductivity of the mold. The adjustment to the thermal conductivity in the mold results in good agreement in times to solidus.



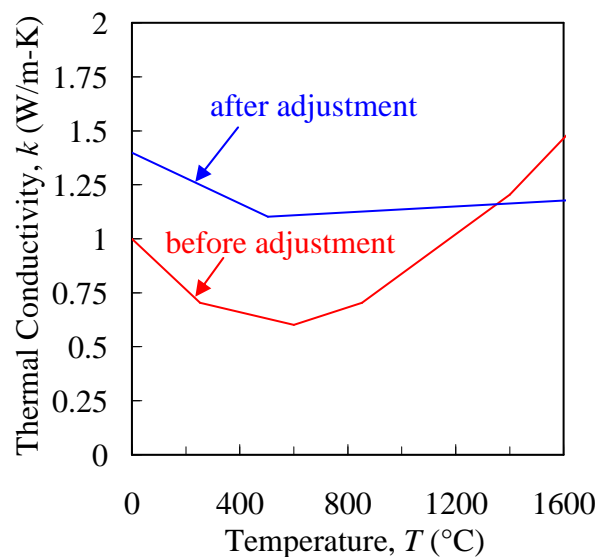
(a) Large time scale



(b) Medium time scale

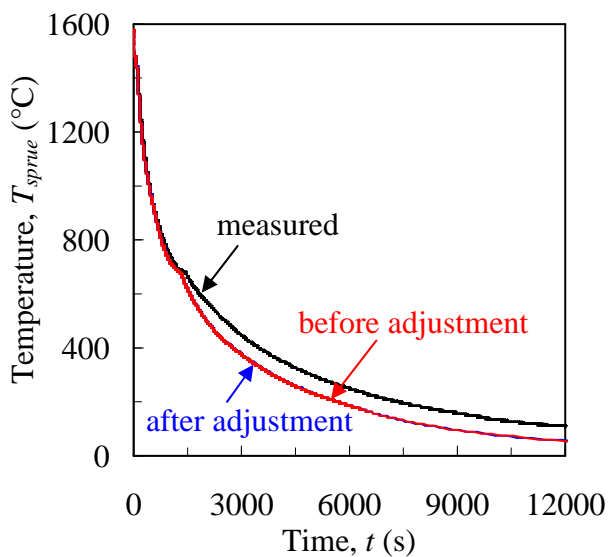


(c) Small time scale

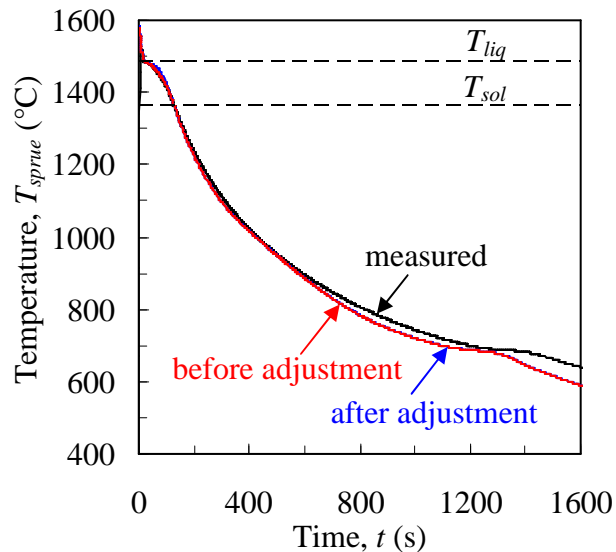


(d) Sand thermal conductivity

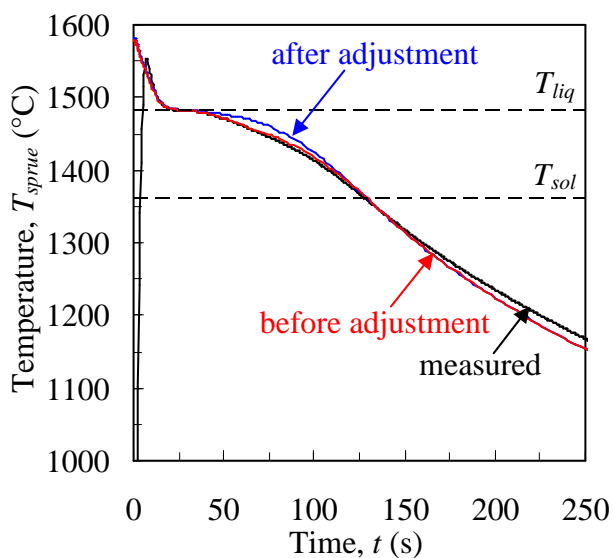
Figure 4.11. Thermal simulation at the Right location after adjusting the thermal conductivity of the mold. The adjustment to the thermal conductivity in the mold results in good agreement in times to solidus.



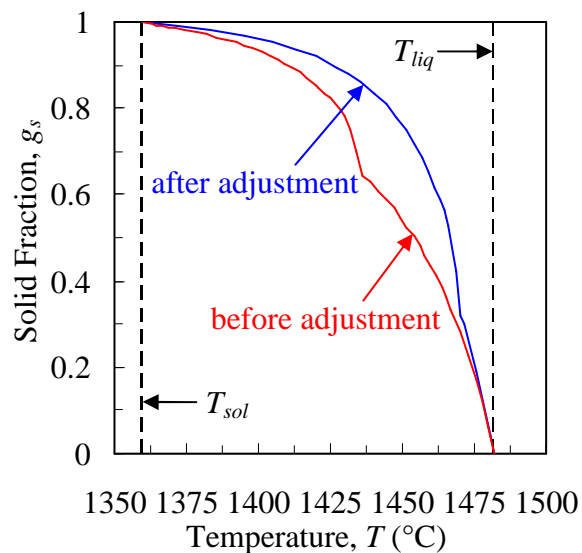
(a) Large time scale



(b) Medium time scale

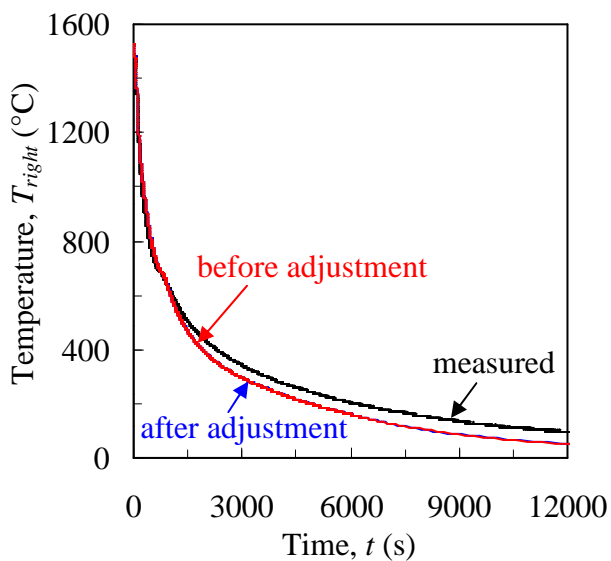


(c) Small time scale

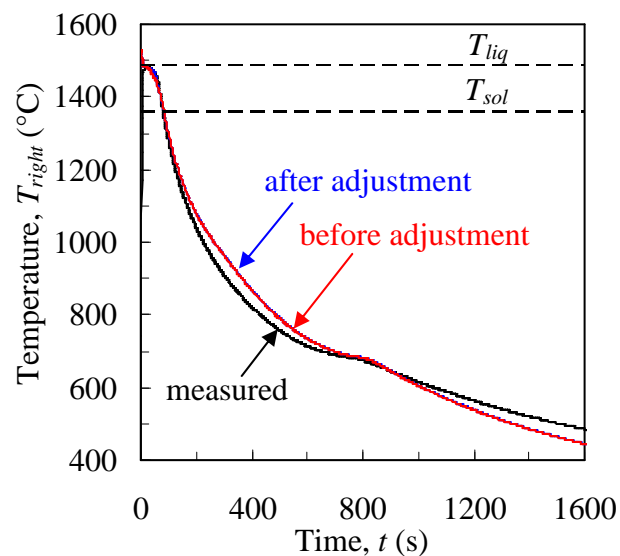


(d) Solid Fraction

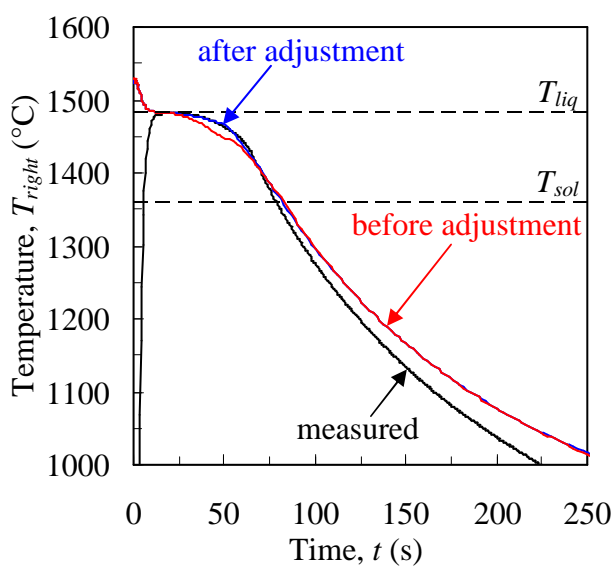
Figure 4.12. Thermal simulation at the Sprue location after adjusting the solid fraction. Although the agreement is worse after the adjustment for this instance, it will generally improve the agreement in the other thermal simulations.



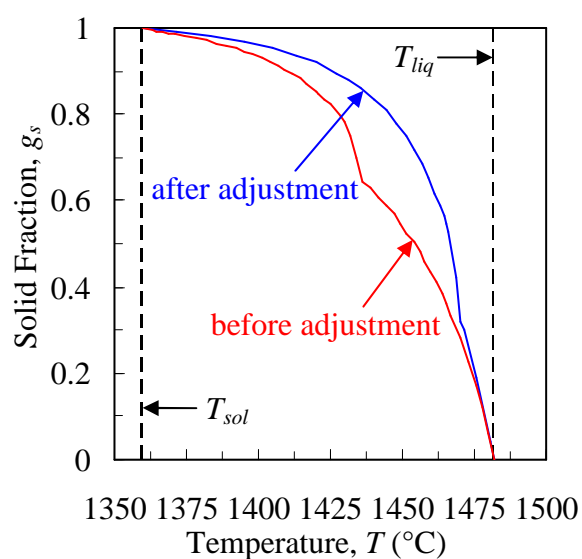
(a) Large time scale



(b) Medium time scale



(c) Small time scale



(d) Solid Fraction

Figure 4.13. Thermal simulation at the Right location after adjusting the solid fraction. The measured and simulated temperatures agree throughout the solidification range after the adjustment.

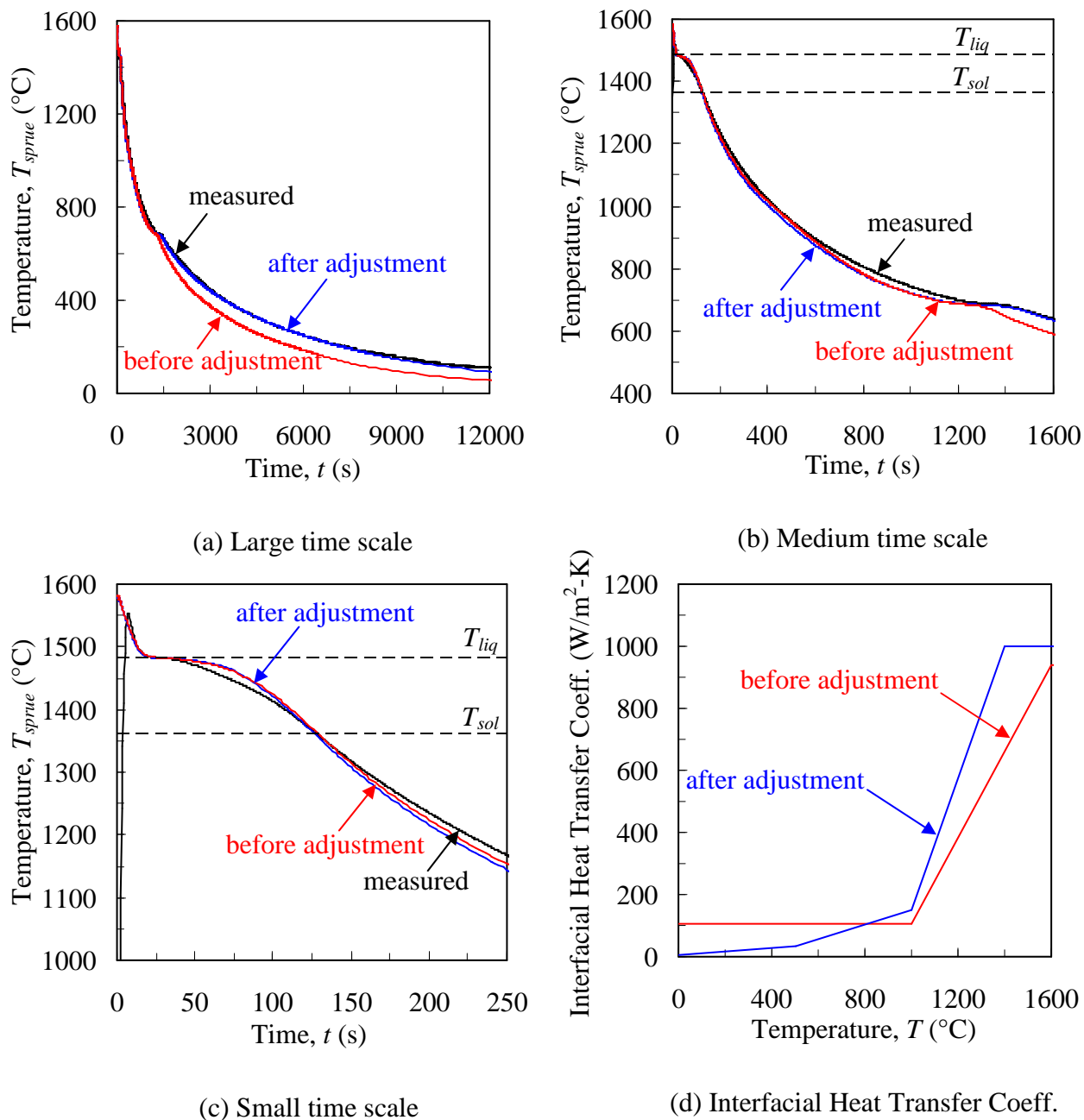
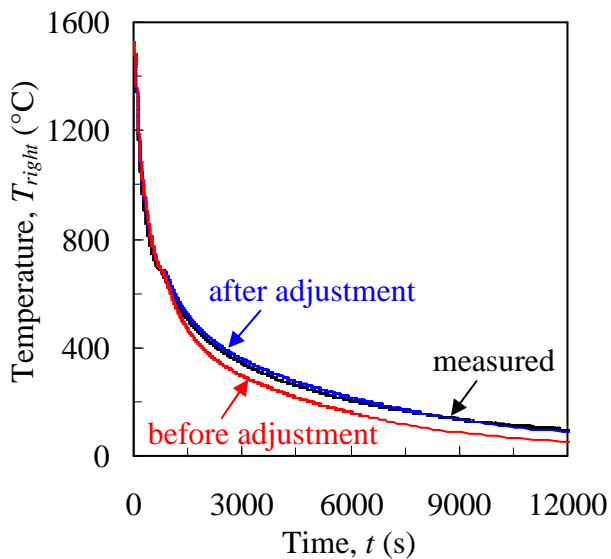
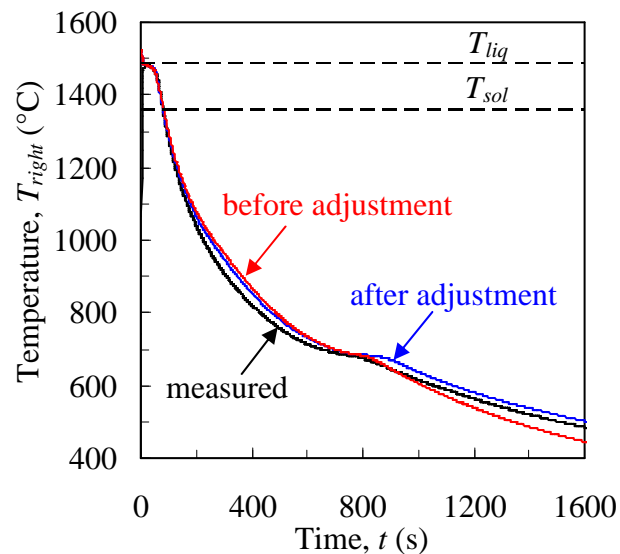


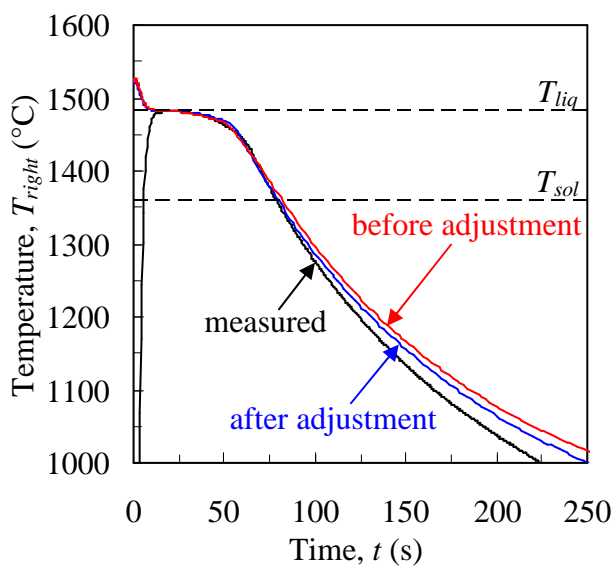
Figure 4.14. Thermal simulation at the Sprue location after adjusting the $IHTC$. This adjustment results in good agreement after the solid-state transformation.



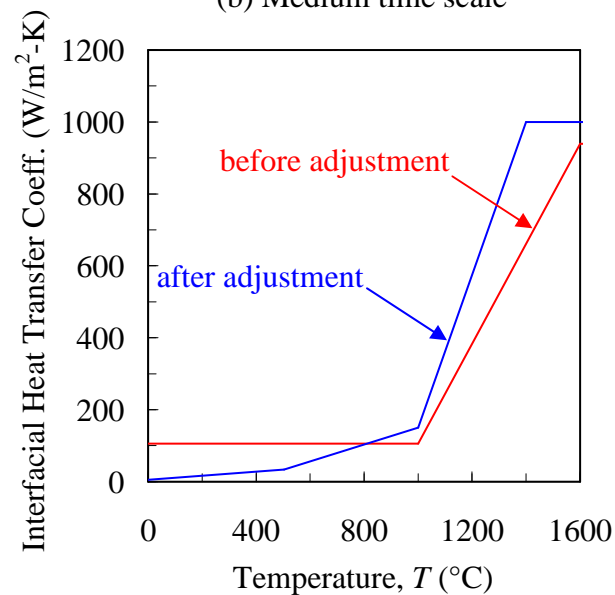
(a) Large time scale



(b) Medium time scale

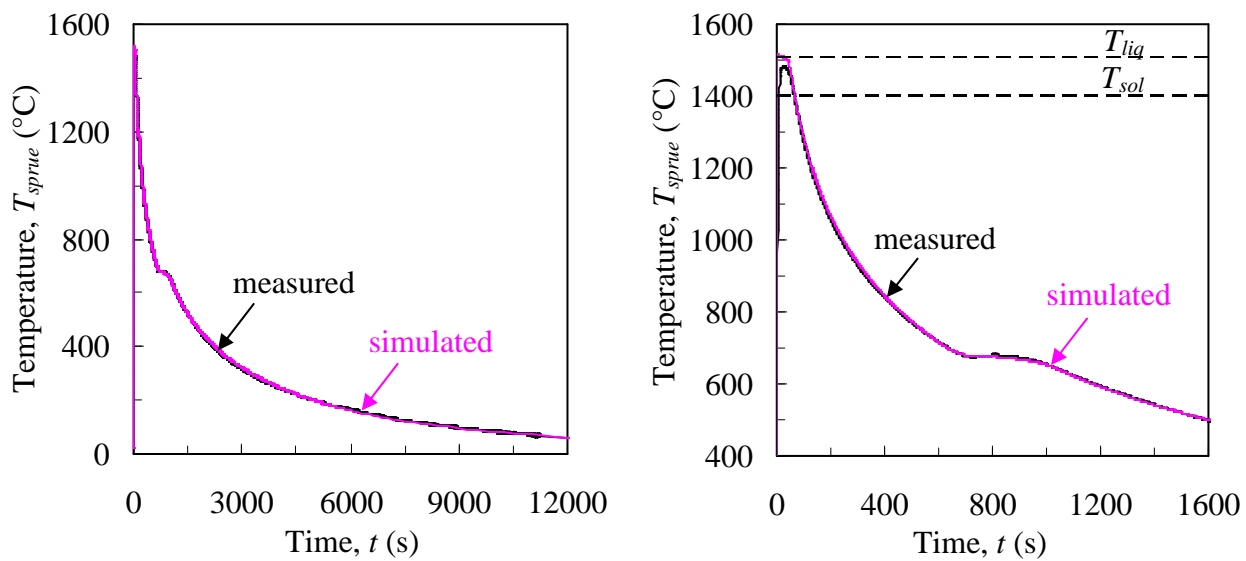


(c) Small time scale



(d) Interfacial Heat Transfer Coeff.

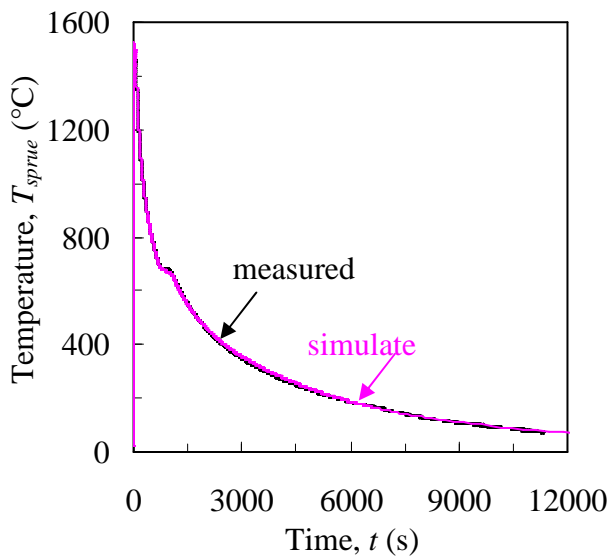
Figure 4.15. Thermal simulation at the Right location after adjusting the $IHTC$. This adjustment results in good agreement after the solid-state transformation.



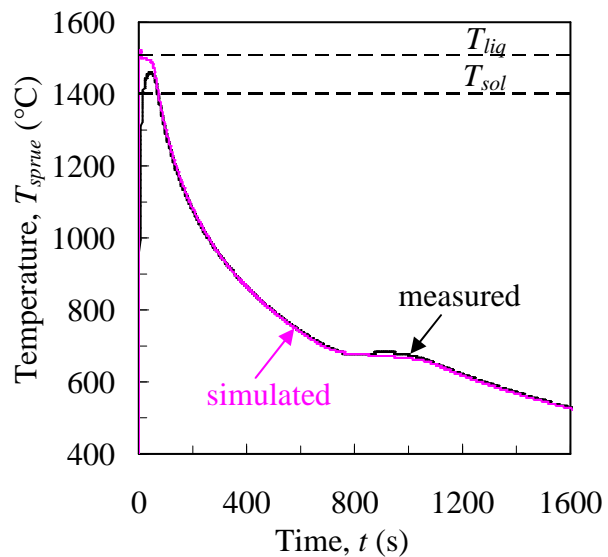
(a) Large Time Scale – Sprue Location

(b) Medium Time Scale – Sprue Location

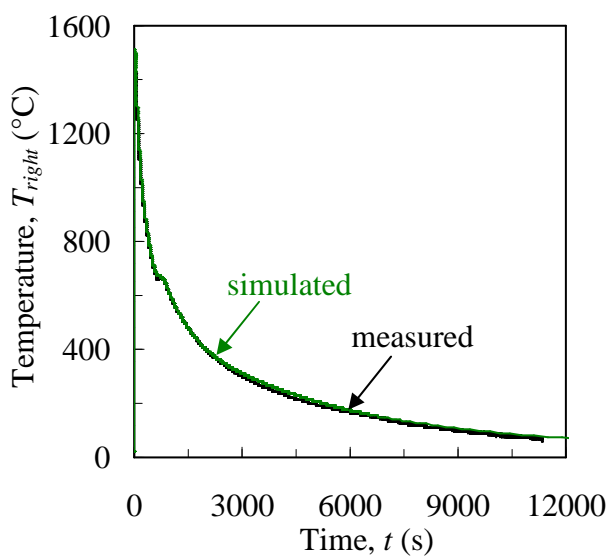
Figure 4.16. Unrestrained 1 final thermal simulation at the Sprue location. The experimental thermocouple failed at the Right location.



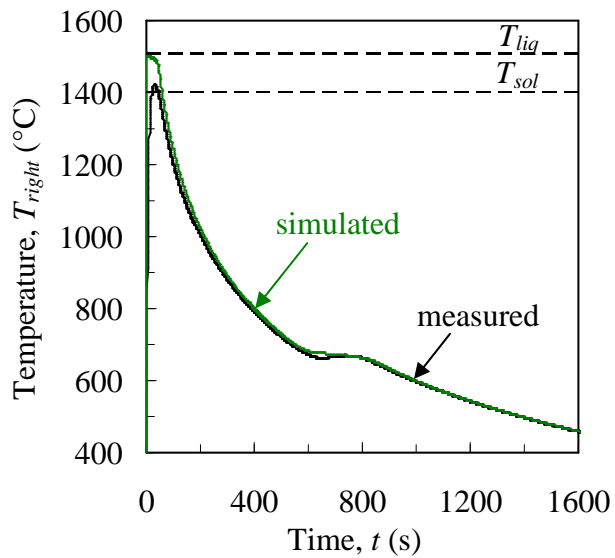
(a) Large Time Scale – Sprue Location



(b) Medium Time Scale – Sprue Location

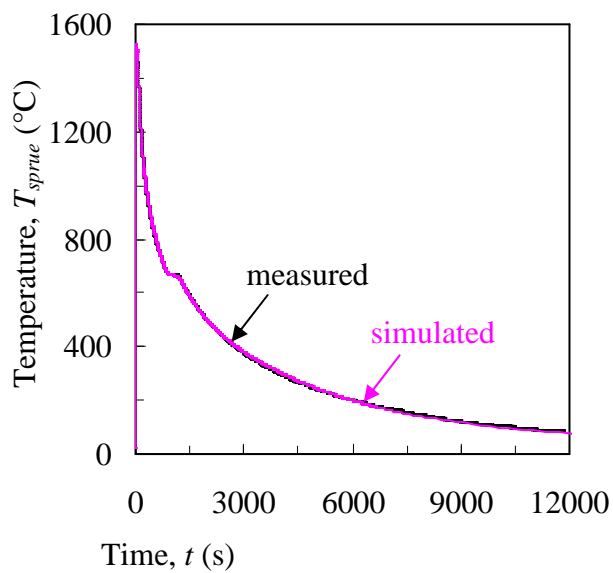


(c) Large Time Scale – Right Location

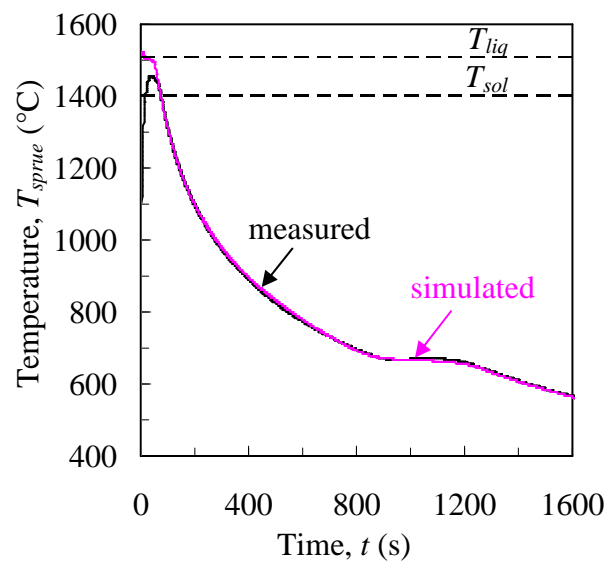


(d) Medium Time Scale – Right Location

Figure 4.17. Unrestrained 2 final thermal simulation at the Sprue and Right locations.

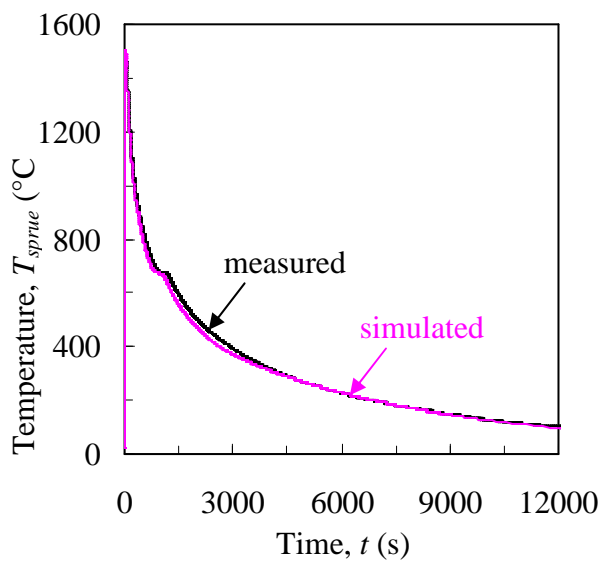


(a) Large Time Scale – Sprue Location

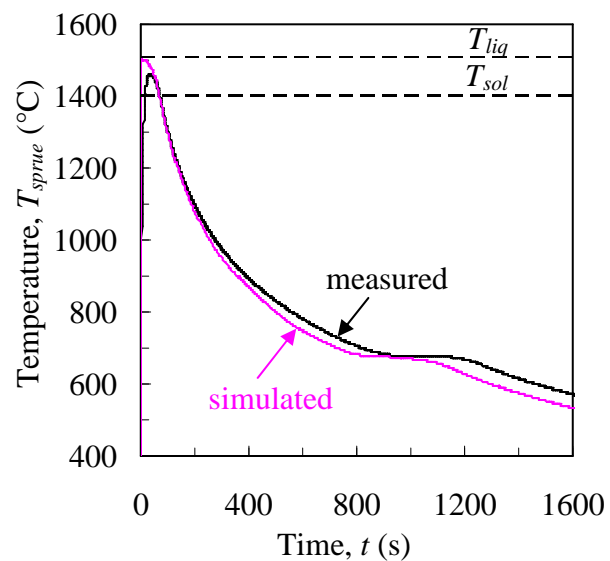


(b) Medium Time Scale – Sprue Location

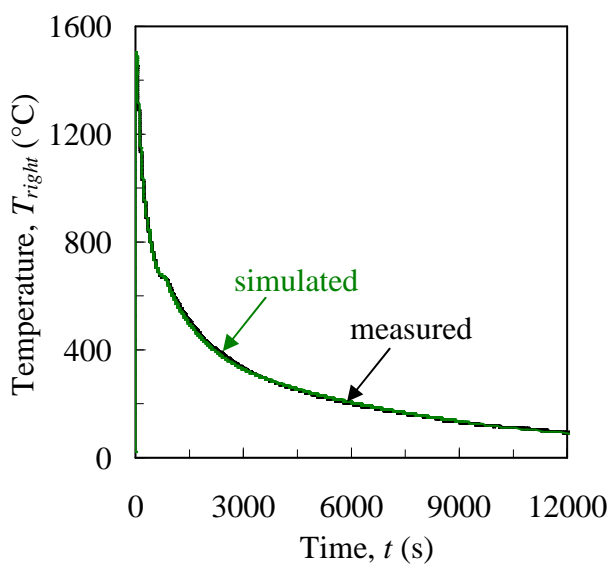
Figure 4.18. Unrestrained 3 final thermal simulation at the Sprue location. The thermocouple failed at the Right location.



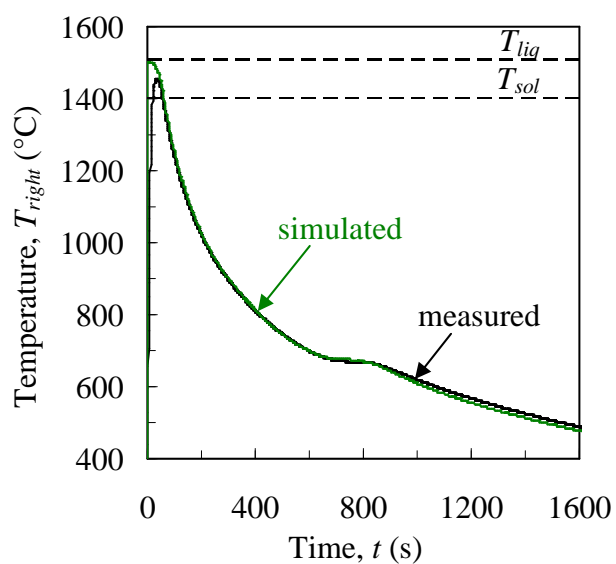
(a) Large Time Scale – Sprue Location



(b) Medium Time Scale – Sprue Location

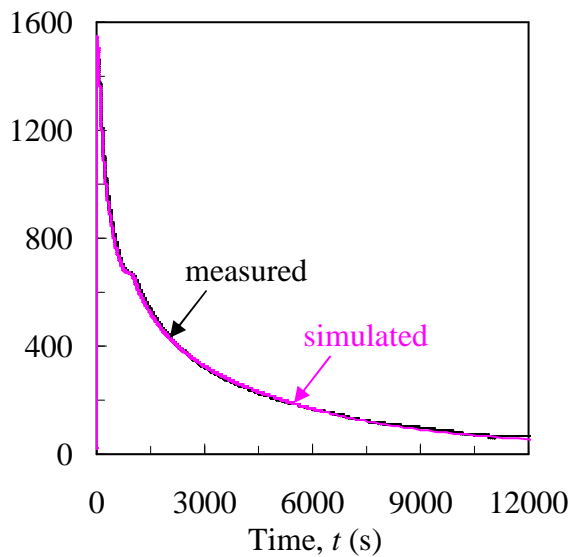


(c) Large Time Scale – Right Location

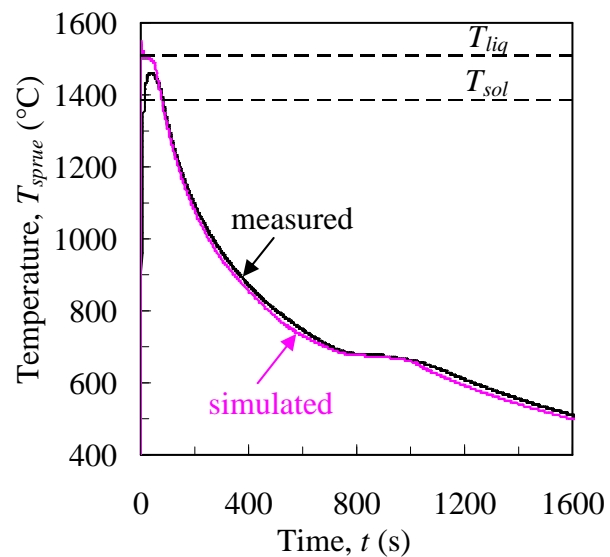


(d) Medium Time Scale – Right Location

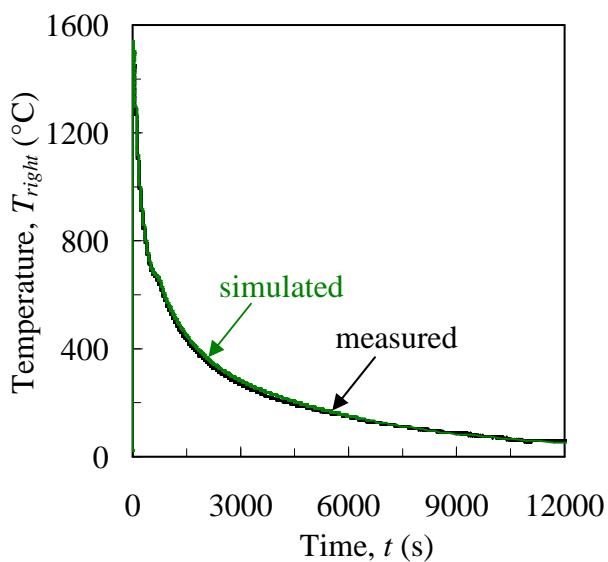
Figure 4.19. Strained 1 final thermal simulation at the Sprue and Right locations.



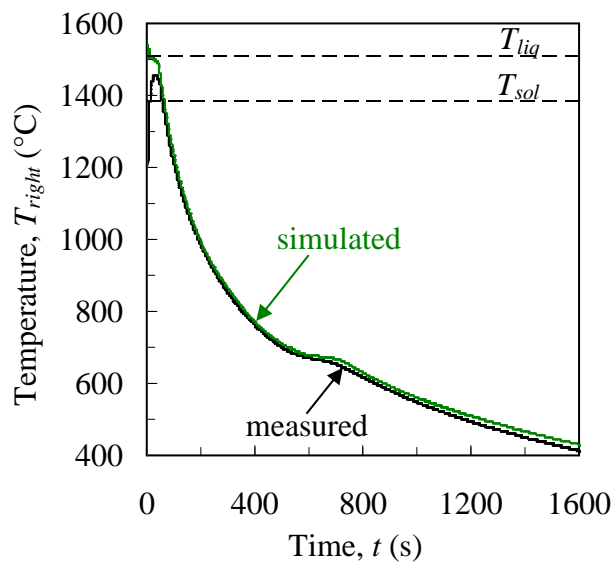
(a) Large Time Scale – Sprue Location



(b) Medium Time Scale – Sprue Location

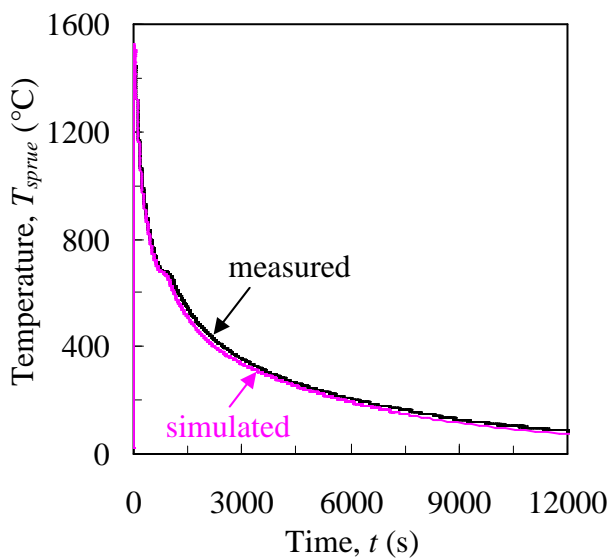


(c) Large Time Scale – Right Location

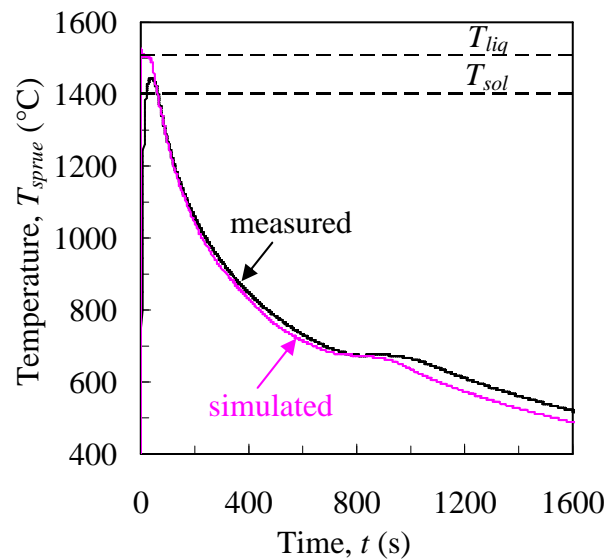


(d) Medium Time Scale – Right Location

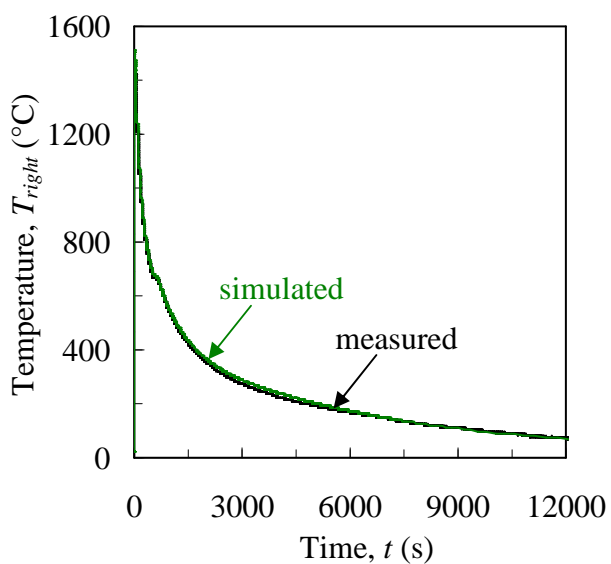
Figure 4.20. Strained 2 final thermal simulation at the Sprue and Right locations.



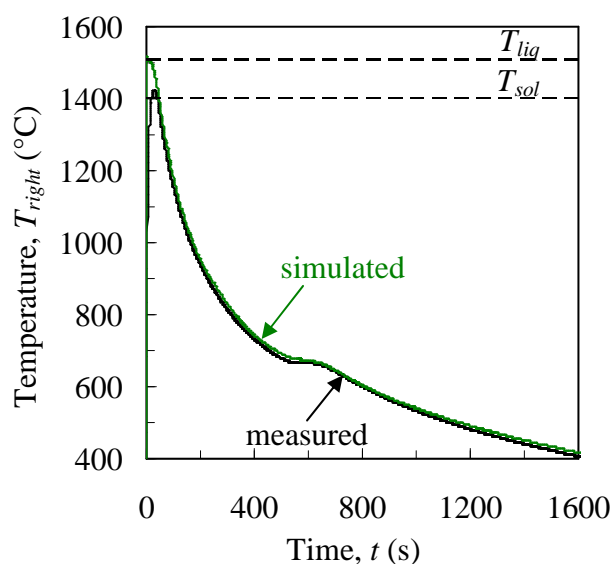
(a) Large Time Scale – Sprue Location



(b) Medium Time Scale – Sprue Location

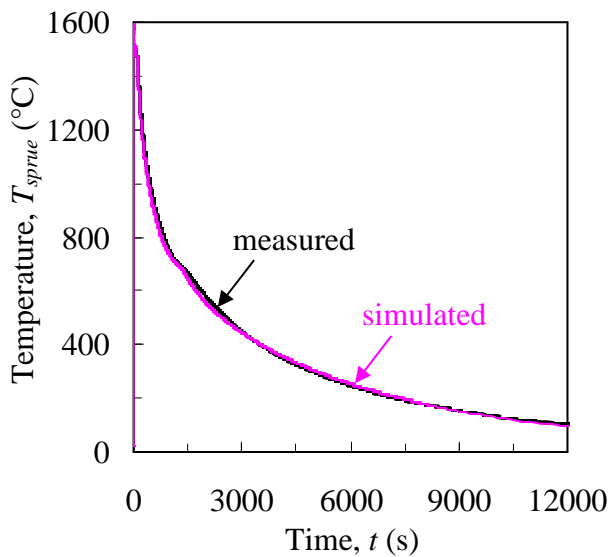


(c) Large Time Scale – Right Location

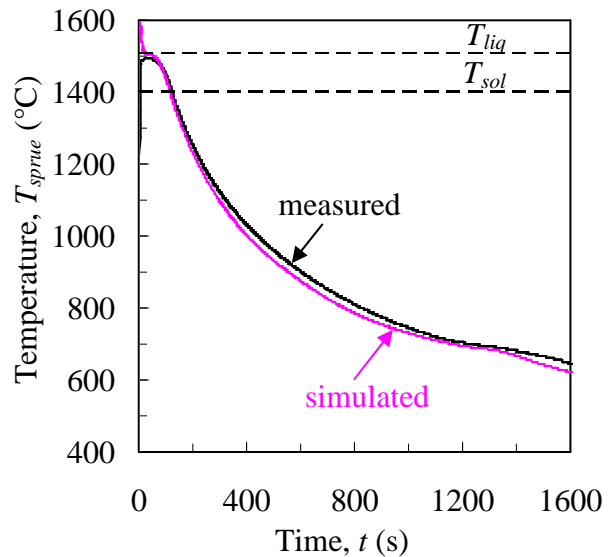


(d) Medium Time Scale – Right Location

Figure 4.21. Strained 3 final thermal simulation at the Sprue and Right locations.

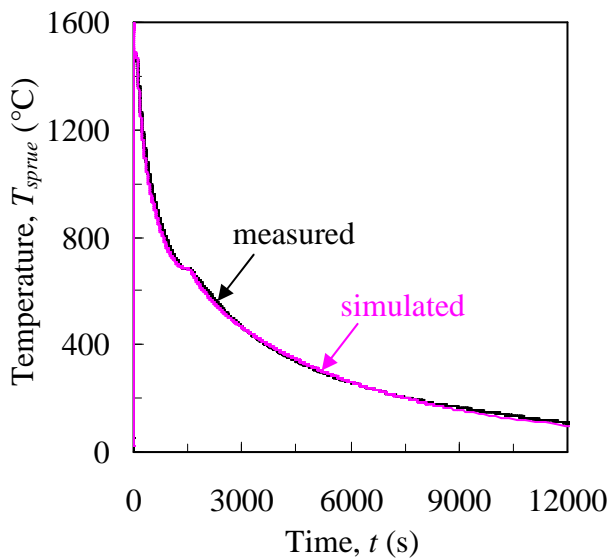


(a) Large Time Scale – Sprue Location

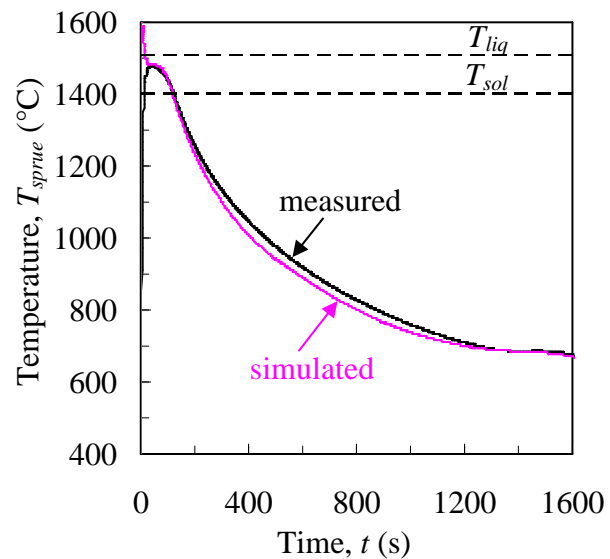


(b) Medium Time Scale – Sprue Location

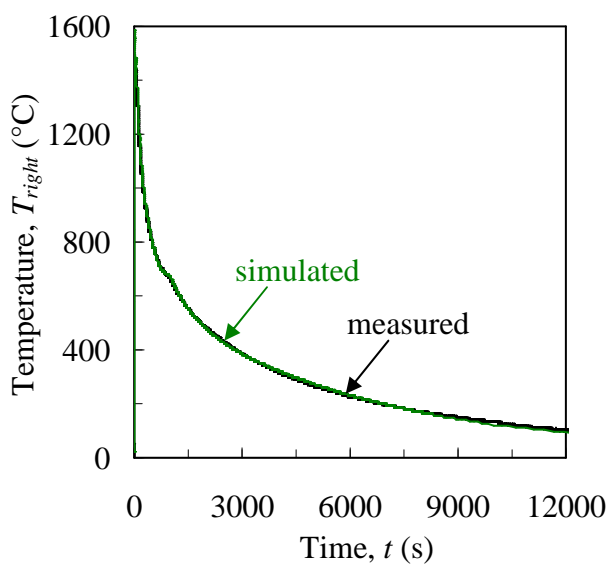
Figure 4.22. Strained 4 final thermal simulation. The experimental thermocouple failed at the Right location.



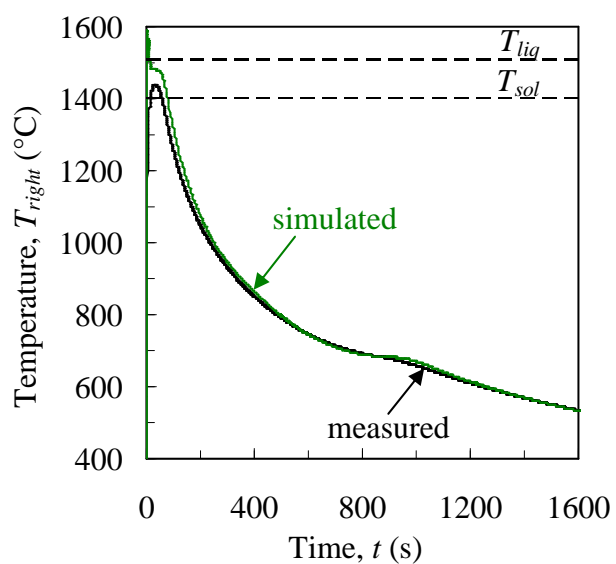
(a) Large Time Scale – Sprue Location



(b) Medium Time Scale – Sprue Location

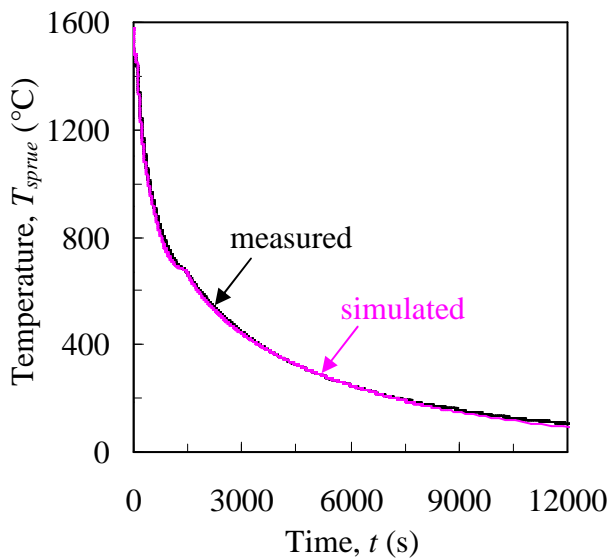


(c) Large Time Scale – Right Location

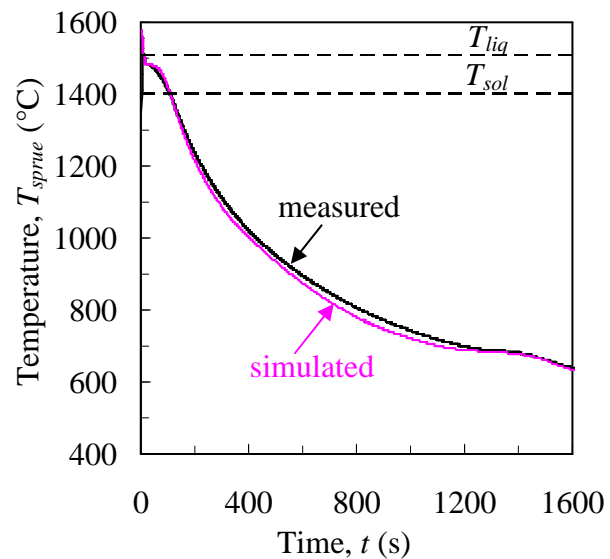


(d) Medium Time Scale – Right Location

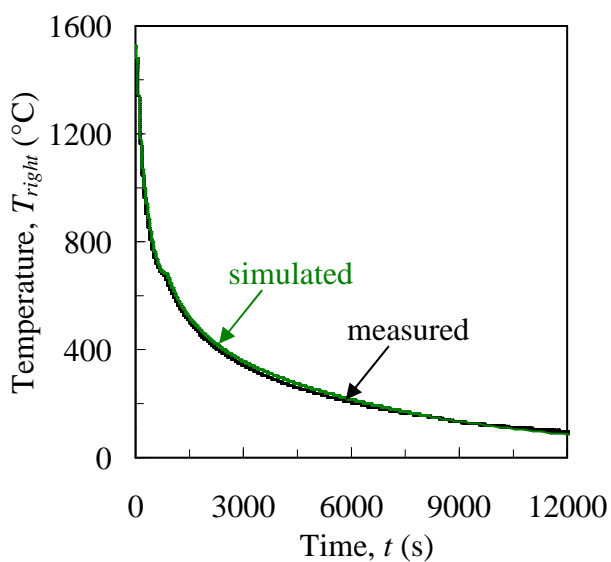
Figure 4.23. Strained 5 final thermal simulation at the Sprue and Right locations.



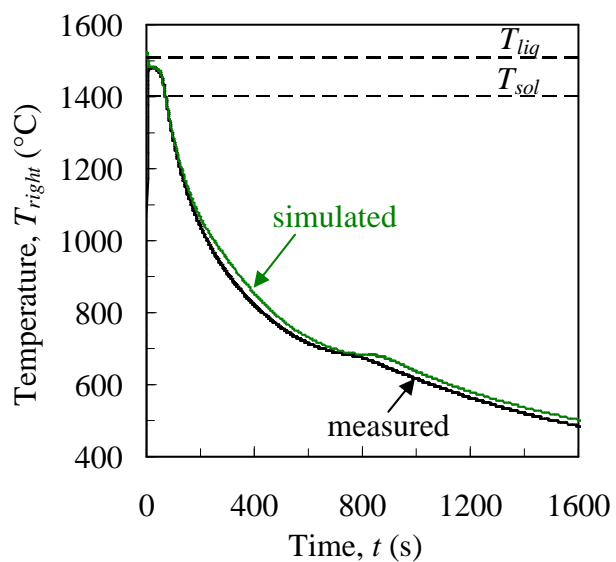
(a) Large Time Scale – Sprue Location



(b) Medium Time Scale – Sprue Location



(c) Large Time Scale – Right Location



(d) Medium Time Scale – Right Location

Figure 4.24. Strained 6 final thermal simulation at the Sprue and Right locations.

CHAPTER 5: MECHANICAL MODEL AND PROPERTIES

5.1 Introduction

The solid deformation model, which was implemented with a user-defined UMAT subroutine in ABAQUS by Monroe [46], calculates stresses, deformations, and damage (porosity created due to solid deformation) in the material during solidification and cooling. It includes both the rate-dependent and hardening effects. The model is reviewed here for completeness. Moving forward, the term “viscoplastic” will be used in place of “elasto-visco-plastic” for brevity.

5.2 Mechanical Model

The solid momentum equation is taken from [47] and given as

$$\nabla \cdot \tilde{\sigma}_s + g_s \rho_s \mathbf{g} = -\frac{g_l^2 \mu_l}{K} (\mathbf{v}_l - \mathbf{v}_s) + g_s \nabla p_l \quad (5.1)$$

where ρ_s is the solid density, \mathbf{g} is the gravitational vector, μ_l is the liquid viscosity, K is the permeability constant, \mathbf{v}_l and \mathbf{v}_s are the liquid and solid velocities, respectively, p_l is the liquid pressure, and g_s and g_l are the volume fractions of solid and liquid, respectively, which must sum to unity in the absence of porosity. The first term on the right side of Equation 5.1 is derived from Darcy’s law and included to account for the interfacial momentum transfer as the liquid flows through the mushy zone [48]. The effective stress tensor ($\tilde{\sigma}_s$) is derived from porous media theory [49] and given as

$$\tilde{\sigma}_s = g_s \sigma_s + g_l p_l \mathbf{I} \quad (5.2)$$

where σ_s is the stress in the solid and \mathbf{I} is the 2nd order identity tensor.

Several terms from Equation 5.1 may be neglected. The liquid pressure drop in the mushy zone (on the order of tens of kPa) is negligible when compared to stresses in the mushy zone (on the order of several MPa). Similarly, the stresses generated by the

body forces and interfacial momentum transfer are orders of magnitude less than effective stress tensor. As a result, Equation 5.1 reduces to

$$\nabla \cdot \tilde{\boldsymbol{\sigma}}_s = 0 \quad (5.3)$$

Because the total strains in a casting are no more than a few percent, the small strain assumption is valid. The total strain tensor, $\boldsymbol{\varepsilon}$, is decomposed into elastic, $\boldsymbol{\varepsilon}_e$, thermal, $\boldsymbol{\varepsilon}_{th}$, and viscoplastic, $\boldsymbol{\varepsilon}_{vp}$, components as

$$\boldsymbol{\varepsilon} = \boldsymbol{\varepsilon}_e + \boldsymbol{\varepsilon}_{th} + \boldsymbol{\varepsilon}_{vp} \quad (5.4)$$

Using Hooke's law, the elastic strain is determined by

$$\boldsymbol{\sigma} = \mathbf{C}_e : \boldsymbol{\varepsilon}_e \quad (5.5)$$

where \mathbf{C}_e is the elastic stiffness tensor. Assuming a homogeneous and isotropic material, \mathbf{C}_e is defined as

$$\mathbf{C}_e = \frac{E}{3(1-2\nu)} \mathbf{I} \otimes \mathbf{I} + \frac{E}{(1+\nu)} \mathbf{I}_{dev} \quad (5.6)$$

where E is Young's modulus, ν is Poisson's ratio, \mathbf{I} is the fourth-order identity tensor, and \mathbf{I}_{dev} is the fourth-order deviatoric identity tensor and given as

$$\mathbf{I}_{dev} = \mathbf{I} - (\mathbf{I} \otimes \mathbf{I})/3 \quad (5.7)$$

The thermal strain is given by

$$\boldsymbol{\varepsilon}_{th} = \alpha_{tot} (T - T_{coh}) \mathbf{I} \quad (5.8)$$

where the coherency temperature, T_{coh} , is the temperature at which the solid material

reaches coherency and begins to thermally contract (usually taken as the solidus temperature), and α_{tot} is the total thermal expansion coefficient and defined as

$$\alpha_{tot} = \frac{1}{(T - T_{coh})} \int_{T_{coh}}^T -\frac{1}{3\rho_s} \frac{d\rho_s}{dT} dT \quad (5.9)$$

Alternatively, the differential thermal expansion coefficient could have been used. However, for its calculation of thermal strains, ABAQUS requires α_{tot} .

The viscoplastic strain rate is determined from the flow condition [50] and defined as

$$\dot{\boldsymbol{\varepsilon}}_{vp} = \dot{\gamma} \frac{\partial \sigma_{eq}}{\partial \tilde{\boldsymbol{\sigma}}_s} \quad (5.10)$$

where $\dot{\gamma}$ is the scalar flow parameter and σ_{eq} is the equivalent stress. To account for stresses in the pressure-dependent mushy zone, the equivalent stress, taken from [51], is defined as the following combination of von Mises stress (q_s) and solid pressure (p_s)

$$\sigma_{eq} = (A_1 q_s^2 + A_2 p_s^2)^{0.5} \quad (5.11)$$

where A_1 and A_2 are functions of the solid fraction and rate dependent properties. The present model uses a form of the constants, which were proposed by Cocks [52] and given as

$$A_1 = \left(1 + \frac{2}{3}(1 - g_s^*)\right) (g_s^*)^{-2/(1+1/m)} \quad (5.12)$$

and

$$A_2 = \frac{9}{4} \left(\frac{1 - g_s^*}{2 - g_s^*}\right) \left(\frac{2}{1 + 1/m}\right) (g_s^*)^{-2/(1+1/m)} \quad (5.13)$$

where $1/m$ is the strain rate exponent (described later in this section), and g_s^* is the scaled solid fraction and defined as

$$g_s^* = g_s^{coal} \left(\frac{g_s - g_s^{coh}}{g_s^{coal} - g_s^{coh}} \right) \quad (5.14)$$

where g_s^{coh} and g_s^{coal} are the coherency and coalescence solid fractions, respectively. The coherency solid fraction occurs when the casting has solidified to where it can transmit stresses. The coalescence solid fraction represents the solid fraction at which no continuous liquid films remain between the dendrite arms. For solid fraction values below the coherency value, the material behaves like a liquid and is modeled as an elastic material with a low Young's modulus. For completeness, the von Mises stress (q_s) and solid pressure (p_s) are defined as

$$q_s = \sqrt{\frac{3}{2}(\boldsymbol{\tau}_s : \boldsymbol{\tau}_s)} \quad (5.15)$$

and

$$p_s = -\frac{1}{3}(\tilde{\boldsymbol{\sigma}}_s : \mathbf{I}) \quad (5.16)$$

where $\boldsymbol{\tau}_s$ is the deviatoric stress tensor ($\boldsymbol{\tau}_s = \tilde{\boldsymbol{\sigma}}_s + p_s \mathbf{I}$).

The yield condition is defined as

$$f_Y = q_s^2 + A_2' p_s^2 - A_3' \sigma_{dy}^2 \leq 0 \quad (5.17)$$

where A_2' and A_3' are related to the constants in Equation 5.11 by $A_2' = A_2/A_1$ and $A_3' = 1/A_1$. By substituting A_2' , A_3' , and Equation 5.11 into Equation 5.17, it is evident that the magnitude of dynamic yield stress, σ_{dy} , cannot exceed the equivalent stress, σ_{eq} .

Hence, if the current stress state lies on the yield surface, i.e., $f_Y = 0$, any subsequent increase in σ_{eq} must be accompanied with an increase in σ_{dy} , defined as

$$\sigma_{dy} = \sigma_0 \left(1 + \frac{\varepsilon_{eq}}{\varepsilon_0} \right)^{1/n} \left(1 + \frac{\dot{\varepsilon}_{eq}}{\dot{\varepsilon}_0} \right)^{1/m} \quad (5.18)$$

The increase in σ_{dy} is accomplished by increasing the equivalent plastic strain, ε_{eq} . The viscoplastic parameters in Equation 5.18 include the initial yield stress (σ_0), hardening exponent ($1/n$), strain rate exponent ($1/m$), reference strain ($\varepsilon_0 = \sigma_0 n / E$, where E is Young's modulus), and reference strain rate ($\dot{\varepsilon}_0 = A \exp(-Q/RT)$, where A is a prefactor, Q is the activation energy, R is the universal gas constant, and T is the absolute temperature). The equivalent plastic strain rate, $\dot{\varepsilon}_{eq}$, is defined from the scalar dissipation of energy and given as

$$\dot{\varepsilon}_{eq} = \frac{\tilde{\sigma}_s : \dot{\varepsilon}_s^{vp}}{g_s \sigma_{dy}} \quad (5.19)$$

and integrated to calculate the equivalent plastic strain

$$\varepsilon_{eq} = \begin{cases} 0, & T > T_{anneal} \\ \int_T^{T_{anneal}} \frac{\tilde{\sigma}_s : \dot{\varepsilon}_s^{vp}}{g_s \sigma_{dy}} dt, & T < T_{anneal} \end{cases} \quad (5.20)$$

The porosity formed due to solid deformation is calculated from the viscoplastic strain, described by [53] as

$$g_{p,d} = \int_{t_{coh}}^t g_s (\dot{\varepsilon}_s^{vp} : \mathbf{I}) dt \quad (5.21)$$

where t_{coh} is the time at which the coherency solid fraction is reached. Any local damage, i.e., $g_{p,d}$, that is calculated from Equation 5.21, is subtracted from the local solid fraction, g_s . This degraded solid fraction is subsequently used to calculate the scaled solid fraction, which couples the damage with the deformation in the model.

5.3 Mechanical Properties

The linear and total thermal expansion coefficients of steel were calculated from the density of the Strained 6 experiment and shown in Figure 5.1. At the solidus temperature, T_{sol} , the linear expansion value is approximately 0.025 mm/mm (2.25% contraction), which corresponds to the free shrink of steel.

Elastic mechanical properties were taken directly from the literature. The temperature-dependent Young's modulus of the steel, from Li and Thomas [32], is shown in Figure 5.2. In addition, because experimental observations of increased Poisson's ratio with temperature may be due to increasing amounts of creep during the test [54], a constant value of 0.3 was used for Poisson's ratio.

The determination of the viscoplastic parameters is central to the current study and thoroughly reviewed here. Recall (from Equation 5.18) the dynamic yield stress is defined as

$$\sigma_{dy} = \sigma_0 \left(1 + \frac{\varepsilon_{eq}}{\varepsilon_0} \right)^{1/n} \left(1 + \frac{\dot{\varepsilon}_{eq}}{\dot{\varepsilon}_0} \right)^{1/m} \quad (5.22)$$

Substitution of expressions for reference strain ($\varepsilon_0 = \sigma_0 n / E$) and reference strain rate ($\dot{\varepsilon}_0 = A \exp(-Q/RT)$) into Equation 5.22 yields

$$\sigma_{dy} = \sigma_0 \left(1 + \frac{E \varepsilon_{eq}}{\sigma_0 n} \right)^{1/n} \left(1 + \frac{\dot{\varepsilon}_{eq}}{A \exp(-Q/RT)} \right)^{1/m} \quad (5.23)$$

Hence, five unknown parameters (σ_0 , n , m , A , Q) remain to be determined. To estimate

the parameters at temperatures above the solid-state transformation, stress-strain data from the literature was used, in which uniaxial tests were performed on reheated low-carbon steel specimens. Suzuki *et al.* [5] performed creep tests from 1200 °C to 1400 °C at a single carbon content, while Wray [4] performed tensile tests on steel over a range of carbon contents and strain rates from 850 °C to 1200 °C. The parameters were estimated using a Levenberg-Marquardt algorithm, which minimized the difference between measured and predicted stresses using a least squares method.

To capture the temperature dependence of the dynamic yield stress, the initial yield stress (σ_0), hardening exponent ($1/n$), and rate exponent ($1/m$) were estimated as linear functions of temperature. Using the method from Kozlowski *et al.* [31], the prefactor of the Arrhenius equation, A , was estimated as a quadratic function of carbon content (%C), i.e., $A = A'_0 + A'_1(\%C) + A'_2(\%C)^2$. Substitution of these relations into Equation 5.2 and setting $\varepsilon = \varepsilon_{eq}$ and $\dot{\varepsilon} = \dot{\varepsilon}_{eq}$ for a uni-axial test gives

$$\sigma_{dy} = (\sigma'_0 + \sigma'_1 T) \left(1 + \frac{E\varepsilon}{(\sigma'_0 + \sigma'_1 T)(n'_0 + n'_1 T)} \right)^{\frac{1}{(n'_0 + n'_1 T)}} \left(1 + \frac{\dot{\varepsilon}}{(A'_0 + A'_1(\%C) + A'_2(\%C)^2) \exp(-Q/RT)} \right)^{\frac{1}{(m'_0 + m'_1 T)}} \quad (5.24)$$

Therefore, ten variables ($\sigma'_0, \sigma'_1, n'_0, n'_1, m'_0, m'_1, A'_0, A'_1, A'_2, Q$) needed to be determined. Because only experimental data with strain rates typically found in a casting process ($\dot{\varepsilon} < 10^{-3}$ 1/s) were considered for the parameter estimation, 804 stress-strain measurements were used. The estimated parameters are shown in Table 5.1. Interestingly, the estimated activation energy ($Q = 298$ kJ/mol) is close to the reported value of the self-diffusion of austenite (284 kJ/mol [55]). Because experimental data for austenite was not available below 850°C, the values from Table 5.1 were linearly extrapolated down to the temperature of the approximate solid-state transformation

(700°C).

At the solid-state transformation from austenite to ferrite and pearlite, the mechanical properties of low-carbon steel dramatically change, as the steel gains considerable strength. To estimate viscoplastic parameters temperatures below the solid-state transformation ($T \leq 700^\circ\text{C}$), the experimental data of Maciejewski [56] was used. As reported in the paper, steel behaves as a rate-independent material at temperatures below 300°C, i.e., $1/m = 0$. Accordingly, Equation 5.2 reduces to

$$\sigma_{dy} = \sigma_0 \left(1 + \frac{E \varepsilon_{eq}}{\sigma_0 n} \right)^{1/n} \quad (5.25)$$

As a result, only two viscoplastic parameters (σ_0 and n) must be estimated. Additionally, because the initial yield stress determines the magnitude of the stress-strain curve, and the hardening parameter determines the shape, the parameters (at 20°C and 300°C) were estimated through a trial-and-error method until the predicted stresses matched the experimental stresses. Values between 20°C and 300°C were linearly interpolated. Comparisons between the model and experimental data at the rate-independent temperatures are shown in Figure 5.3.

With parameter estimates complete for the temperature ranges containing rate-independent ($20^\circ\text{C} < T < 300^\circ\text{C}$) and austenitic ($700^\circ\text{C} < T < 1400^\circ\text{C}$) steel, parameters were estimated in the temperature range containing rate-dependent pearlite and ferrite ($300^\circ\text{C} < T < 700^\circ\text{C}$) next. To avoid large jumps in viscoplastic parameters at 300°C and 700°C, the hardening exponent, $1/n$, and rate exponent, $1/m$, were linearly interpolated between 300°C and 700°C. The final hardening and rate exponent curves are shown as functions of temperature in Figure 5.4.

The relation of the reference strain rate at high temperatures (see Table 5.1) was also extended to temperatures below the solid-state transformation. This was considered

a reasonable assumption because rate-dependence below the solid-state transformation plays a diminished role in the stress-strain relationship. The reference strain rate over the entire temperature range is shown in Figure 5.5. As a result, the lone remaining parameter to be determined was the initial yield stress, which was estimated as a linear function of temperature from the experimental data of [56] in the rate-dependent temperature range ($500^{\circ}\text{C} < T < 700^{\circ}\text{C}$). To obtain a complete curve, the initial yield stress was linearly interpolated from 300°C to 500°C . In addition, the instantaneous jump in σ_0 at 700°C was distributed over a finite temperature range of 10°C . The initial yield stress curve is shown in Figure 5.6. For completeness, the reference strain (calculated as $\varepsilon_0 = \sigma_0 n / E$) is shown in Figure 5.7.

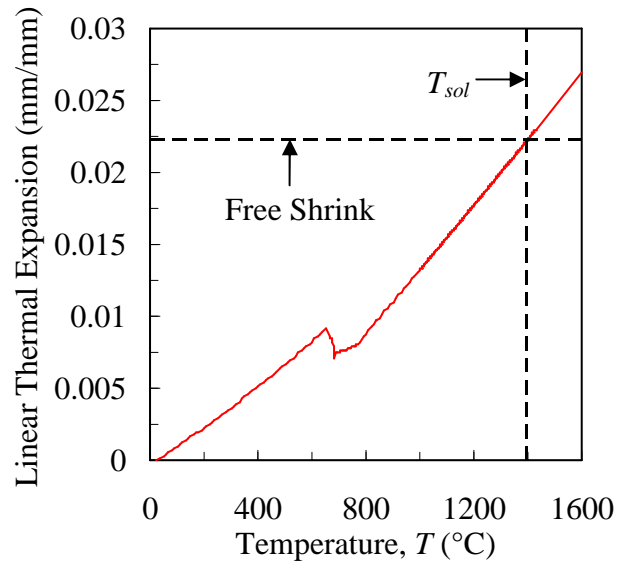
The constitutive model was evaluated based on its ability to reproduce the experimental stress-strain curves that were used to estimate the model parameters. The simulated and experimental curves of Suzuki *et al.* [5] are compared in Figure 5.8. Next, the simulated stress-strain curves are compared to the Wray [4] data at 0.005% (Figure 5.9), 0.051% (Figure 5.10), 0.29% (Figure 5.11), 0.46% (Figure 5.12), 0.71% (Figure 5.13), 0.93% (Figure 5.14), 1.24% (Figure 5.15), and 1.54% (Figure 5.16) carbon contents. Finally, the simulated and measured curves of Maciejewski [56] are compared in Figure 5.17. While the simulated and experimental stress-strain curves generally appear to agree, a quantitative method is needed to check the quality of the fit. To determine the relative accuracy of the model, the root-mean-square (RMS) error between the measured and simulated curves was calculated using the relation

$$RMS\ error = \sqrt{\frac{\sum_{i=1}^n (\hat{y}_i - y_i)^2}{n}} \quad (5.26)$$

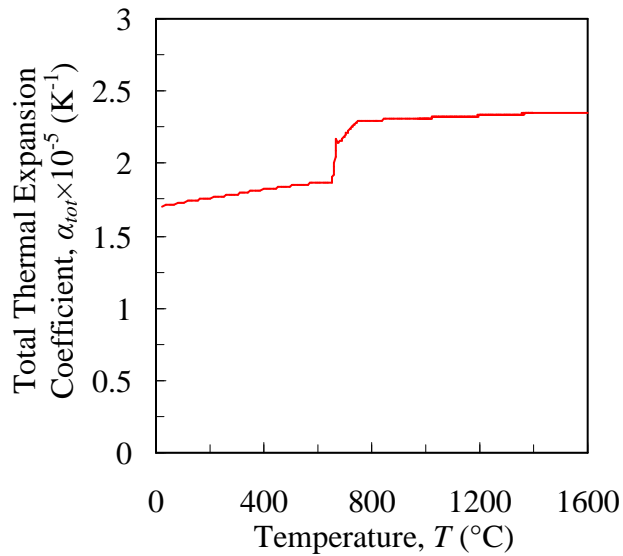
where \hat{y}_i is the predicted value, y_i is the measured value, and n is the number of measurements. While the RMS error alone is not of particular interest, its comparison to

other RMS errors has benefits. For example, temperature-dependent viscoplastic parameters (σ_0 , n , m) were estimated using both linear and quadratic relationships. However, the model accuracy did not improve using the quadratic fit, i.e., the RMS error did not decrease. Therefore, the RMS error is a useful criteria for determining which fit to use. Because using higher order relationships did not improve the RMS error, the lower order (linear) relationships were used.

It can be seen that the RMS values of the Suzuki *et al.* data [5] are generally lower than the other experimental data. However, these experimental data were generated from an equation that was fitted to the experimental data. Because this fit inherently removed the variance in the measurements, the resulting RMS error was very small.



(a) Linear Thermal Expansion



(b) Total Thermal Expansion Coefficient

Figure 5.1 The linear thermal expansion and total thermal expansion coefficient were calculated from the steel density. The total thermal expansion coefficient (defined in Equation 5.9) is the parameter required by ABAQUS to calculate thermal strains.

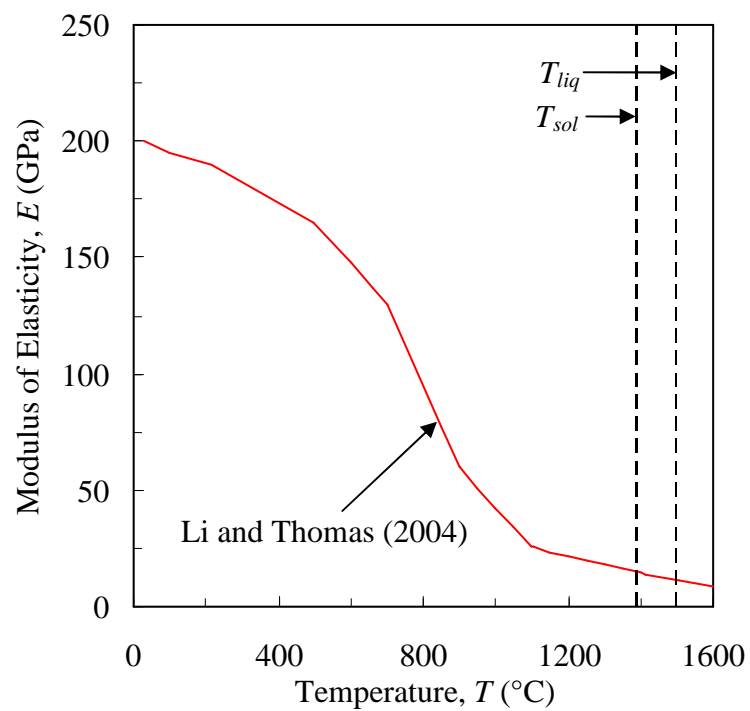
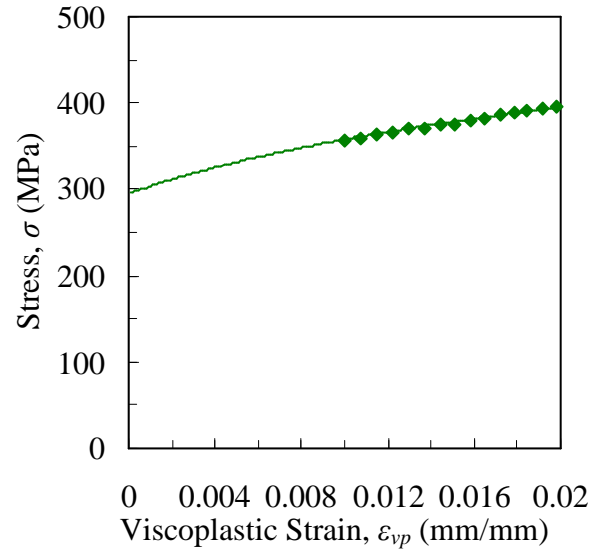


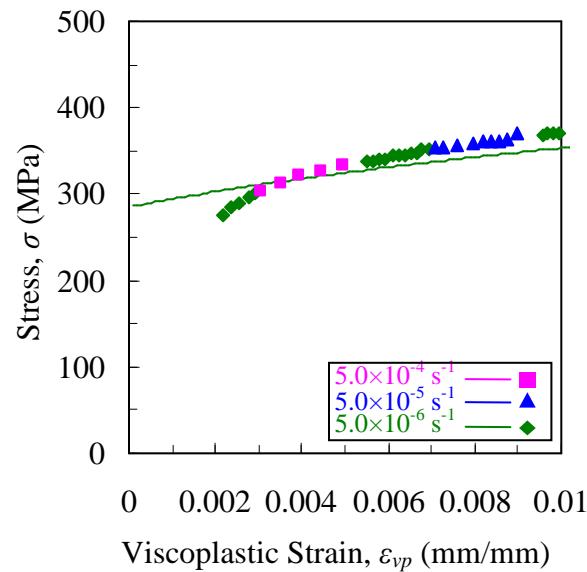
Figure 5.2 Elastic properties included a constant Poisson's ratio of 0.3 and temperature-dependent modulus of elasticity shown above taken from Li and Thomas [32].

Table 5.1. Estimated viscoplastic parameters.

Parameter	Expression	Units
Initial Yield Stress (σ_0)	$3.485 - 1.495 \times 10^{-3} T$	MPa
Hardening Exponent ($1/n$)	$2.327 \times 10^{-1} - 4.181 \times 10^{-5} T$	-
Strain Rate Exponent ($1/m$)	$5.924 \times 10^{-2} + 8.899 \times 10^{-5} T$	-
Arrhenius Prefactor (A)	$1.269 \times 10^4 + 6.131 \times 10^4 (\%C) + 7.134 \times 10^3 (\%C)^2$	1/s
Activation Energy (Q)	298	kJ/mol



(a) 20 °C



(b) 300 °C

Figure 5.3 Comparison between simulated and measured data at 20°C and 300°C from Maciejewski [56]. Because the steel was rate-independent at these temperatures, i.e., $1/m = 0$, only two viscoplastic parameters (σ_0 and n) from the viscoplastic constitutive equation (Equation 18) remained to be estimated.

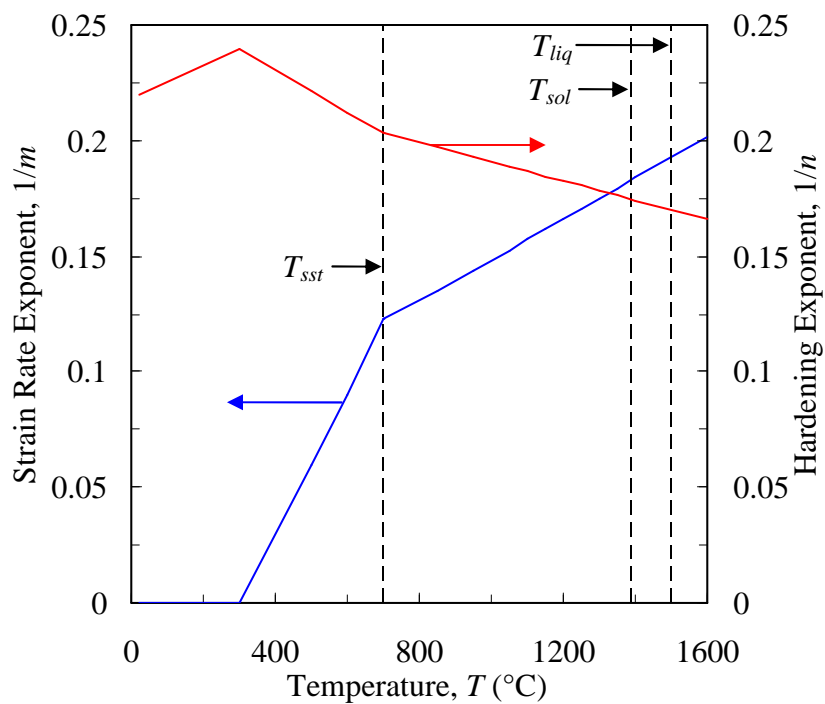


Figure 5.4 Strain rate and hardening exponents. The rate and hardening exponents were estimated using the experimental data of Suzuki *et al.* [5], Wray [4], and Maciejewski *et al.* [56].

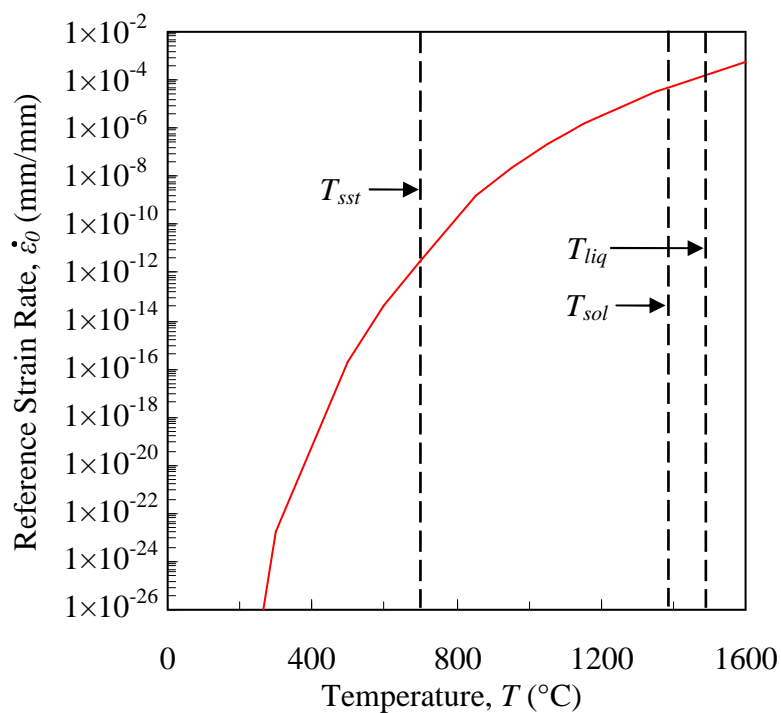
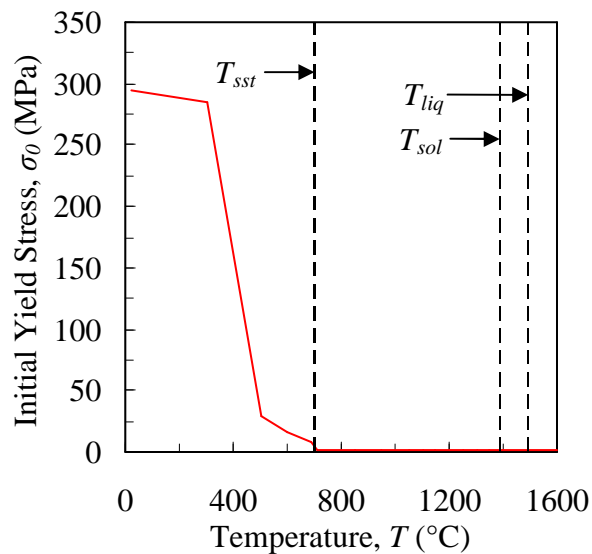
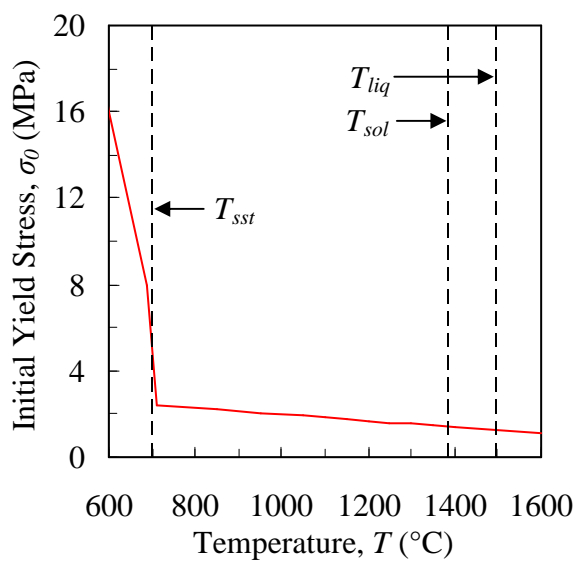


Figure 5.5 The reference strain rate was estimated with the high temperature data of Suzuki *et al.* [5] and Wray [4] and extended to the lower temperatures ($T < 700^\circ\text{C}$).

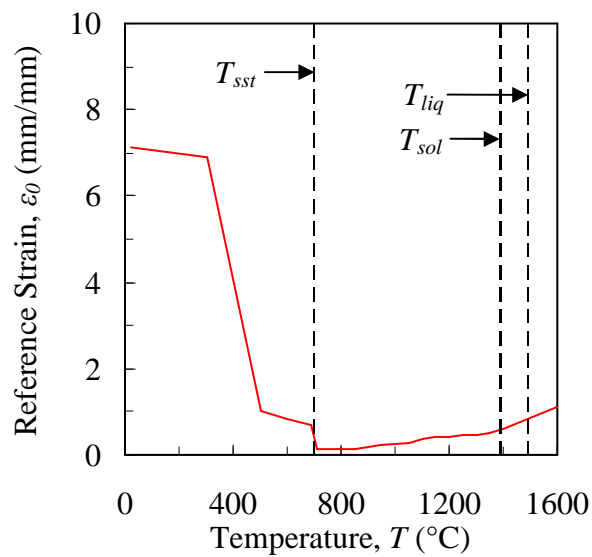


(a) Large stress scale

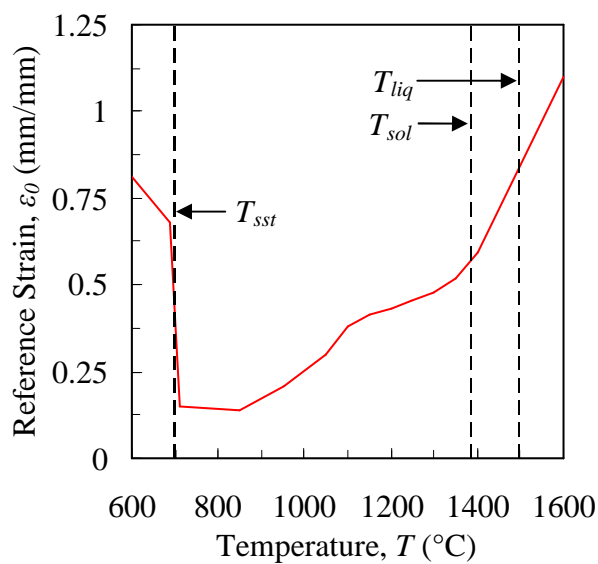


(b) Small stress scale

Figure 5.6 The initial yield stress was estimated using the experimental data of Suzuki *et al.* [5], Wray [4], and Maciejewski *et al.* [56].



(a) Large stress scale



(b) Small stress scale

Figure 5.7 The reference strain was calculated from Young's modulus (E , shown in Figure 5.2), the hardening parameter ($1/n$, shown in Figure 5.4), and the initial yield stress (σ_0 , shown in Figure 5.6) using the relation $\varepsilon_0 = \sigma_0 n / E$.

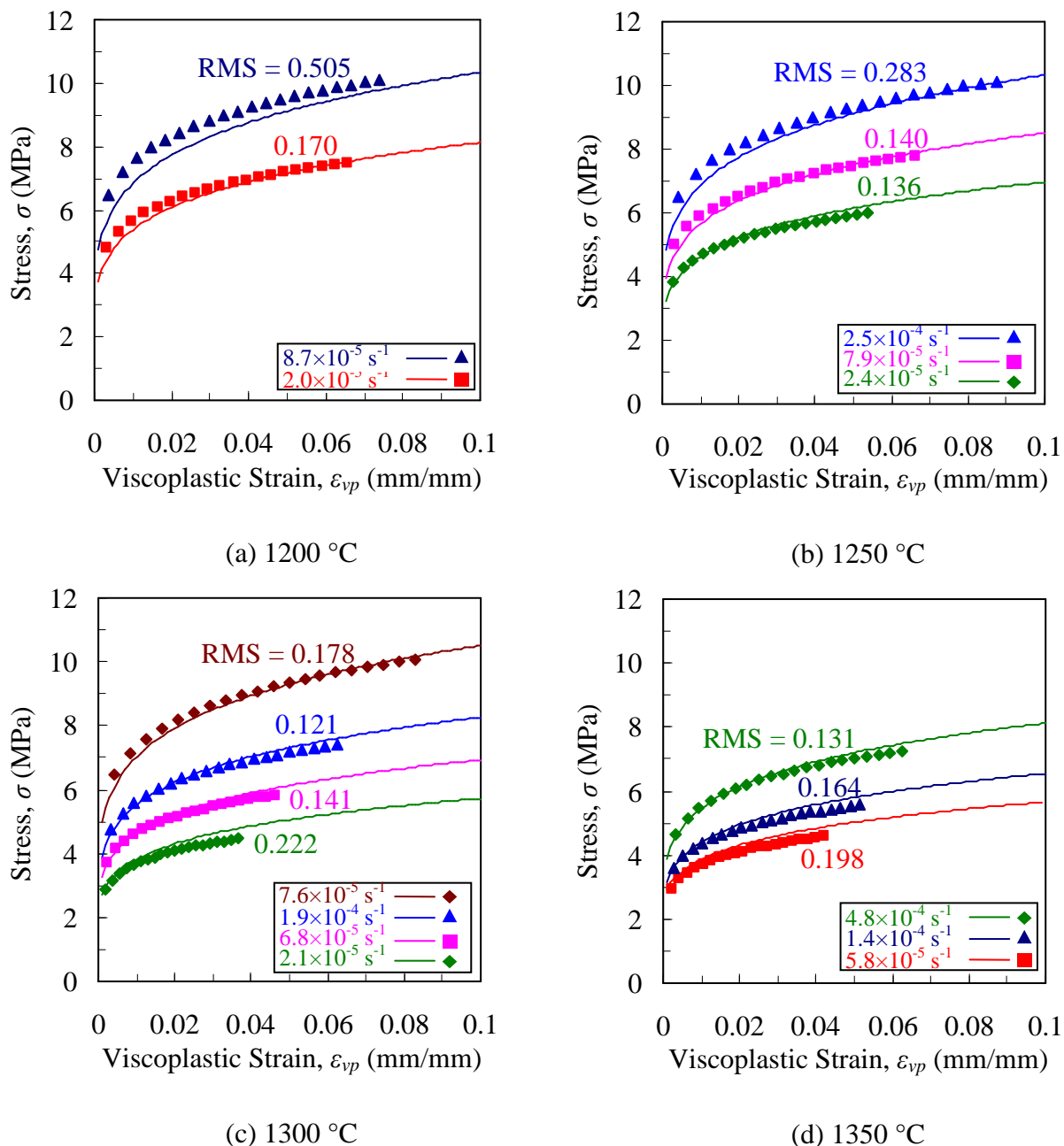
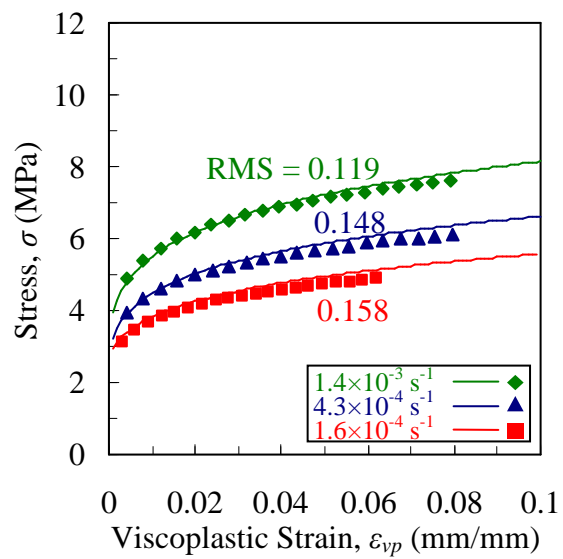
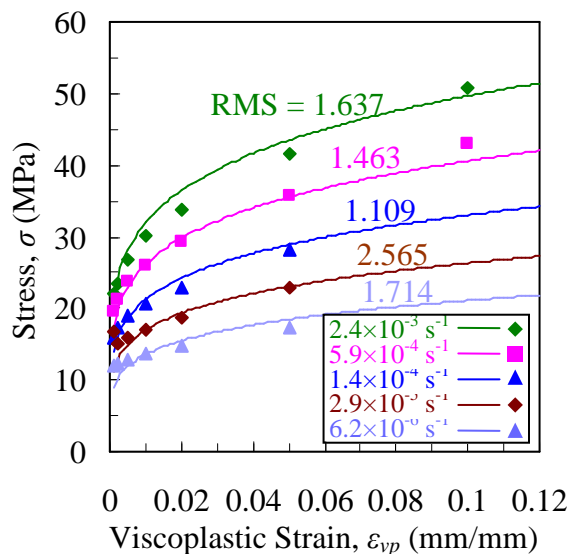


Figure 5.8 Comparison of predicted and measured (from Suzuki *et al.* [5]) stresses at 0.19% carbon content. Each curve represents a different strain rate. The viscoplastic model can be evaluated based on its ability to reproduce the experimental stress-strain curves from which its parameters were estimated. The root-mean-square (RMS) values show the relative error for each curve.

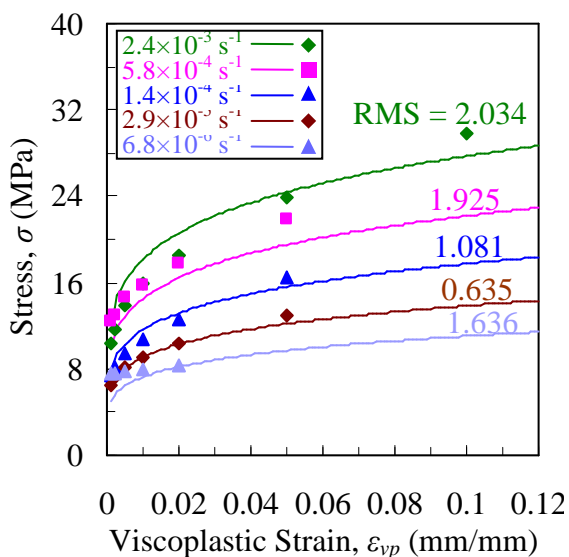


(e) 1400 °C

Figure 5.8 (continued)

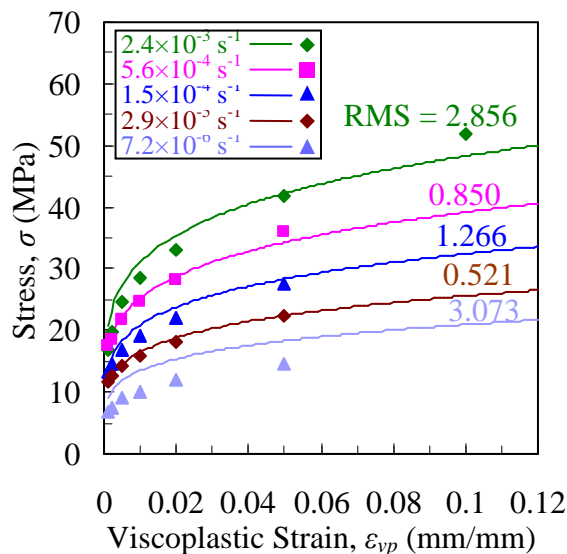


(a) 950 °C

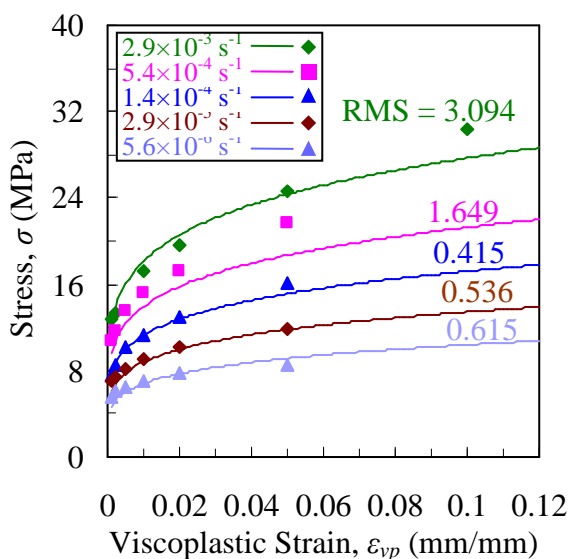


(b) 1100 °C

Figure 5.9 Comparison of predicted and measured (from Wray [4]) stresses at 0.005% carbon content. Each curve represents a different strain rate. The viscoplastic model can be evaluated based on its ability to reproduce the experimental stress-strain curves from which its parameters were estimated. The root-mean-square (RMS) values show the relative error for each curve.

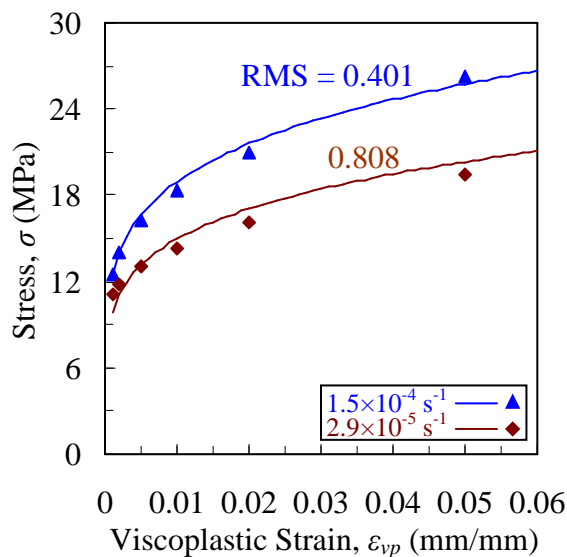


(a) 950 °C

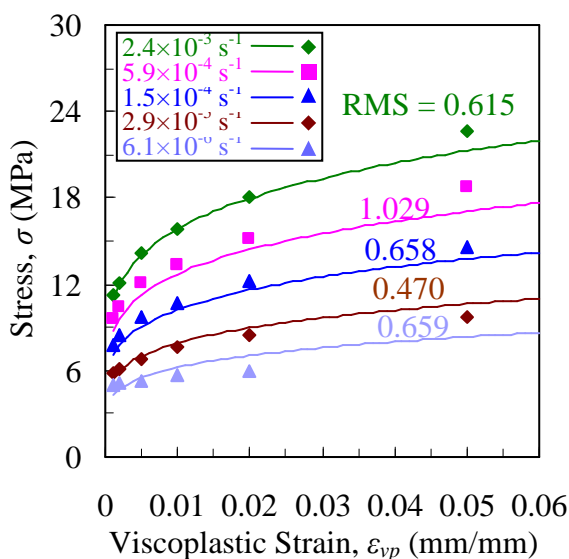


(b) 1100 °C

Figure 5.10 Comparison of predicted and measured (from Wray [4]) stresses at 0.051% carbon content. Each curve represents a different strain rate. The viscoplastic model can be evaluated based on its ability to reproduce the experimental stress-strain curves from which its parameters were estimated. The root-mean-square (RMS) values show the relative error for each curve.

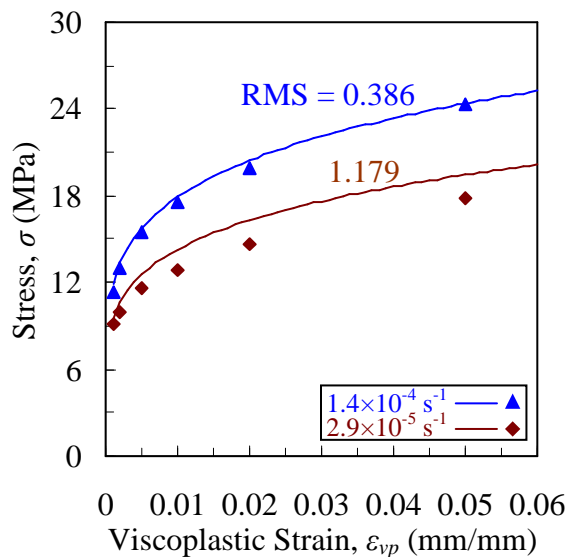


(a) 950 °C

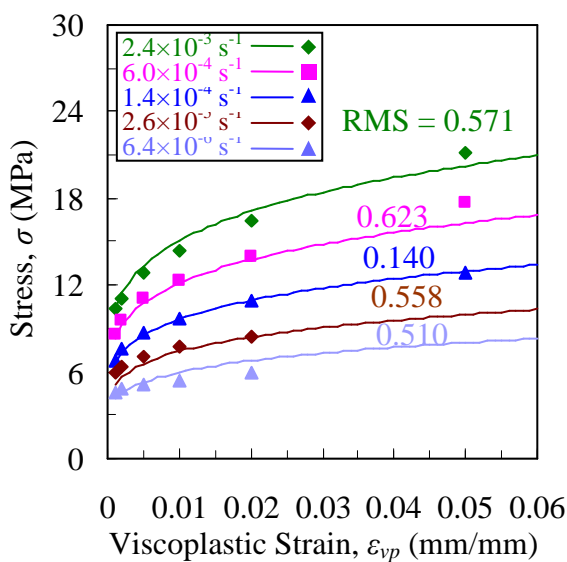


(b) 1100 °C

Figure 5.11 Comparison of predicted and measured (from Wray [4]) stresses at 0.29% carbon content. Each curve represents a different strain rate. The viscoplastic model can be evaluated based on its ability to reproduce the experimental stress-strain curves from which its parameters were estimated. The root-mean-square (RMS) values show the relative error for each curve.

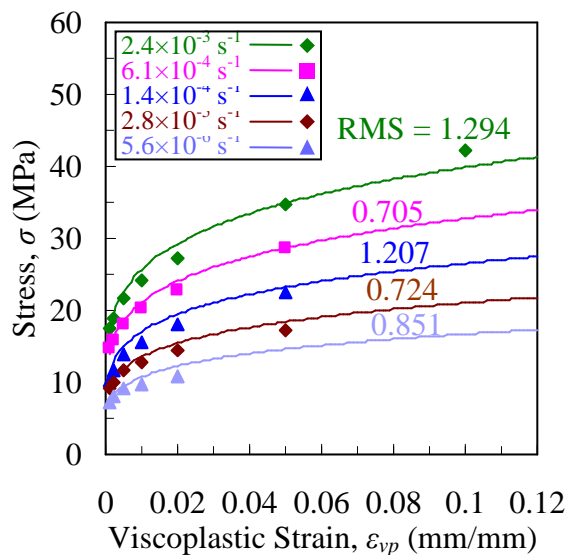


(a) 950 °C

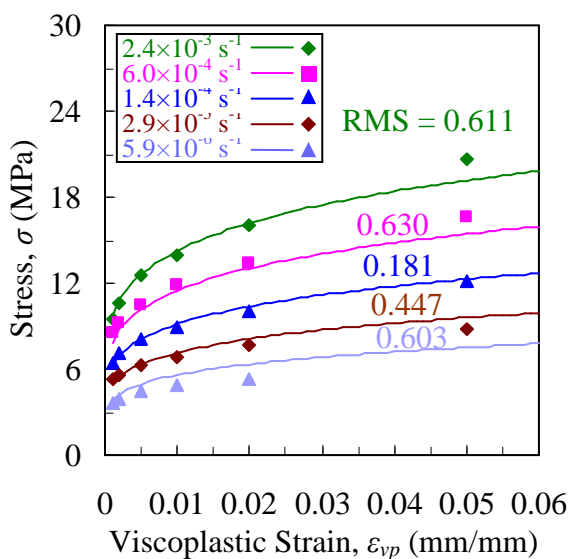


(b) 1100 °C

Figure 5.12 Comparison of predicted and measured (from Wray [4]) stresses at 0.46% carbon content. Each curve represents a different strain rate. The viscoplastic model can be evaluated based on its ability to reproduce the experimental stress-strain curves from which its parameters were estimated. The root-mean-square (RMS) values show the relative error for each curve.



(a) 950 °C



(b) 1100 °C

Figure 5.13 Comparison of predicted and measured (from Wray [4]) stresses at 0.71% carbon content. Each curve represents a different strain rate. The viscoplastic model can be evaluated based on its ability to reproduce the experimental stress-strain curves from which its parameters were estimated. The root-mean-square (RMS) values show the relative error for each curve.

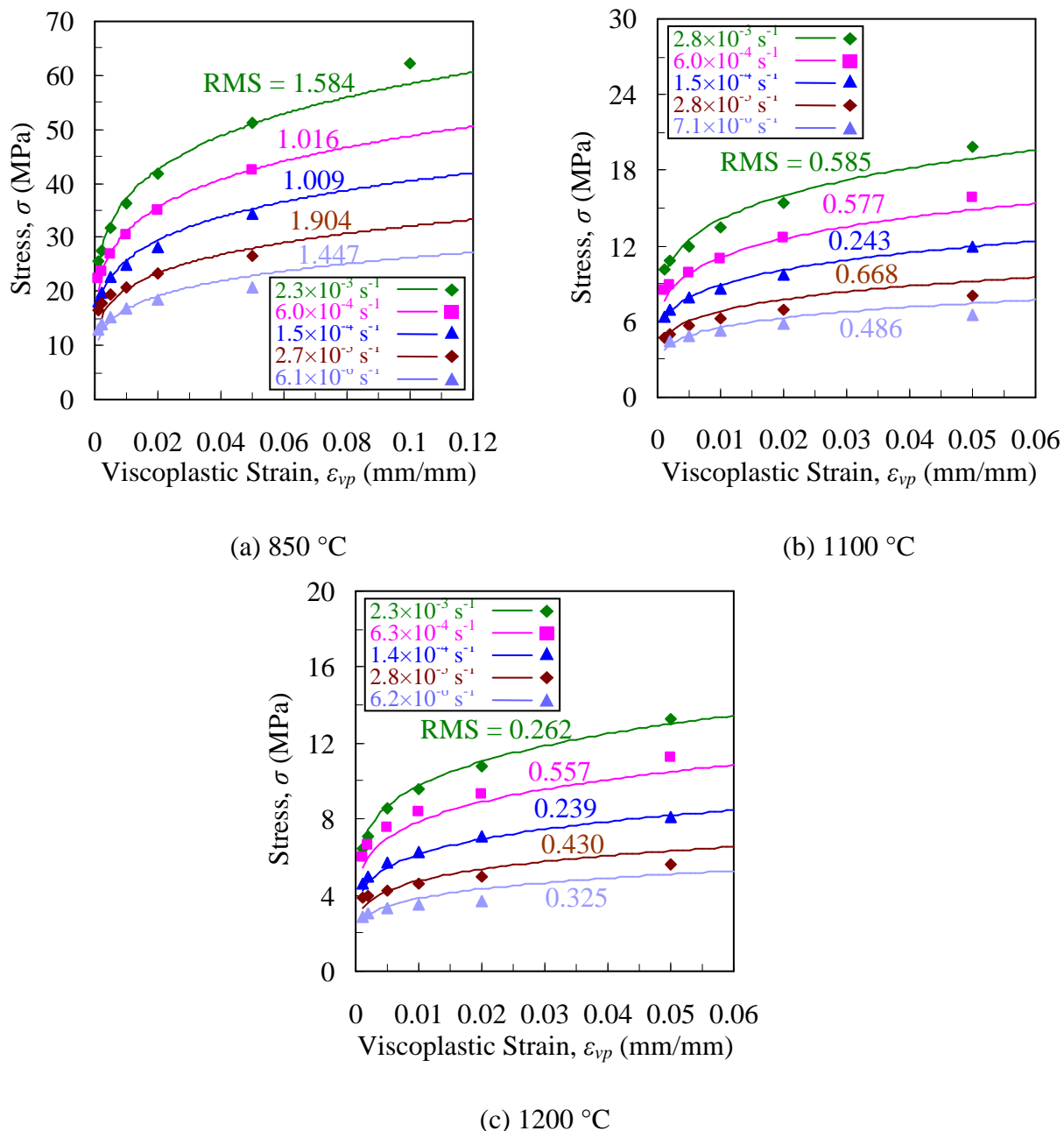


Figure 5.14 Comparison of predicted and measured (from Wray [4]) stresses at 0.93% carbon content. Each curve represents a different strain rate. The viscoplastic model can be evaluated based on its ability to reproduce the experimental stress-strain curves from which its parameters were estimated. The root-mean-square (RMS) values show the relative error for each curve.

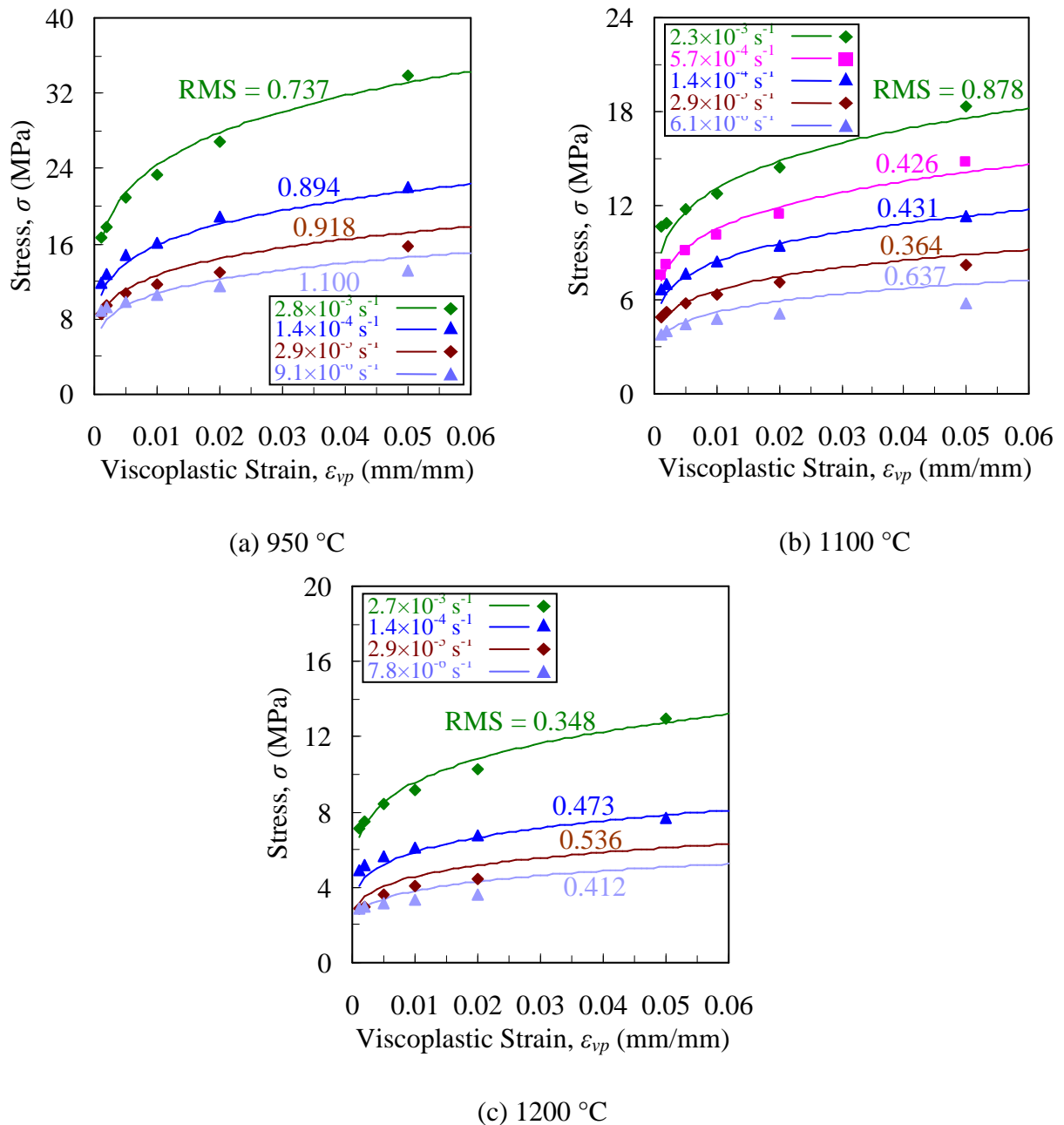


Figure 5.15 Comparison of predicted and measured (from Wray [4]) stresses at 1.24% carbon content. Each curve represents a different strain rate. The viscoplastic model can be evaluated based on its ability to reproduce the experimental stress-strain curves from which its parameters were estimated. The root-mean-square (RMS) values show the relative error for each curve.

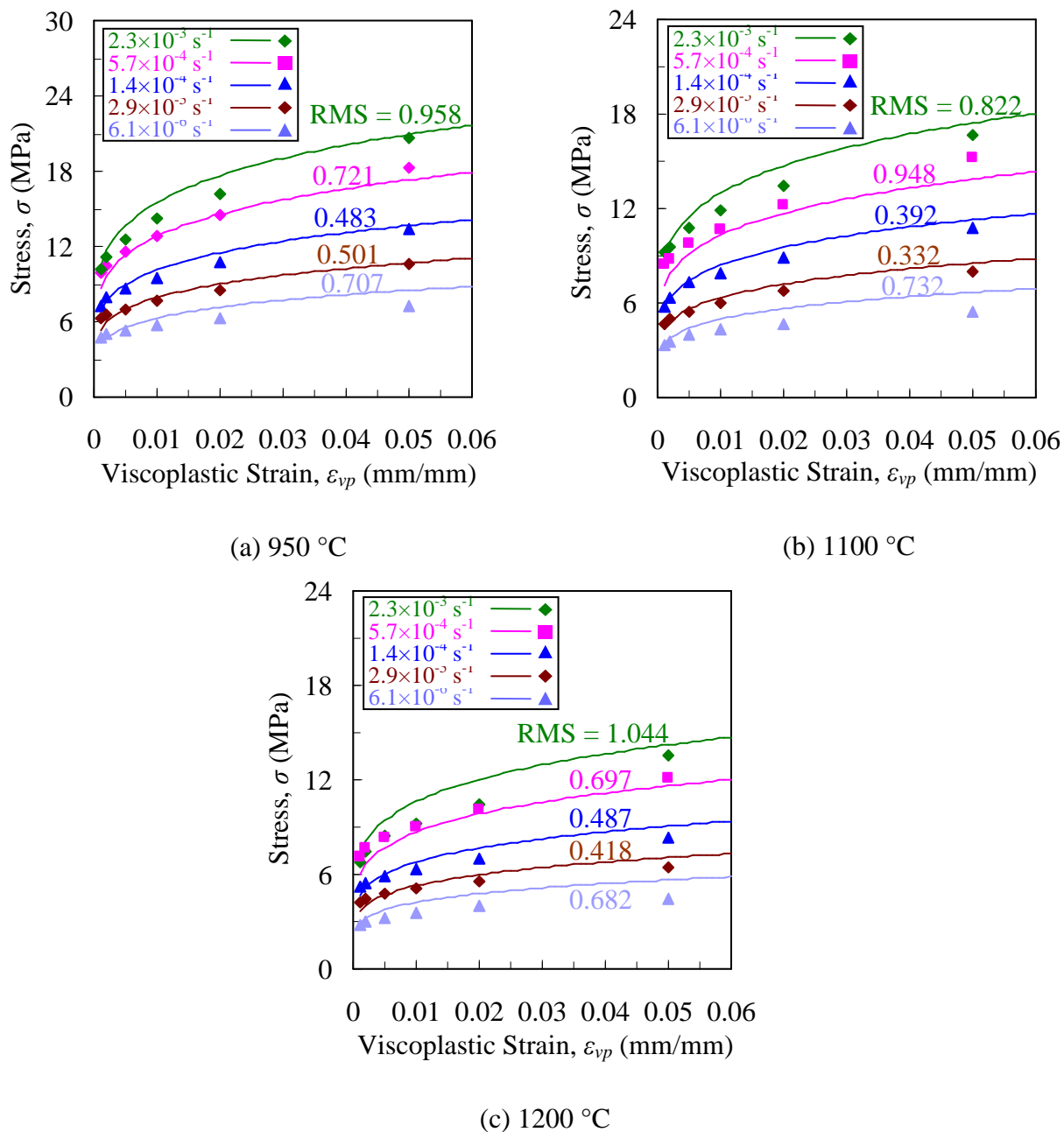


Figure 5.16 Comparison of predicted and measured (from Wray [4]) stresses at 1.54% carbon content. Each curve represents a different strain rate. The viscoplastic model can be evaluated based on its ability to reproduce the experimental stress-strain curves from which its parameters were estimated. The root-mean-square (RMS) values show the relative error for each curve.

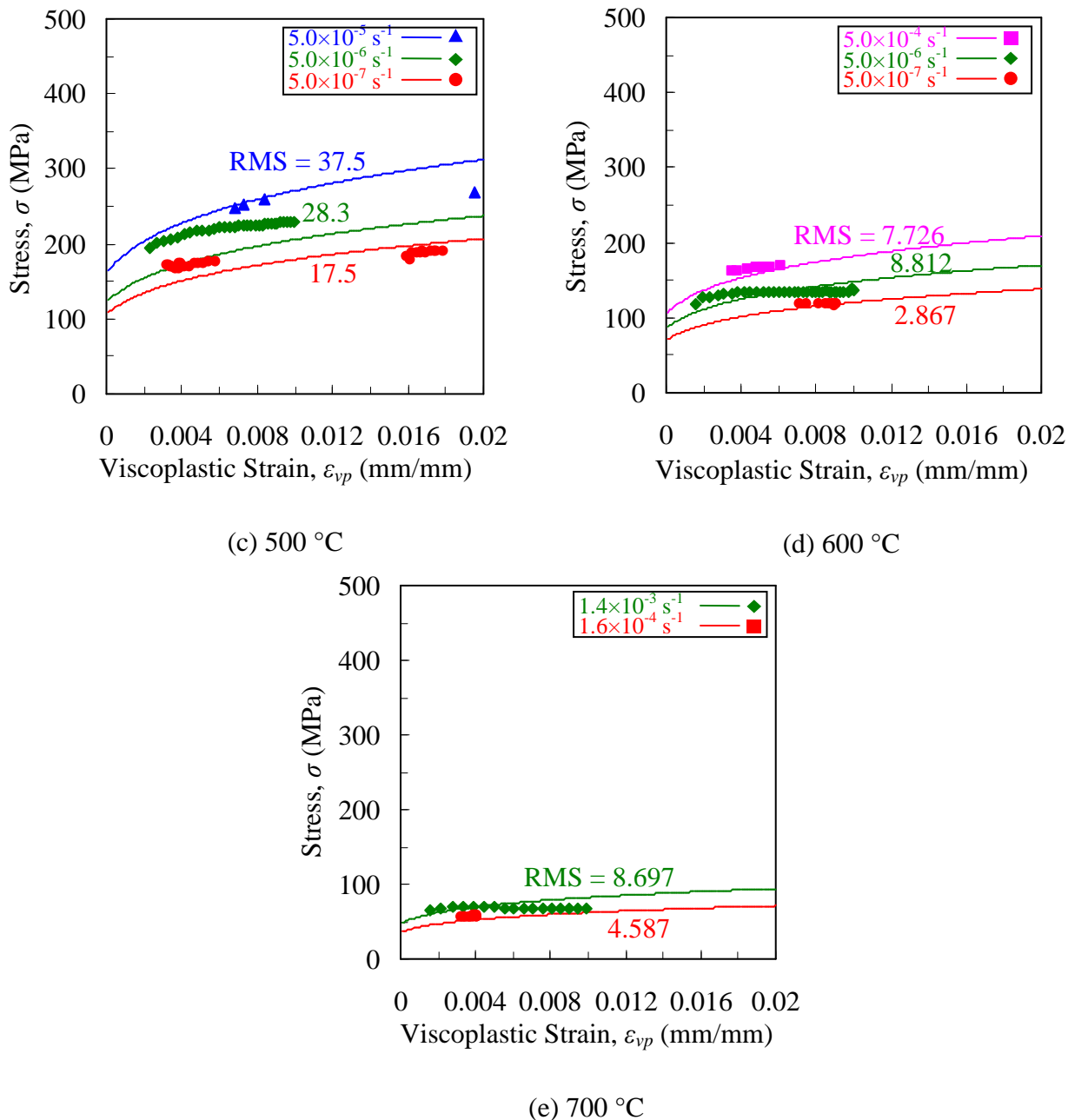


Figure 5.17 Comparison of predicted and measured (from Maciejewski *et al.* [56]) stresses at 0.23% carbon content. Each curve represents a different strain rate. The viscoplastic model can be evaluated based on its ability to reproduce the experimental stress-strain curves from which its parameters were estimated. The root-mean-square (RMS) values show the relative error for each curve.

CHAPTER 6: STRESS SIMULATIONS

6.1 Introduction

In order to calculate stresses and deformations, the simplified solid momentum equation (Equation 5.3) was solved using the finite element software ABAQUS. The viscoplastic constitutive model, which was implemented with a user-defined UMAT subroutine, required additional inputs to account for temperature and pressure-dependent effects. Temperature-dependent mechanical properties were determined at all times and locations throughout the bar using the MAGMAsoft temperature fields, which were transferred to the ABAQUS mesh using MAGMALink. The volume solid fraction, shown as the “after adjusted” curve in Figure 4.13(d), was also needed to calculate deformation in pressure-dependent mushy zone.

To save computational costs, the steel in the pouring basin and mold were excluded from the ABAQUS model, due to their minimal contribution to the generation of stresses in the bar. The finite element meshes were constructed with second-order tetrahedral elements containing approximately 25000 and 28000 elements for the small-sprue and large-sprue simulations, respectively.

Distortions in the Strained experiments were predicted in a two-step process. First, the Unrestrained bars, which served as the experimental control, were simulated to determine the thermal expansion coefficient, which was then used in conjunction with the measured force (as a boundary condition) to predict the total strain in the Strained bars. To validate the model, the predicted and measured length changes were matched through an adjustment to the viscoplastic parameters.

6.2 Unrestrained Simulations

The ABAQUS model for the Unrestrained simulations is shown in Figure 6.1. A zero-displacement boundary condition was enforced on the left side of the bar, i.e., $u_x = u_y = u_z = 0$. During the experiments, normal forces between the mold and casting

constrained the displacement of the bar primarily to the axial direction. However, because the mold was not included in the simulations, an additional displacement boundary condition ($u_y = u_z = 0$) was required to keep the right side of the bar from “floating” in the non-axial directions. By applying the additional boundary condition at a single node, any imaginary stresses resulting from this boundary condition were minimized.

Recall from Chapter 3 that mold symmetry and small frictional forces resulted in the generation of negligible mechanical strains in the Unrestrained experiments. As a result, dimensional changes were due to thermal contractions only. Thus, to calculate the final dimensions, only the total thermal expansion coefficient (α_{tot}) and coherency temperature (T_{coh}) (from Equation 5.8) were required.

The Unrestrained 1 experiment was simulated first. For the initial simulation, the total thermal expansion coefficient was calculated (using equation 5.9) from the IDS temperature-dependent density and the coherency temperature (initially set as the solidus temperature). A comparison between the simulated and measured axial length changes, shown in Figure 6.2, shows the “initial” curve begins to diverge from the “measured” curve at approximately 150 s (shown on the medium time scale). In other words, the simulated bar contracts too much. The gap between the “measured” and “initial” curves gradually increases with time, until there is approximately a 1 mm difference between the measured and simulated axial length changes at 12000 s. Through a trial-and-error method, adjustments to α_{tot} (shown in Figure 6.2(c)) and T_{coh} (from 1410°C to 1430°C) resulted excellent agreement, as can be seen by the “measured” and “after adjusted” curves in Figure 6.2. The same adjusted total thermal expansion coefficient was used to match the simulated and measured axial length changes in the other Unrestrained experiments, shown in Figure 6.3 and Figure 6.4.

Whereas a single total thermal expansion coefficient was used for all Unrestrained simulations, the coherency temperature was uniquely modified for each simulation to

some value above the solidus temperature. Choosing a coherency temperature above the solidus temperature is logical because a solid network capable of transmitting stresses forms at some time during solidification. Therefore, the onset of thermal contraction is likely to commence at this time (or shortly afterwards). Initially, the coherency temperature was assigned to coincide with a specific solid fraction value; for example, thermal contraction might begin when the casting is 90% solidified. However, this method did not result in good agreement for several reasons. First, the solidus temperature can only be determined within a few degrees of its true value. Additionally, the solidus temperature varies throughout the casting. Furthermore, experimental temperatures were only recorded at two locations. Therefore, because the simulations were only matched to experimental data at these two locations, the simulated temperature fields likely contained errors. Because of these uncertainties, determination of the actual coherency temperature was unlikely. Rather, the coherency temperature was treated as an adjustable parameter to achieve agreement in all experiments (including the Strained bars). For all simulations, the adjusted coherency temperature varied from 20-40°C above the experimental solidus temperatures; this variation roughly coincides with the difference in measured solidus temperatures between the Sprue and Right locations (shown in Table 3.2).

Because the total thermal expansion coefficient is a function of the temperature-dependent density, an adjustment to either property requires a re-calculation of the other. The density curve needed to obtain the adjusted thermal expansion coefficient is shown in Figure 6.5. The maximum relative change between the “IDS” and “adjusted” curves is approximately 0.8%, which occurs at the solidus temperature. Therefore, due to the uncertainties at these high temperatures, this small adjustment is justified.

6.3 Strained Simulations

The ABAQUS model of the Strained bar, shown in Figure 6.6, contains the same

displacement boundary conditions as the Unrestrained model. Additionally, a force boundary condition (using the measured Right load bolt force in Figure 3.1(a)) was applied at the right end of the bar. Also, to account for the measured force imbalance described in Chapter 3, the difference between the Left and Right load bolt forces was added as a boundary condition at the base of the sprue.

Because the temperatures vary with time and position throughout the bar, the application of an axial force will yield different amounts of viscoplastic strain in various regions. Therefore, consideration of the temperature fields during the straining period provides insight as to where these strains are likely to occur. Simulated temperature fields of the Strained 1 (small-sprue) and Strained 4 (large-sprue) bars at the beginning and end of the straining periods are shown in Figure 6.7 and Figure 6.8, respectively. From these images, several interesting observations can be made. First, significant temperature variations are seen throughout the cross-sections of the bars, with the middle being hottest. Therefore, it is possible (and likely) to transmit stresses through an outer solidified shell of the cross-section before the middle has reached coherency; in this case, the shell will provide the majority of resistance to deformation, while the middle of the bar may still be liquid and contribute minimal restraint. Next, an increase in the sprue size also increases the axial temperature gradients along the bar. For example, at the beginning of the straining period for the small-sprue bar, the center of the cross-section is nearly isothermal along the length, while the large-sprue temperatures decrease nearly 150°C in the same distance. As a result, an even distribution of viscoplastic strains should be expected along the length of the small-sprue bar, whereas plastic deformations in the large-sprue bar are likely to be concentrated near the sprue. Preliminary stress simulations show this to be the case, as a higher concentration of equivalent plastic strains are seen near the center of the large-sprue bar than the small-sprue bar (shown in Figure 6.9). However, the differences are not large, and significant plastic deformation still occurs in all regions of both bars. Therefore, even when the temperatures throughout

the bar vary by over 200°C (as in the Strained 4 experiment at the beginning of the straining period), significant distortions still occur in all areas. As a final observation, the majority of viscoplastic strain is predicted on the left side of the bar due to the additional force boundary condition at the sprue.

Individual stress simulations were performed for all six Strained casting trials. Figure 6.10 shows a comparison between measured and simulated axial length changes of the Strained 1 experiment. On the large time scale, shown in Figure 6.10(a), the agreement between the “measured” curve and “before adjustment” curve appears reasonable. However, from the medium and small time scales, the viscoplastic strain is seen to have been grossly over-predicted, as the predicted length change increases to approximately 0.25 mm at 100 s. Before the straining period (which is bounded by the vertical red dashed lines in Figure 6.10(c)), the measure and simulated axial length changes are in good agreement, as the total strain in the bar is due to thermal contractions only and calculated using the total thermal expansion coefficient. However, the curves begin to diverge early in the straining period, as the simulated casting is too weak and deforms easily. Therefore, to strengthen the steel, changes to one or more of the viscoplastic parameters are needed. Because rate effects are most influential at high temperatures, the strain rate exponent, $1/m$, was adjusted, shown as the “after adjusted” curve in Figure 6.10(d), which resulted in excellent agreement between measured and simulated curves.

The strain rate exponent of the Strained 2 bar experiment was adjusted in a similar manner, as shown in Figure 6.11, as the initial simulation once again predicted too much viscoplastic strain. Conversely, the initial simulations for the Strained 3, 4, 5, and 6 bars (shown in Figure 6.12, Figure 6.13, Figure 6.14, and Figure 6.15, respectively) predicted too little viscoplastic strain. Nevertheless, the adjustments needed to achieve agreement were similar to those in the Strained 1 and 2 simulations, as shown in Figure 6.16. This can be explained by observing whether the Sprue location (and therefore, the entire bar)

had completely solidified before or during the straining period. In other words, was time of the Sprue solidus bounded by the straining period? Figure 6.10 through Figure 6.15(c) show this relation. Strained 1 and 2 bars were strained before the Sprue location had completely solidified. Therefore, an adjustment to the strain rate exponent at temperatures close to the solidus ($T > 1300^{\circ}\text{C}$) significantly affected the prediction of viscoplastic strain. For the Strained 3, 5 and 6 bars, however, solidification at the Sprue location was complete (or nearly complete) before the induced straining period began. In this case, adjustments to the strain rate exponent at temperatures near the solidus would have a much smaller effect on the prediction of viscoplastic strain.

From the summary of adjusted strain rate exponents (shown in Figure 6.16), the Strained 4 simulation appears to be an outlier, as the strain rate exponent curve lies significantly lower than the other curves. From the simulation (shown in Figure 6.13), the “measured” and “after adjustment” curves agree until 150 s, after which the simulated length change decreases too quickly. Therefore, (assuming the thermal strains are accurately predicted) it appears as though the mechanical strains are larger in the measurement than the simulation. However, the straining period began at 80 s, but the Sprue location did not solidify until 120 s (shown in Figure 6.13(c)). This suggests that considerable damage may have occurred during the experiment. The radiograph of the Strained 4 bar in Figure 3.5(b) supports this notion, as the dark regions around the sprue signify damage. Conversely, the same area is brighter in the small-sprue bar (shown in Figure 3.5(a)), which suggests a sound casting. The effect of damage would result in the measurement of positive length change. The inability of the deformation model to predict the length change suggests the damage may have occurred after solidification was complete. For the current model, damage must nucleate in the mushy zone, after which it may grow and coalesce either during or after solidification. Therefore, if no damage exists at the time of solidification, the model will never predict damage, regardless of the magnitude of applied forces. In order to predict the effects of damage in this situation,

the strain rate exponent must be reduced to a very low value.

Recall that a slight change in the casting chemistry effects the solid-state transformation, which is manifested through the different sizes of “wiggles” seen in the measured axial length changes. Because of this sensitivity, slight adjustments to the total thermal expansion coefficient, shown in Figure 6.17, were needed at the solid-state transformation to achieve reasonable agreement for each Strained experiment. After these small adjustments, any remaining disagreement during the solid state transformation is likely due to differences between measured and simulated temperatures.

A sensitivity study demonstrated that the adjustments to the strain rate exponent were not arbitrary but indeed necessary. Certainly, the entire original curve could have been shifted either up or down to decrease or increase the total amount of predicted viscoplastic strain. However, this method could only predict the total amount of viscoplastic strain for a single experiment but not the times at which it occurred. In other words, a simple shift in the preliminary strain rate exponent curve (shown in Figure 5.4) would not accurately characterize the stress-strain relationship in the steel casting. Hence, the manner in which the curves were adjusted, as shown in Figure 6.16, was necessary to achieve agreement. As an illustration, stress simulations were performed using two iterations of the adjusted strain rate exponent from the Strained 1 bar experiment. In the first iteration, the strain rate exponent curve was matched to the “initial” curve at lower temperatures and “final” curve at higher temperatures (shown in Figure 6.18(d)). The results show the simulation predicted too little viscoplastic strain, shown by the “iteration 1” curve on the small time scale in Figure 6.18(c). For the next iteration, the “iteration 2” curve was matched to the “initial” curve at higher temperatures and “final” curve at lower temperatures (shown in Figure 6.19(d)). This resulted in the prediction of too much viscoplastic strain, shown by the “iteration 2” curve in Figure 6.19(c). These two iterations sufficiently demonstrate that adjustments to the strain rate exponent were not arbitrary. Reasonable agreement for all experiments could only be

achieved using these adjustments.

In all stress simulations, significant changes to the strain rate exponent were needed to achieve agreement between predicted and measured length changes. Although only a single parameter was adjusted, it is likely that other viscoplastic parameters also contribute to differences in the mechanical behavior (between a reheated specimen and steel casting). However, the harsh, dynamic conditions encountered in the casting experiments made it impossible to determine these parameters individually. Although other parameters could have likely been adjusted to achieve agreement, the strain rate exponent was chosen as the adjustable parameter based on its importance at high temperatures. In addition, adjustments to multiple parameters would have been arbitrary. The conclusion to be reached is that the mechanical response of a reheated steel specimen (from which preliminary mechanical properties were estimated) is significantly different than a solidified steel casting. Therefore, the experimental data from Wray [4] and Suzuki *et al.* [5] cannot be used to accurately characterize the material behavior in a steel casting. These preliminary parameters should be used only as a first estimation and subsequently adjusted to match the experimental data from *in situ* casting experiments.

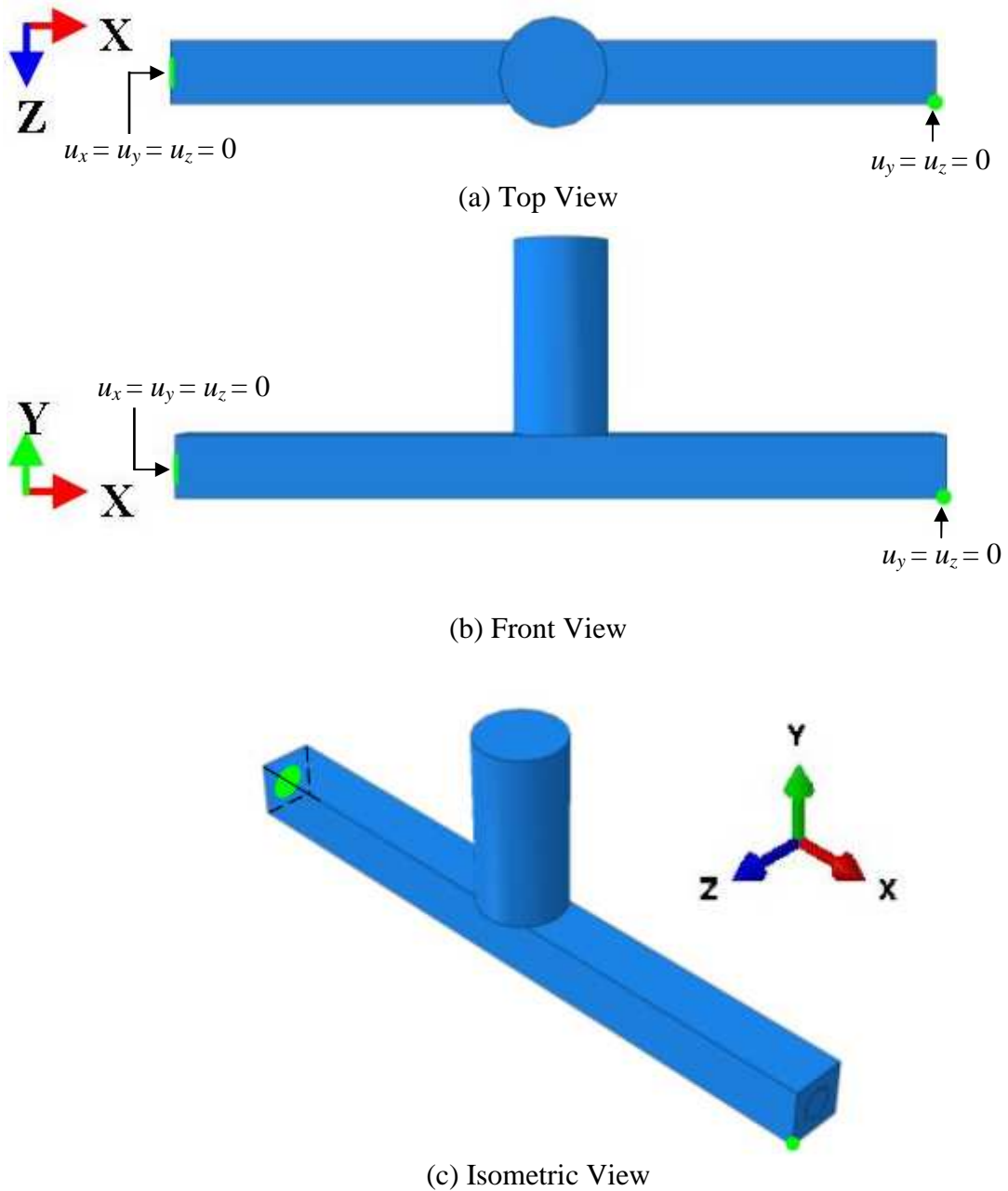
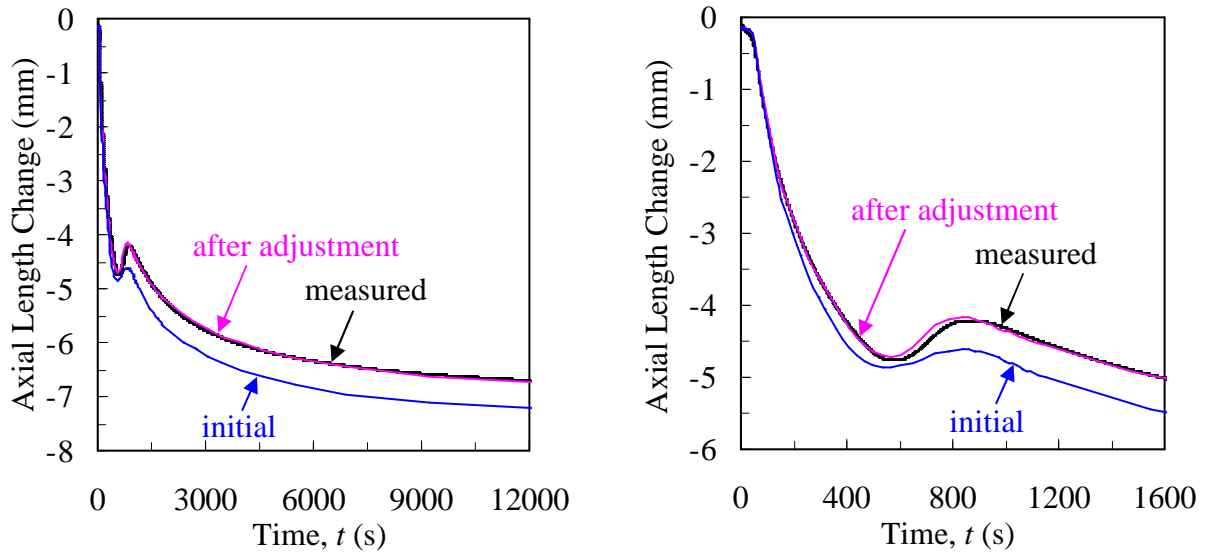
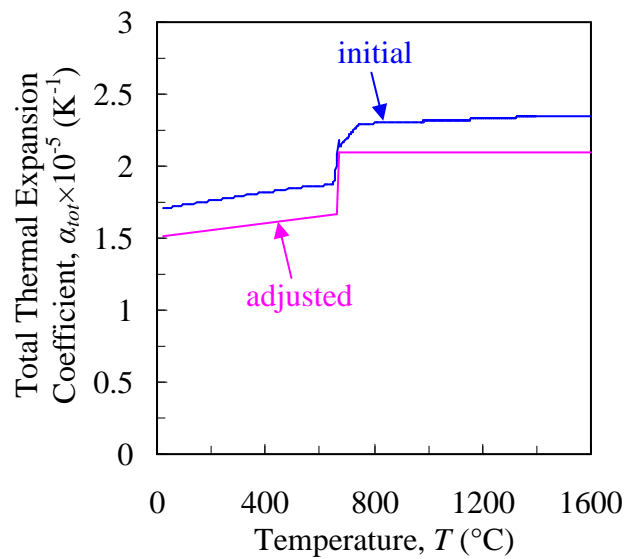


Figure 6.1. ABAQUS model of the Unrestrained bar. To save computational costs, the steel in the pouring cup was not included in the simulations. Because the mold was not included in the stress simulations, an additional boundary condition was required on the right side of the model to restrict the bar to thermal contraction in the axial direction.



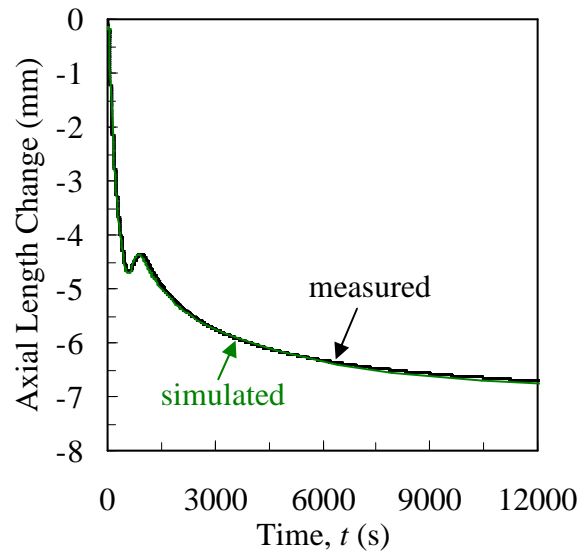
(a) Large Time Scale

(b) Medium Time Scale

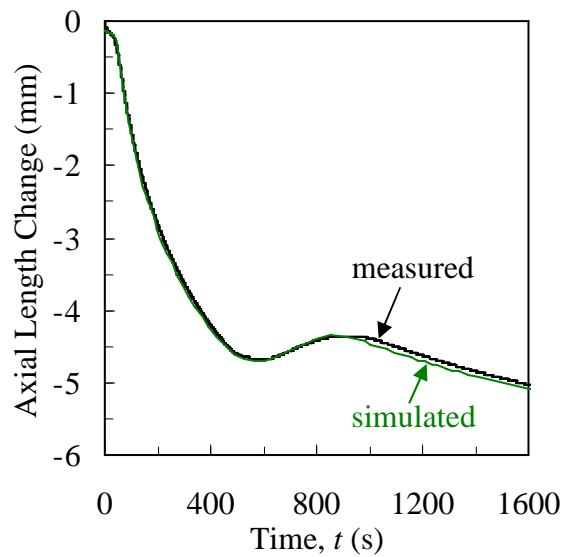


(c) Total Thermal Expansion Coefficient

Figure 6.2. Stress simulation of Unrestrained 1. The “initial” curves use the IDS density to calculate the total thermal expansion coefficient. The “adjusted” total thermal expansion coefficient results in excellent agreement between measured and simulated axial length changes.

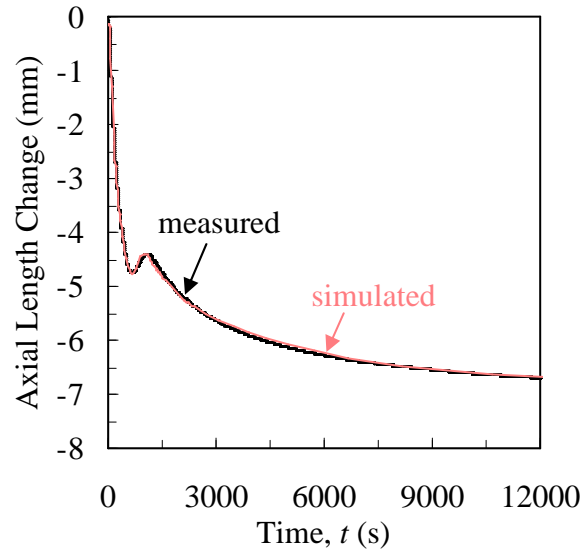


(a) Large Time Scale

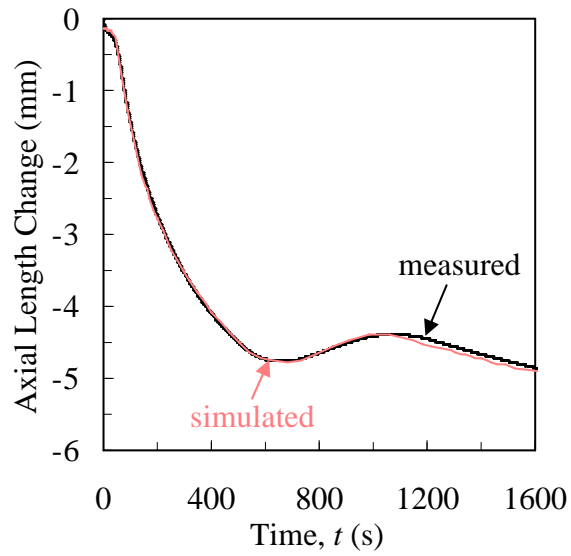


(b) Medium Time Scale

Figure 6.3. Stress simulation of Unrestrained 2. The “adjusted” total thermal expansion coefficient from Figure 6.2(c) was used for the simulation.



(a) Large Time Scale



(b) Medium Time Scale

Figure 6.4. Stress simulation of Unrestrained 3. The “adjusted” total thermal expansion coefficient from Figure 6.2(c) was used for the simulation.

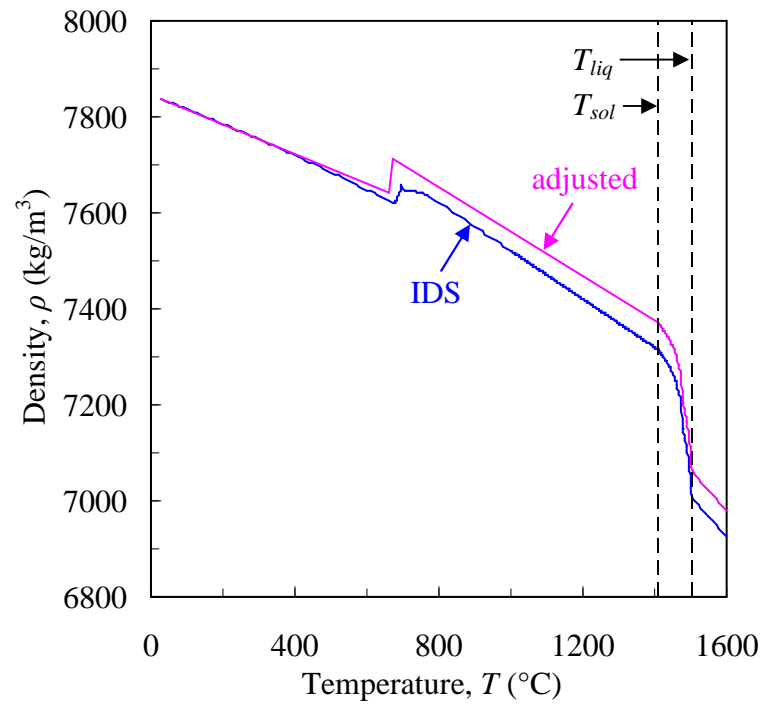


Figure 6.5. Density of the steel. The adjusted total thermal expansion coefficient, shown in Figure 6.2(c), is calculated using the “adjusted” density curve. The maximum relative difference between the curves is 0.8% (at the solidus temperature).

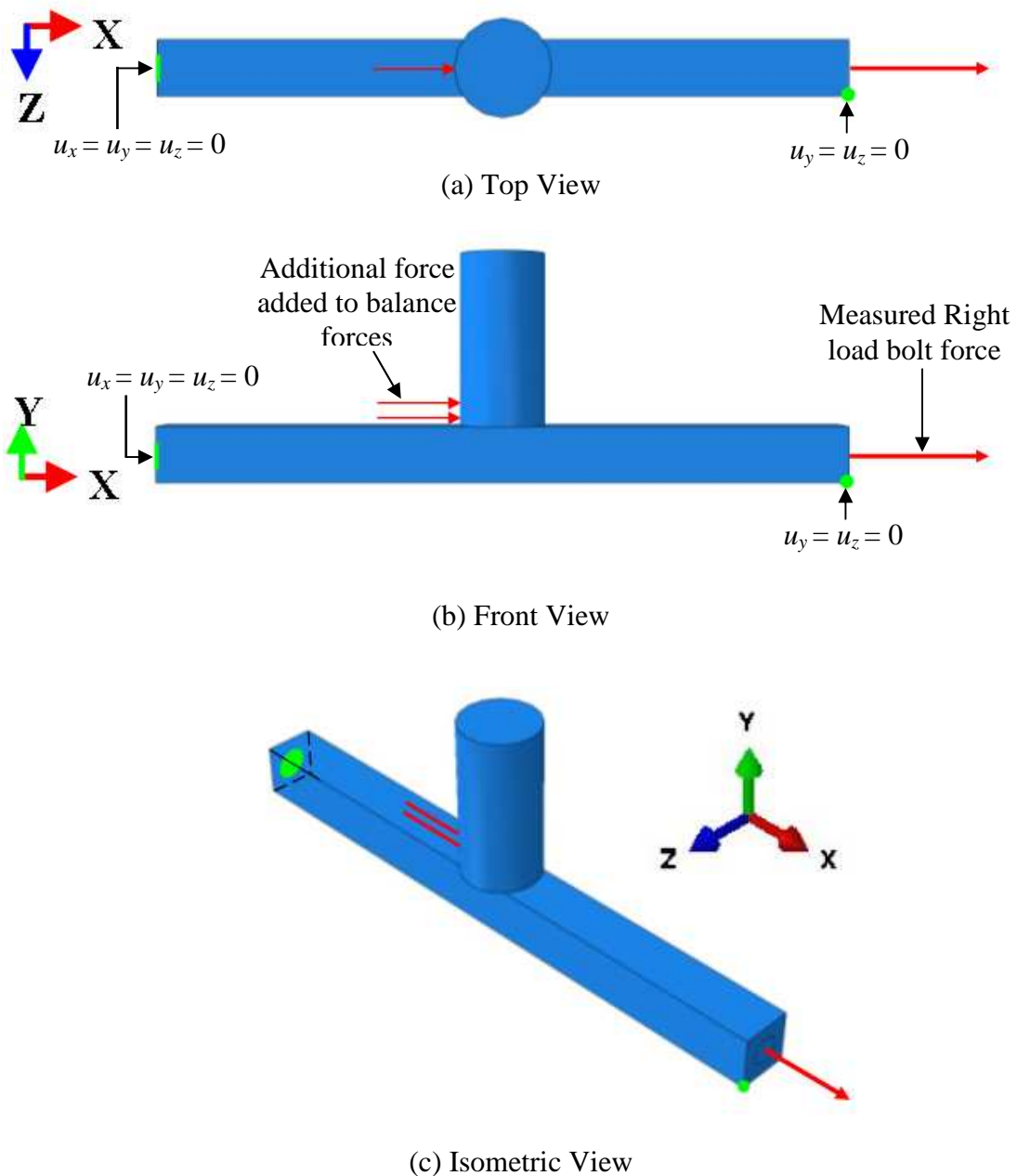


Figure 6.6. ABAQUS model of Strained bar. The displacement boundary conditions are the same as the Unrestrained bar (shown in Figure 6.1). The measured force from the Right load bolt is used as the force boundary condition on the right side of the bar. An additional force boundary condition is required at the base of the sprue to account for the force imbalance between the Left and Right force measurements.

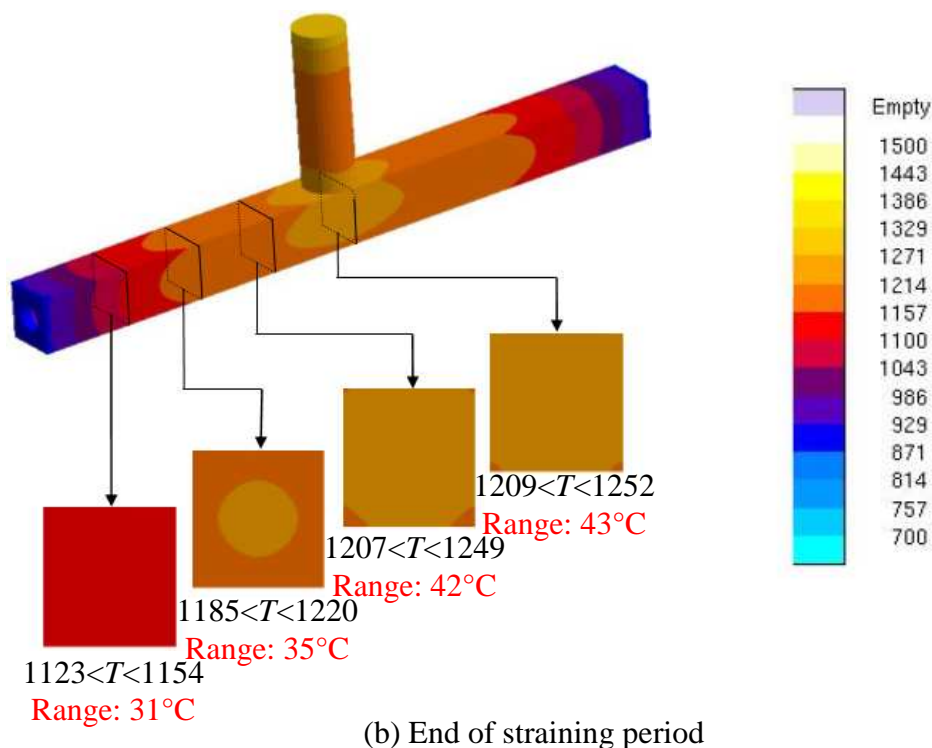
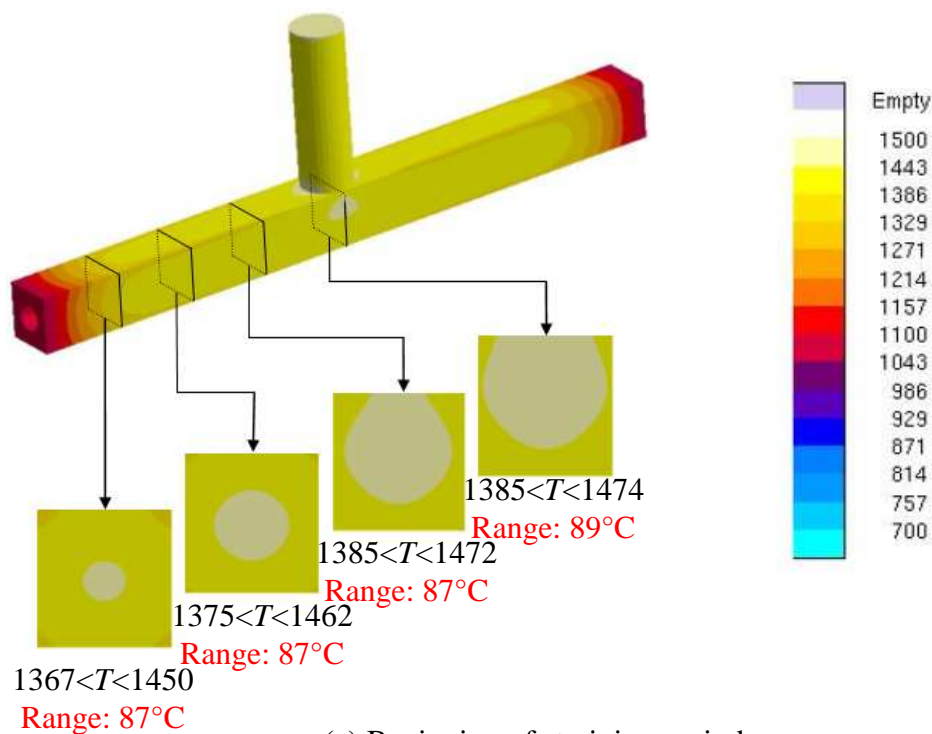


Figure 6.7. Simulated thermal fields of the small-sprue Strained bar at the beginning (a) and end (b) of the straining period. At the beginning of the straining period, the highest temperatures in the cross-section of the bar only have a range of 24°C ($1450 < T < 1474^{\circ}\text{C}$), resulting in relatively isothermal conditions along the axis (compared to the large-sprue bar).

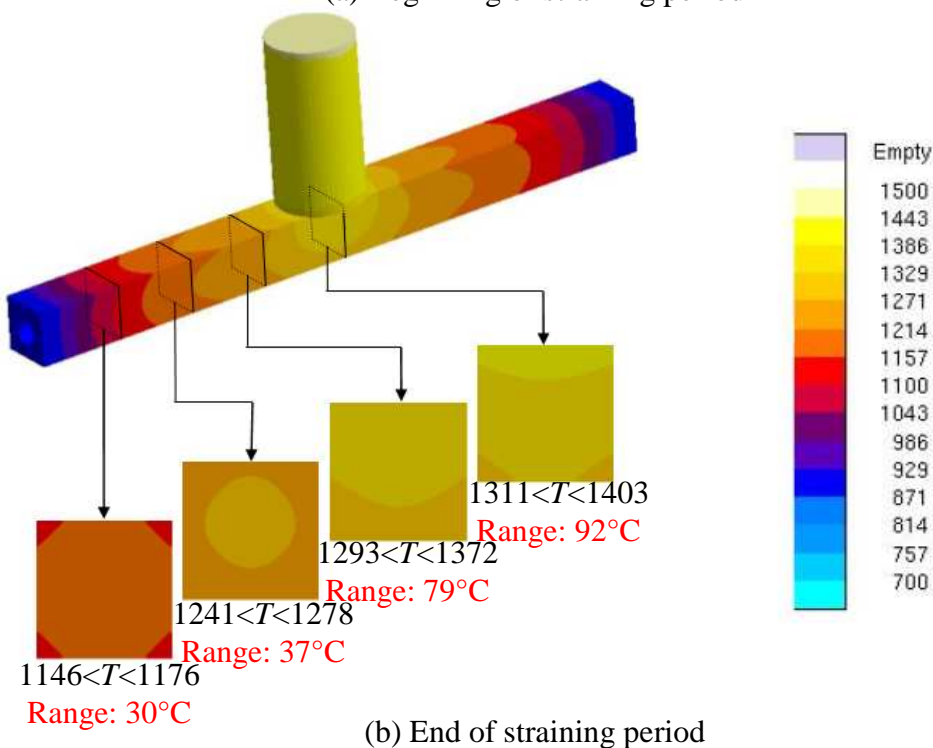
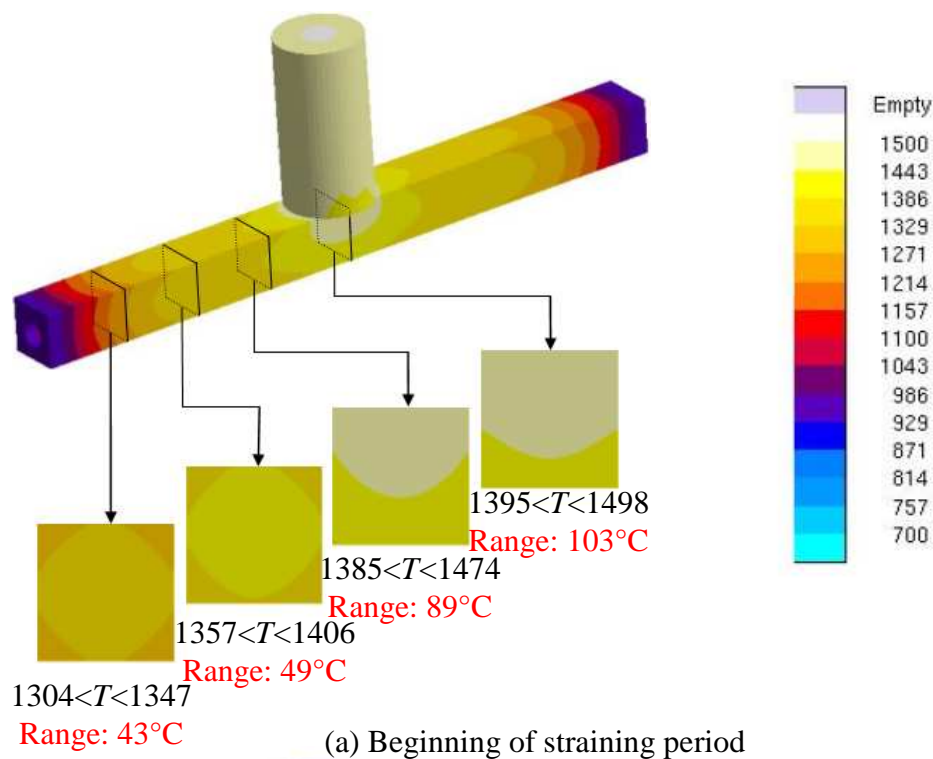


Figure 6.8. Simulated thermal fields of the large-sprue Strained bar at the beginning (a) and end (b) of the straining period. At the beginning of the straining period, the highest temperatures in the cross-section of the bar have a range of 151°C (1347 T 1498°C), resulting in relatively large temperature gradients (compared to the small-sprue bars).

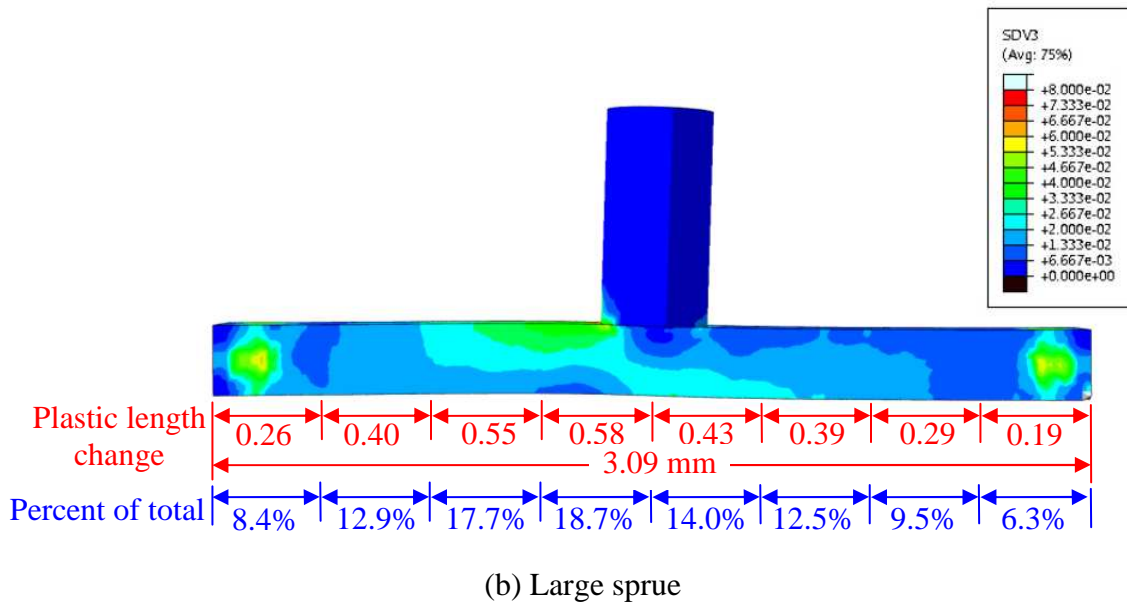
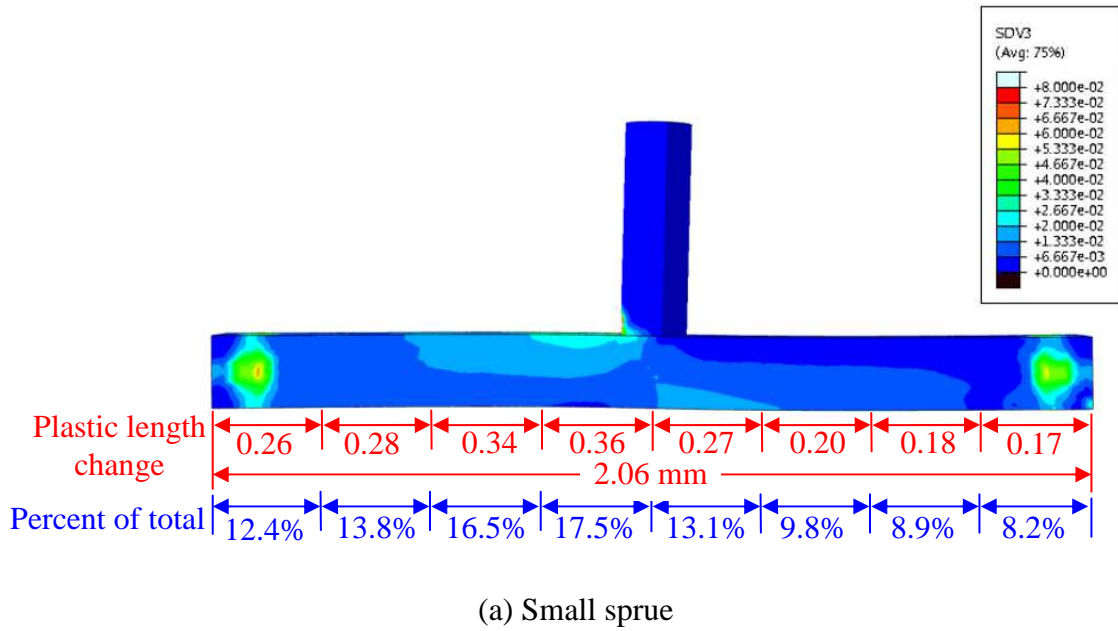


Figure 6.9. Predicted equivalent plastic strain of the small-sprue (a) and large-sprue (b) bars. Significant plastic strain is predicted along the length of both small-sprue and large-sprue bars. The force boundary condition at the sprue creates a higher percentage of predicted plastic strain on the left side of the bar.

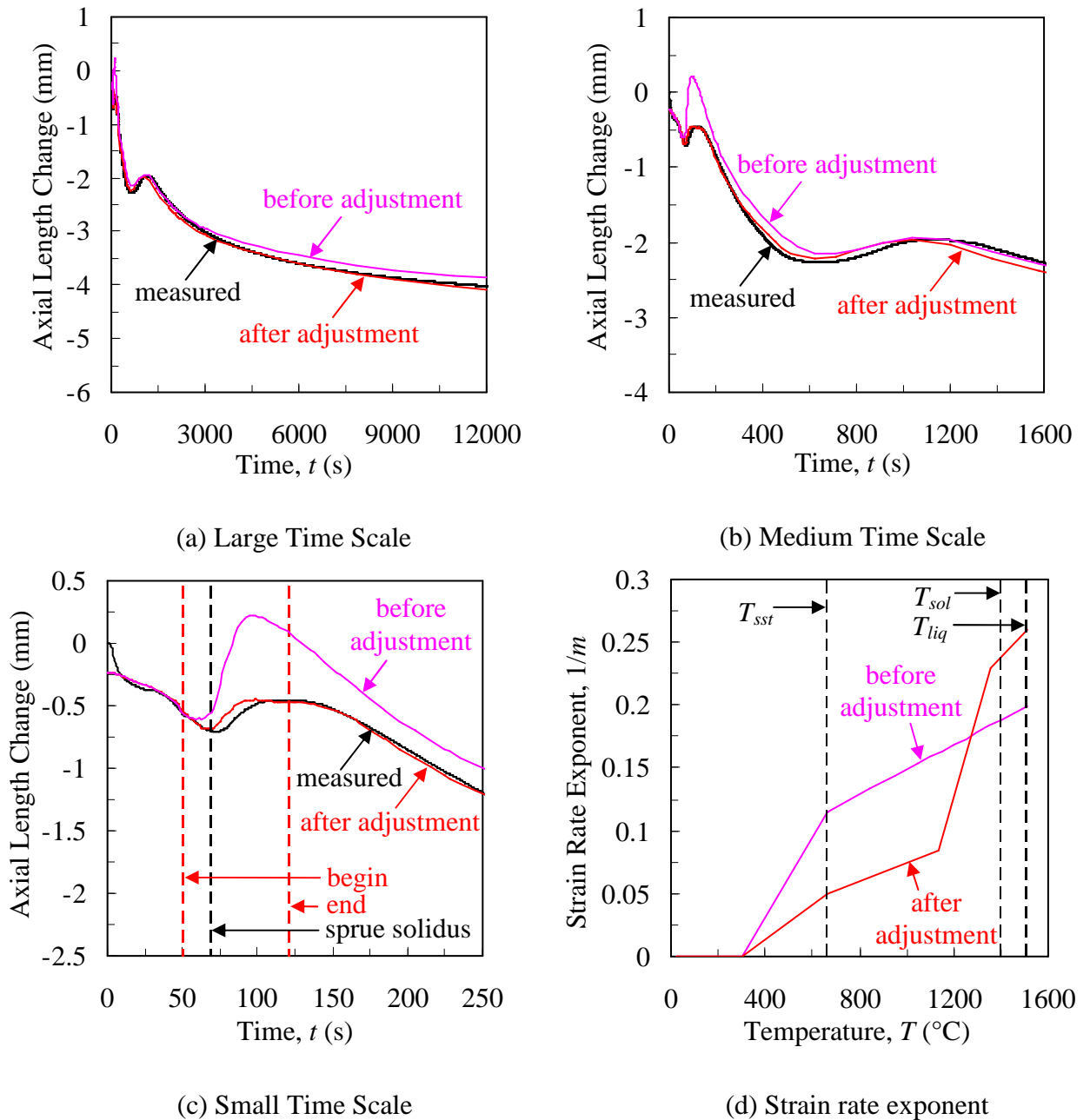


Figure 6.10. Comparison of the simulated and measured axial length changes of the Strained 1 experiment before and after adjustments to the strain rate exponent.

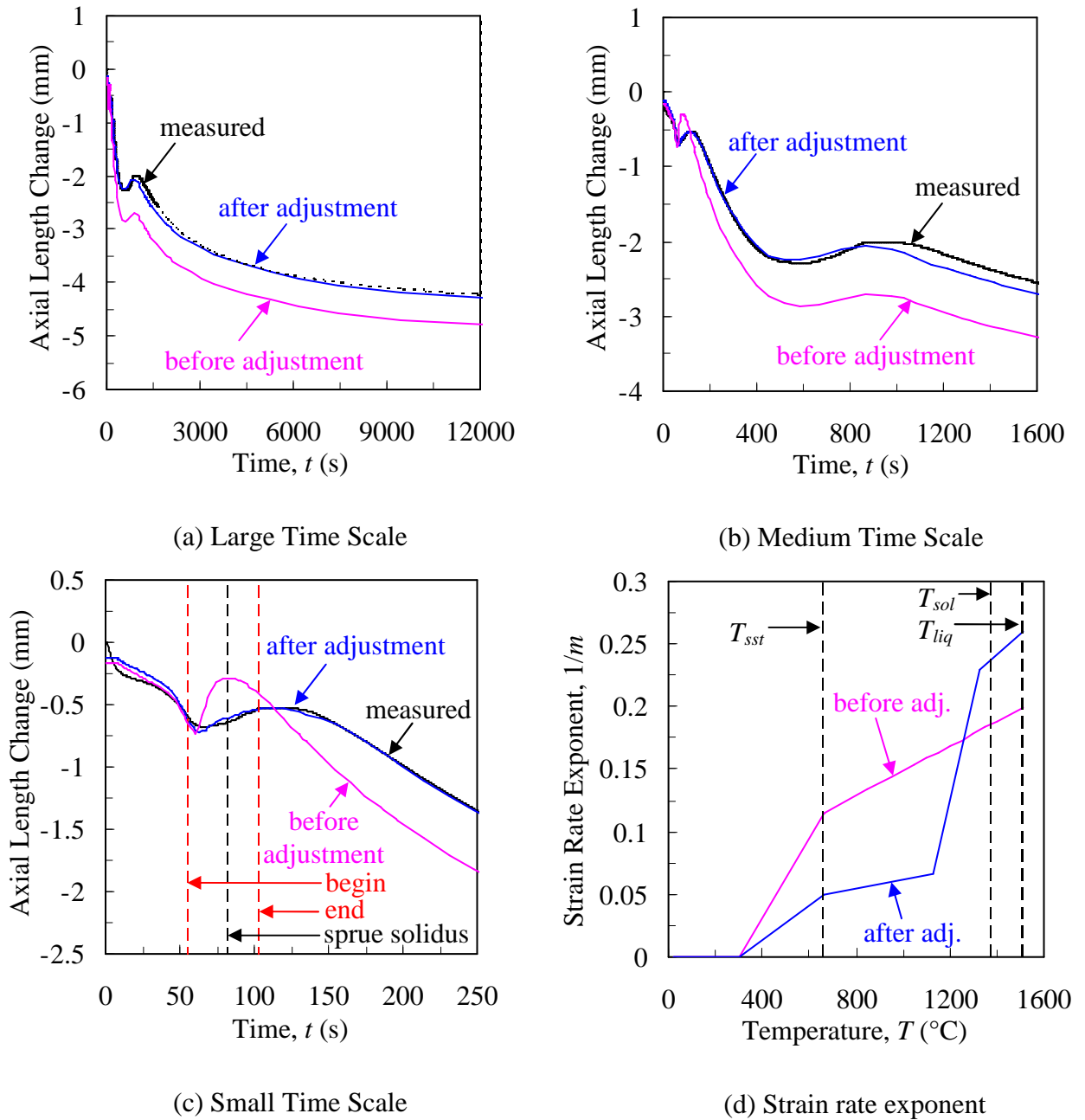


Figure 6.11. Comparison of the simulated and measured axial length changes of the Strained 2 experiment before and after adjustments to the strain rate exponent.

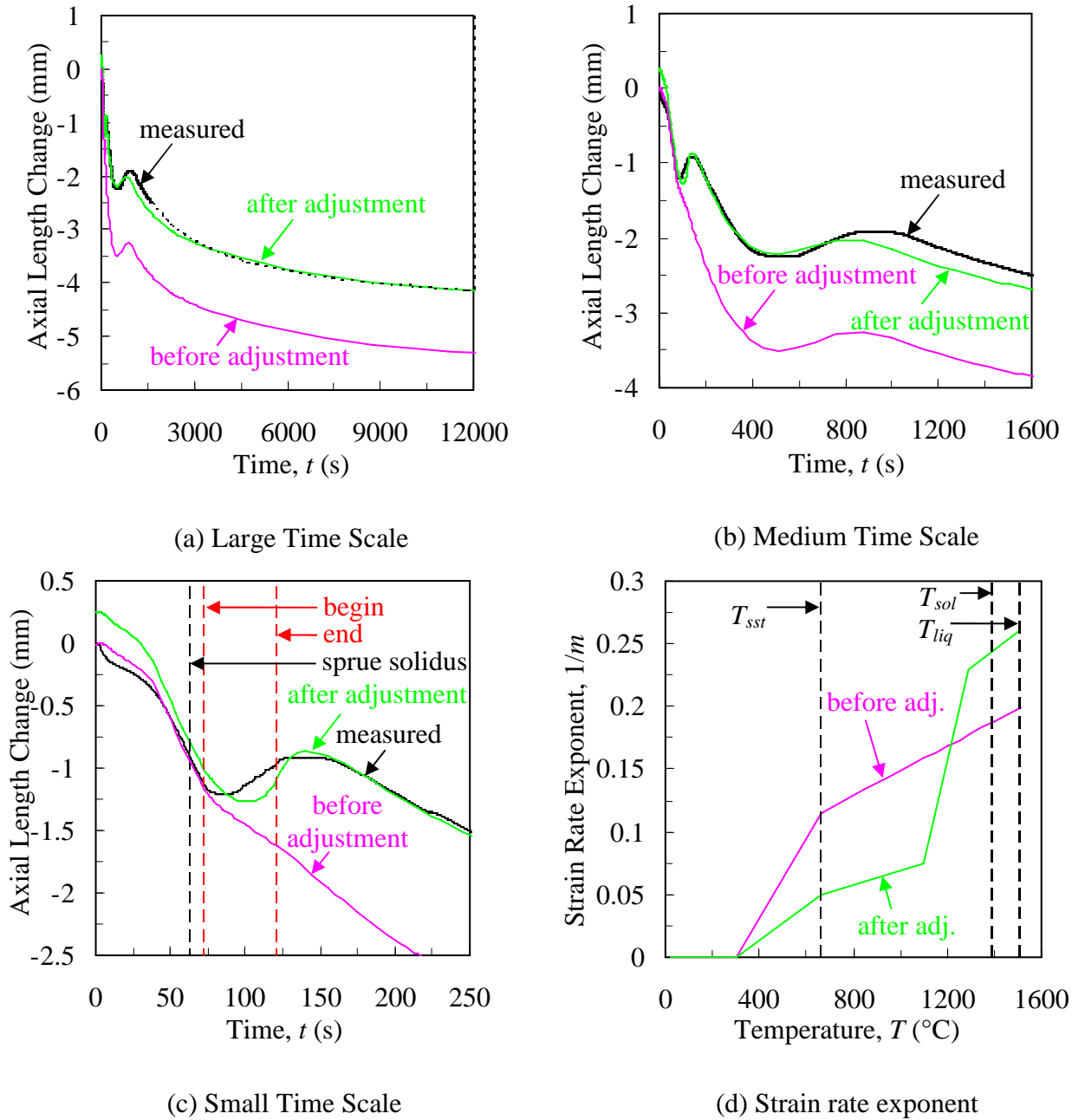
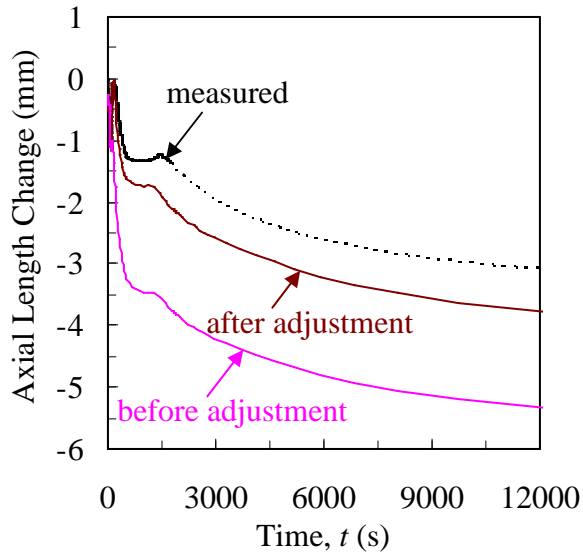
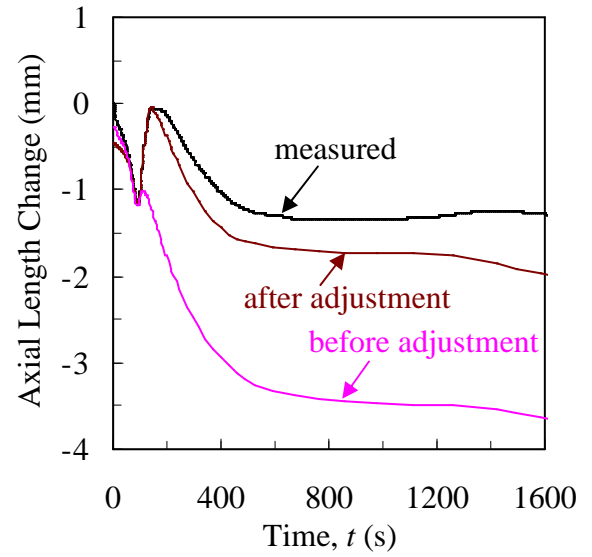


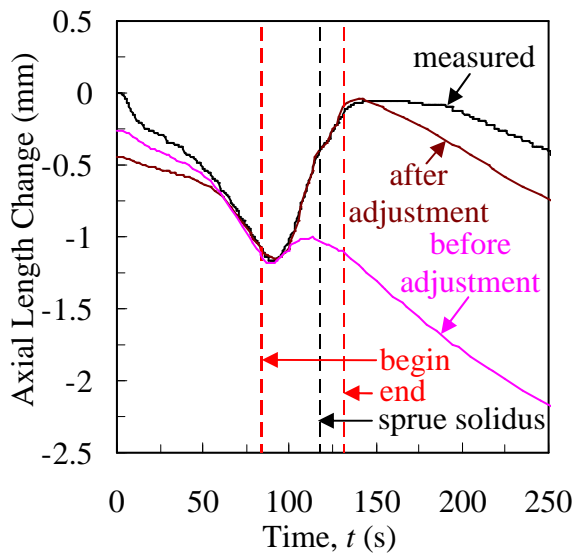
Figure 6.12. Comparison of the simulated and measured axial length changes of the Strained 3 experiment before and after adjustments to the strain rate exponent.



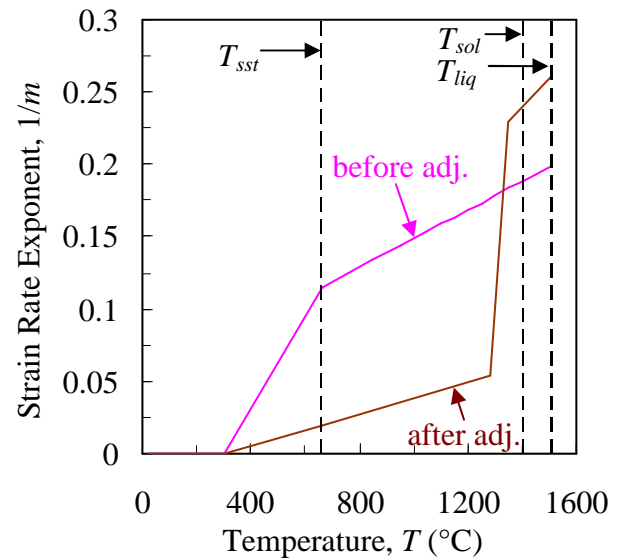
(a) Large Time Scale



(b) Medium Time Scale



(c) Small Time Scale



(d) Strain rate exponent

Figure 6.13. Comparison of the simulated and measured axial length changes of the Strained 4 experiment before and after adjustments to the strain rate exponent.

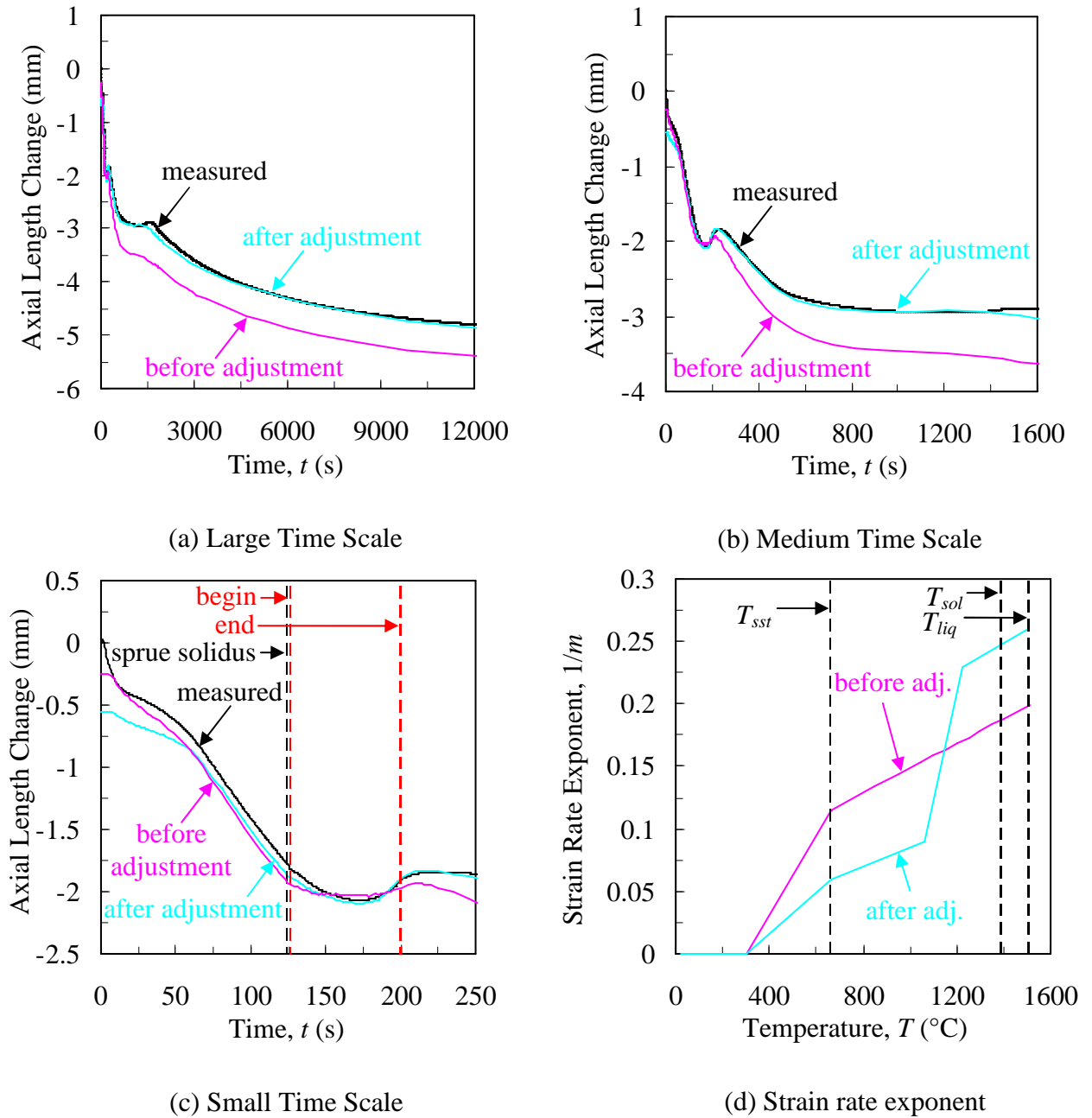


Figure 6.14. Comparison of the simulated and measured axial length changes of the Strained 5 experiment before and after adjustments to the strain rate exponent.

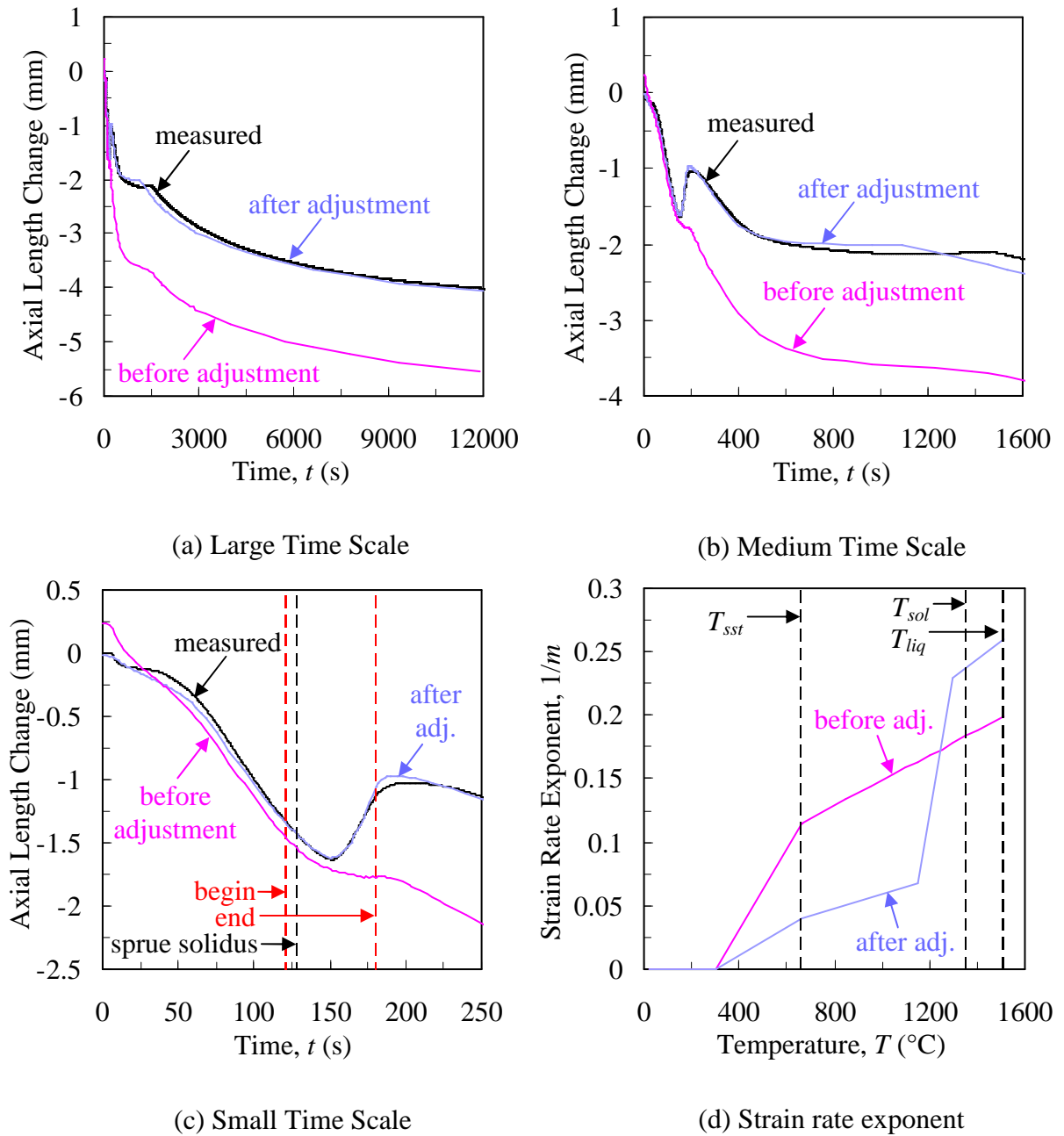


Figure 6.15. Comparison of the simulated and measured axial length changes of the Strained 6 experiment before and after adjustments to the strain rate exponent.

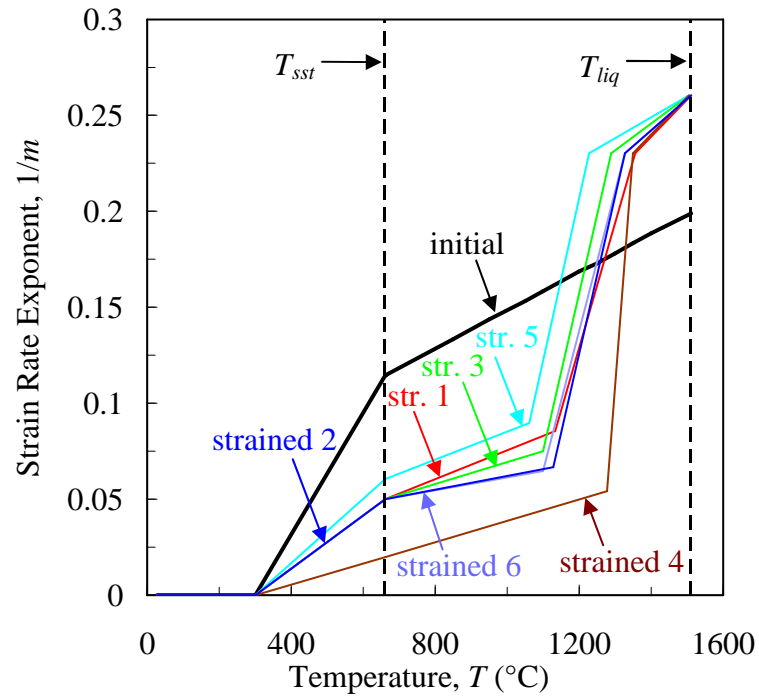


Figure 6.16. Adjusted strain rate exponents from all Strained stress simulations. The “initial” curve was estimated from the experimental data of Suzuki *et al.* [5], Wray [4], and Maciejewski *et al.* [56], shown in Figure 5.4.

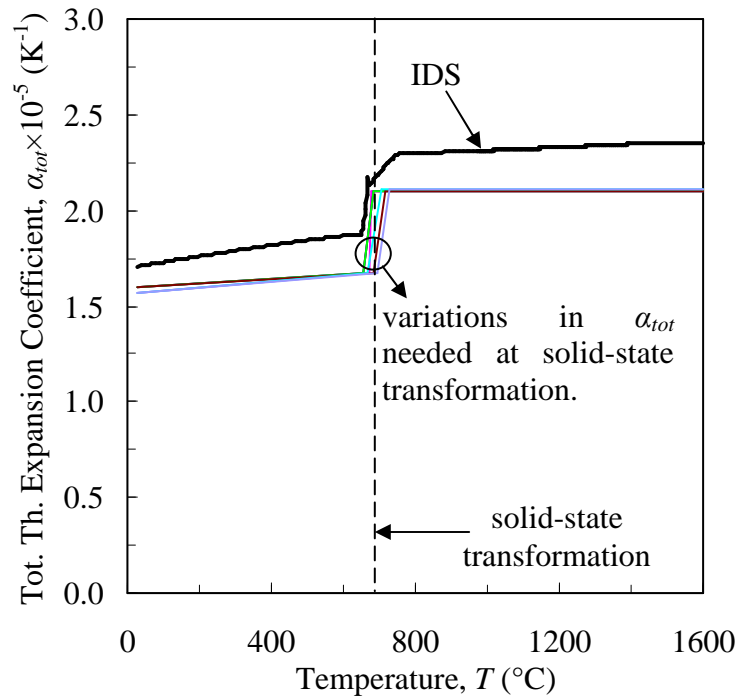


Figure 6.17. Total thermal expansion coefficient of the steel. Because of differences in casting chemistries, slight variations were needed at the solid-state transformation to achieve reasonable agreement between measured and simulated length changes.

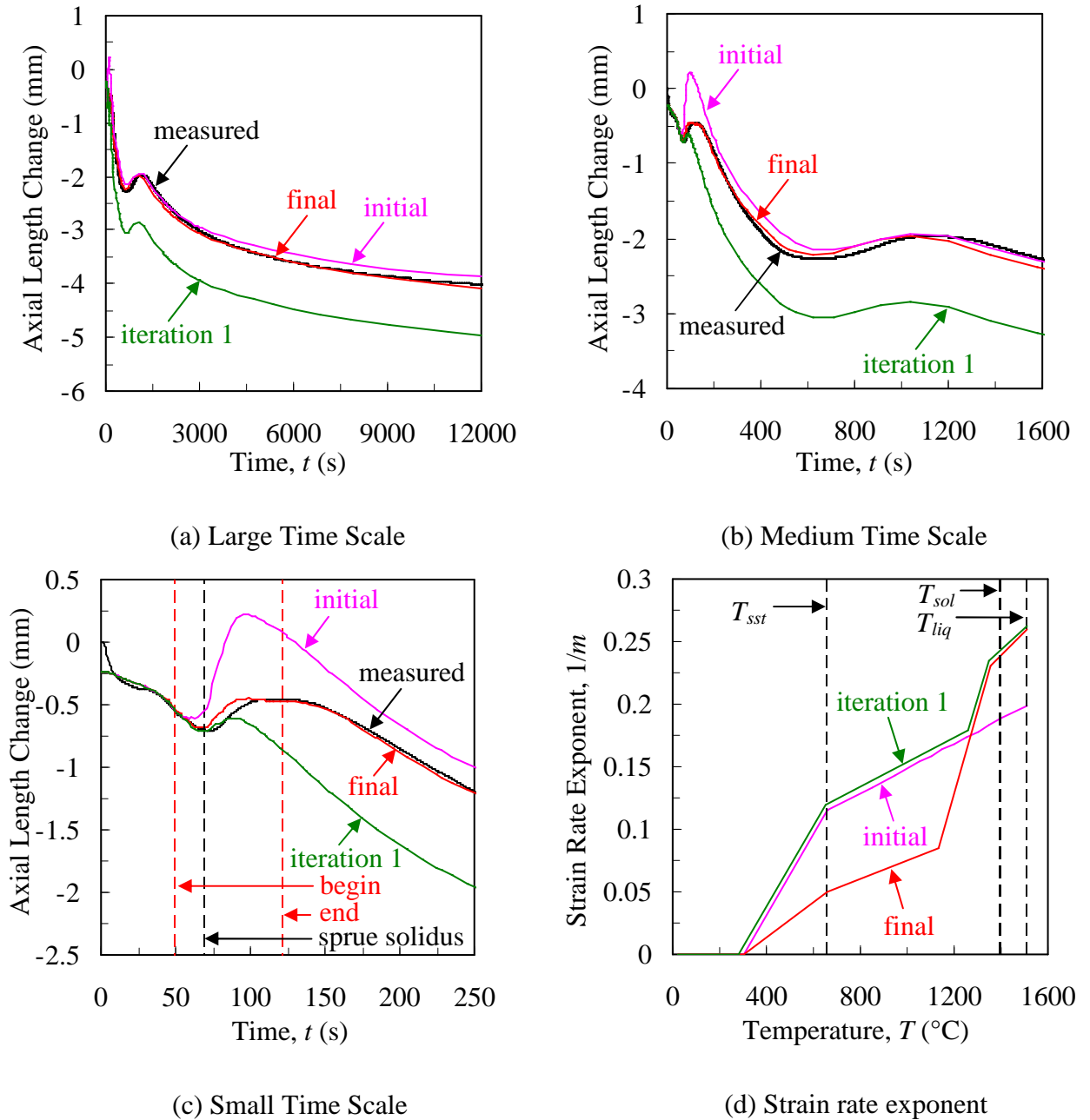


Figure 6.18. Parametric study of the strain rate exponent. To illustrate the necessity of the strain-rate exponent adjustments (shown in Figure 6.16), stress simulations were performed with iterations of the adjusted strain rate exponents. For this simulation, the “iteration 1” strain rate exponent curve matched the “final” curve at higher temperatures and “initial” curve at lower temperatures. As a result, the simulation predicts too little viscoplastic strain.

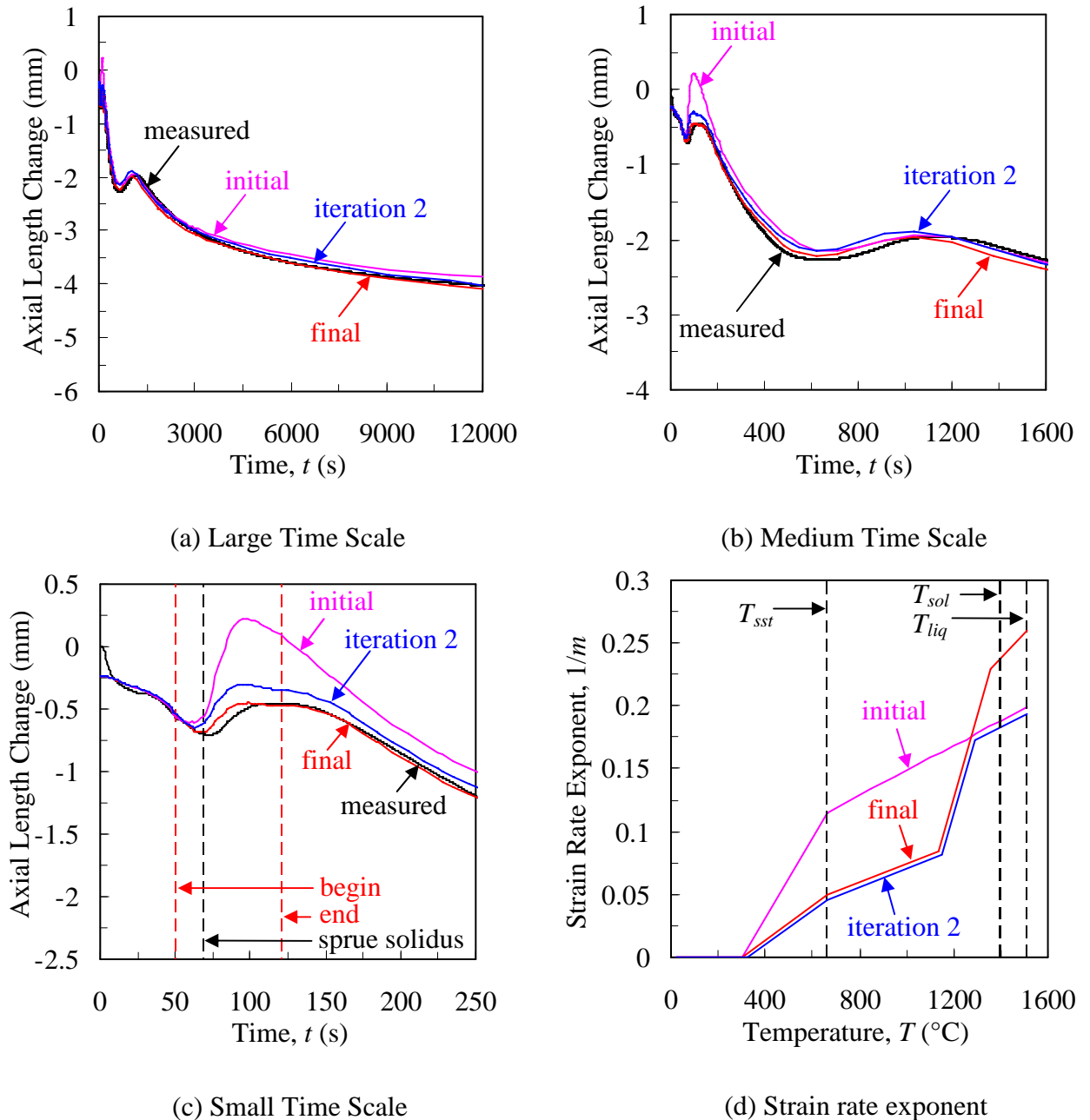


Figure 6.19. Parametric study of the strain rate exponent. To illustrate the necessity of the strain-rate exponent adjustments (shown in Figure 6.16), stress simulations were performed using iterations of the adjusted strain rate exponents. For this simulation, the “iteration 2” strain rate exponent curve matched the “final” curve at lower temperatures and “initial” curve at higher temperatures. As a result, the simulation predicts too much viscoplastic strain and occurring too early.

CHAPTER 7: CONCLUSIONS

An elasto-visco-plastic model was implemented with a user-defined UMAT subroutine in ABAQUS to predict stresses and deformations during solidification and cooling of a low-carbon steel casting. The simulations successfully predicted distortions in a casting environment, which is attributed to calibration of the computational model with dynamic force and displacement measurements from *in situ* casting experiments. For the preliminary stress simulations, the viscoplastic model parameters were estimated from the experimental data of Wray [4] and Suzuki *et al.* [5] (in which reheated steel specimens were subjected to uniaxial tests under isothermal conditions). However, the simulated distortions did not match the measurements, and a single material parameter (strain rate exponent) was adjusted accordingly to achieve agreement. This necessary adjustment (summarized as the Mastercurve in Figure 7.1) suggests the mechanical behavior of a steel casting during solidification and cooling cannot be characterized with stress-strain data from mechanical tests, as the harsh casting environment creates a segregated microstructure which, in turn, has a significant impact on the mechanical properties. Therefore, computational deformation models should be calibrated with stress-strain data obtained from testing conditions that reflect industrial casting processes. This will lead to the prediction of final casting dimensions with higher accuracy and, as a result, reduce wasteful post-casting rework.

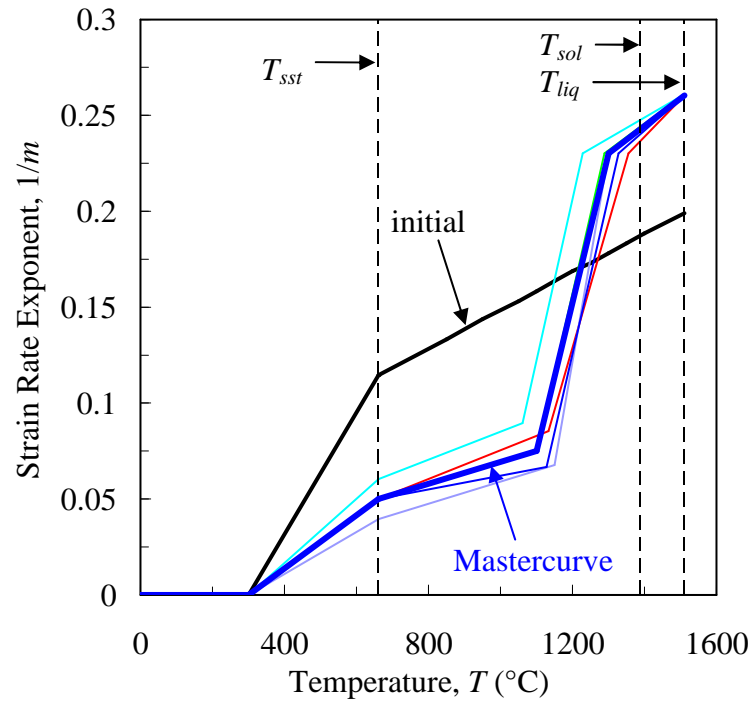


Figure 7.1. Strain rate exponent Mastercurve. The “initial” curve was estimated from the experimental data of Suzuki *et al.* [5], Wray [4], and Maciejewski *et al.* [56], shown in Figure 5.4.

REFERENCES

1. L. Bichler, A. Elsayed, K. Lee, and C. Ravindran, Influence of mold and pouring temperatures on hot tearing susceptibility of az91d magnesium alloy, *International Journal of Metalcasting*, vol. 2, no. 1, pp 45-56, 2008.
2. P. Feltham, The plastic flow of irons and plain steel above the a-3 point, *Physical Society – Proceedings*, vol. 66, no. 406B, pp 865-83, 1953.
3. P.J. Wray and M.F. Holmes, Plastic deformation of austenitic iron at intermediate strain rates, *Metallurgical Transactions A*, vol. 6A, no. 6, pp 1189-96, 1975.
4. P.J. Wray, Effect of carbon content on the plastic flow of plain carbon steels at elevated temperatures, *Metallurgical Transactions A*, vol. 13A, no. 1, pp 125-34, 1982.
5. T. Suzuki, K.H. Tacke, K. Wunnenberg, and K. Schwerdtfeger, Creep properties of steel at continuous casting temperatures, *Ironmaking and Steelmaking*, vol. 15, no. 2, pp 90-100, 1988.
6. C. Zhang, M. Bellet, M. Bobadilla, H. Shen, and B. Liu, Inverse finite element modelling and identification of constitutive parameters of uhs steel based on gleeble tensile tests at high temperature, *Inverse Problems in Science and Engineering*, vol. 19, no. 4, pp 485-508, 2011.
7. R.N. Parkins and A. Cowan, Effects of mould resistance on internal stresses in sand castings, *Proceedings of the Institute of British Foundation*, paper no. 1062, pp A101-9, 1953.
8. C.S.E. Mkumbo, B.B. Nyichomba, J. Campbell, and M. Tiryakioglu, Linear contraction of grey iron sand castings, *International Journal of Cast Metals Research*, vol. 14, no. 4, pp 225-34, 2002.
9. B.B. Nyichomba and J. Campbell, J., M., Linear contraction and residual stresses of aluminum alloy sand castings, *International Journal of Cast Metals Research*, vol. 11, pp 163-7, 1998.
10. B.B. Nyichomba, I.M. Cheya, and J. Campbell, Linear contraction of ductile iron castings, *International Journal of Cast Metals Research*, vol. 11, pp 179-86, 1998.
11. C. Monroe, and C. Beckermann, Deformation during casting of steel: mold and material properties, *Proceedings of the 61st SFSA Technical and Operating Conference*, paper no. 5.6, Steel Founders' Society of America, Chicago, IL, 2007.
12. P. Ackermann, J.D. Wagniere, and W. Kurz, In situ tensile testing of solidifying aluminum and al-mg shells, *Materials Science and Engineering*, vol. 75, pp 79-86, 1985.
13. H. Hiebler and C. Bernhard, Mechanical properties and crack susceptibility of steel during solidification, *Steel Research*, vol. 70, nos. 8 and 9, pp 349-55, 1999.

14. C. Bernhard, H. Moitzi, and M.M. Wolf, Influence of alloying elements and cooling conditions on hot tearing of steel, measured by the ssct-test, *Modeling of Casting, Welding, and Advanced Solidification Processes VIII*, B.G. Thomas and C. Beckermann, eds., pp 923-30, 1998.
15. Mi. Suzuki, Ma. Suzuki, C. Yu, and T. Emi, In-situ measurement of fracture strength of solidifying shells to predict upper limit of casting speed in continuous caster with oscillating mold, *ISIJ International*, vol. 37, no. 4, pp 375-82, 1997.
16. Y. Motoyama, H. Takahashi, Y. Inoue, K. Shinji, and M. Yoshida, Development of a device for dynamical measurement of the load on casting and the contraction of the casting in a sand mold during cooling, *Journal of Materials Processing Technology*, vol. 212, no. 6, pp 1399-1405, 2012.
17. Y. Motoyama, H. Takahashi, Y. Inoue, K. Shinji, and M. Yoshida, Dynamic measurements of the load on castings and the contraction of the castings during cooling in sand molds, *Journal of Materials Processing Technology*, vol. 213, no. 2, pp 238-44, 2013.
18. M. Bellet, F. Decultieux, M. Menai, F. Bay, C. Levaillant, J.L. Chenot, P. Schmidt, and I.L. Svensson, Thermomechanics of the cooling stage in casting processes: three-dimensional finite element analysis and experimental validation, *Metallurgical and Materials Transactions B*, vol. 27B, pp 81-99, 1996.
19. A. Stangeland, A. Mo, M. M'Hamdi, D. Viano, and C. Davidson, Thermal strain in the mushy zone related to hot tearing, *Metallurgical and Materials Transactions A*, vol. 37A, pp 705-14, 2006.
20. J.H. Weiner and B.A. Boley, Elasto-plastic thermal stresses in a solidifying body, *Journal of the Mechanics and Physics of Solids*, vol. 11, pp 145-54, 1963.
21. A. Grill, K. Sorimachi, and J.K. Brimacombe, Heat flow, gap formation, and break-outs in the continuous casting of steel slabs, *Ironmaking and Steelmaking*, vol. 3, pp 38-47, 1976.
22. J.O. Kristiansson, Thermomechanical behavior of the solidifying shell within continuous-casting billet molds – a numerical approach, *Journal of Thermal Stresses*, vol. 7, pp 209-26, 1984.
23. J.E. Kelly, K.P. Michalek, T.G. O'Connor, B.G. Thomas, and J.A. Dantzig, Initial development of thermal and stress fields in continuously cast steel billets, *Metallurgical Transactions A*, vol. 19A, pp 2589-602, 1988.
24. F.G. Rammerstorfer, C. Jaquemar, D.F. Fischer, and H. Wiesinger, Temperature fields, solidification progress and stress development in the strand during a continuous casting process of steel, *Numerical Methods in Thermal Problems*, Pineridge Press, Whiting, NJ, pp 712-22, 1979.
25. J.R. Boehmer, G. Funk, M. Jordan, and F.N. Fett, Strategies for coupled analysis of thermal strain history during continuous solidification processes, *Advances in Engineering Software*, vol. 29, nos. 7-9, pp 679-97, 1998.

26. A.E. Huespe, A. Cardona, and V. Fachinotti, Thermomechanical model of a continuous casting process, *Computer Methods in Applied Mechanics and Engineering*, vol. 182, pp 439-55, 2000.
27. A.E. Huespe, A. Cardona, N. Nigro, and V. Fachinotti, Visco-plastic models of steel at high temperature, *Journal of Materials Processing Technology*, vol. 102, pp 143-52, 2000.
28. J.M. Risso, A.E. Huespe, and A. Cardona, Thermal stress evaluation in the steel continuous casting process, *International Journal for Numerical Methods in Engineering*, vol. 65, pp 1355-77, 2006.
29. M. Bellet and V.D. Fachinotti, Ale method for solidification modeling, *Computer Methods in Applied Mechanics and Engineering*, vol. 193, pp 4355-81, 2004.
30. V.D. Fachinotti, S. Le Corre, N. Triolet, M. Bobadilla, and M. Bellet, Two-phase thermo-mechanical and macrosegregation modeling of binary alloys solidification with emphasis on the secondary cooling stage of steel slab continuous casting processes, *International Journal of Numerical Methods in Engineering*, vol. 67, pp 1341-84, 2006.
31. P.F. Kozlowski, B.G. Thomas, J.A. Azzi, and H. Wang, Simple constitutive equations for steel at high temperatures, *Metallurgical Transactions A*, vol. 23A, pp 903-18, 1992.
32. C. Li and B.G. Thomas, Thermomechanical finite-element model of shell behavior in continuous casting of steel, *Metallurgical and Materials Transactions B*, vol. 35B, pp 1151-72, 2004.
33. S. Koric and B.G. Thomas, Efficient thermo-mechanical model for solidification processes, *International Journal for Numerical Methods in Engineering*, vol. 66, pp 1955-89, 2006.
34. S. Koric, L.C. Hibbeler, and B.G. Thomas, Explicit coupled thermo-mechanical finite element model of steel solidification, *International Journal for Numerical Methods in Engineering*, vol. 78, pp 1-31, 2009.
35. M. Rowan, B.G. Thomas, R. Pierer, and C. Bernhard, Measuring mechanical behavior of steel during solidification: modeling the ssc test, *Metallurgical and Materials Transactions B*, vol. 42B, pp 837-51, 2011.
36. J.M. Drezet and M. Rappaz, Modelling of ingot distortions during direct chill casting of aluminum alloys, *Metallurgical and Materials Transactions A*, vol. 27A, pp 3214-25, 1996.
37. J.M. Drezet, M. Rappaz, G.U. Grun, and M. Gremaud, Determination of thermophysical properties and boundary conditions of direct chill-cast aluminum alloys using inverse methods, *Metallurgical and Materials Transactions A*, vol. 31A, pp 1627-34, 2000.
38. V. Mathier, J.M. Drezet, and M. Rappaz, Two-phase modeling of hot tearing in aluminum alloys using a semi-coupled approach, *Modelling and Simulation in Materials Science and Engineering*, vol. 15, pp 121-34, 2007.

39. M. M'Hamdi, A. Mo, and C.L. Martin, Two-phase modeling directed toward hot tearing formation in aluminum direct chill casting, *Metallurgical and Materials Transactions A*, vol. 33A, pp 2081-93, 2002.
40. A. Stangeland, A. Mo, O. Nielsen, D. Eskin, and M. M'Hamdi, Development of thermal strain in the coherent mushy zone during solidification of aluminum alloys, *Metallurgical and Materials Transactions A*, vol. 35A, pp 2903-15, 2004.
41. S. Gouttebroze, A. Mo, O. Grong, K.O. Pederson, and H.G. Fjaer, A new constitutive model for the finite element simulation of local hot forming of aluminum 6xxx alloys, *Metallurgical and Materials Transactions A*, vol. 39A, pp 522-34, 2008.
42. M. Pokorny, C. Monroe, and C. Beckermann, Prediction of hot tear formation in a Magnesium alloy permanent mold casting, *International Journal of Metalcasting*, vol. 2, no. 4, pp 41-53, 2008.
43. DASYLab v8.0, National Instruments, 11500 N. Mopac Expwy, Austin, TX 78759.
44. J. Ni and C. Beckermann, A volume-averaged two-phase model for solidification transport phenomena, *Metallurgical and Materials Transactions B*, vol. 22B, pp 349-61, 1991.
45. J. Miettinen, Calculation of solidification-related thermophysical properties for steels, *Metallurgical and Materials Transactions B*, vol. 28, no. 2, pp 281-97, 1997.
46. C. Monroe, Ph.D. thesis, University of Iowa, Iowa City, 2008.
47. I. Farup and A. Mo, Two-phase modeling of mushy-zone parameters associated with hot tearing, *Metallurgical and Materials Transactions A*, vol. 31A, pp 1461-72, 2000.
48. M. M'Hamdi, A. Mo, and H.G. Fjaer, Tearsim: a two-phase model addressing hot tearing formation during aluminum direct chill casting, *Metallurgical and Materials Transactions A*, vol. 37A, pp 3069-83, 2006.
49. J. Bluhm and R. DeBoer, The volume fraction concept in the porous media theory, *ZAMM – Journal of Applied Mathematics and Mechanics*, vol. 77, no. 8, pp 563-77, 1997.
50. J.C. Simo and T.J.R. Hughes, *Computational Inelasticity*, Springer-Verlag New York Inc., New York, NY, 1998.
51. C. Martin, M. Braccini, and M. Suery, Fracture behavior in tension of viscoplastic porous metallic materials saturated with liquid, *International Journal of Plasticity*, vol. 15, pp 981-1008, 2002.
52. A.C.F. Cocks, Inelastic deformation of porous materials, *Journal of the Mechanics and Physics of Solids*, vol. 37, no. 6, pp 693-715, 1989.
53. E.B. Marin and D.L. McDowell, A semi-implicit integration scheme for rate-dependent and rate-independent plasticity, *Computers and Structures*, vol. 63, no. 3, pp 579-600, 1997.
54. B.G. Thomas, Issues in thermal-mechanical modeling of casting processes, *ISIJ International*, vol. 35, no. 6, pp 737-743, 1995.

55. E.A. Brandes, *Smithell's Metals Reference Book*, 6th ed., Butterworth's, Boston, 1983.
56. K. Maciejewski, Y. Sun, O. Gregory, and H. Ghonem, Time-dependent deformation of low-carbon steel at elevated temperatures, *Materials Science and Engineering A*, vol. 534, pp 147-56, 2012.